BRNO UNIVERSITY OF TECHNOLOGY
VYSOKÉ UČENÍ TECHNICKÉ V BRNĚ

FACULTY OF MECHANICAL ENGINEERING
FAKULTA STROJNÍHO INŽENÝRSTVÍ

INSTITUTE OF PHYSICAL ENGINEERING
ÚSTAV FYZIKÁLNÍHO INŽENÝRSTVÍ

SPIN WAVE PROPAGATION IN STRUCTURES WITH LOCALLY MODIFIED MAGNETIC ANISOTROPY

ŠÍŘENÍ SPINOVÝCH VLN VE STRUKTURÁCH S LOKÁLNĚ MODIFIKOVANOU MAGNETICKOU ANIZOTROPIÍ

MASTER'S THESIS
DIPLOMOVÁ PRÁCE

AUTHOR — Bc. Václav Roučka
AUTOR PRÁCE

SUPERVISOR — Ing. Michal Urbánek, Ph.D.
VEDOUCÍ PRÁCE

BRNO 2021

BRNO UNIVERSITY OF TECHNOLOGY
FACULTY OF MECHANICAL ENGINEERING

Assignment Master's Thesis

Institut:	Institute of Physical Engineering
Student:	**Bc. Václav Roučka**
Degree programm:	Physical Engineering and Nanotechnology
Branch:	no specialisation
Supervisor:	**Ing. Michal Urbánek, Ph.D.**
Academic year:	2020/21

As provided for by the Act No. 111/98 Coll. on higher education institutions and the BUT Study and Examination Regulations, the director of the Institute hereby assigns the following topic of Master's Thesis:

Spin wave propagation in structures with locally modified magnetic anisotropy

Brief Description:

Spin–wave propagation is typically controlled by an external magnetic field, acting on the whole sample area. To be able to design and build spin–wave based devices, local control over spin–wave propagation (i.e. over the local effective field) is needed. There are two promising concepts for local magnetic anisotropy modification. The first method exploits focused ion beam control over the transformation of metastable iron thin films and the second concept is based on curvature induced anisotropy. The goal of the thesis is to exploit these concepts for steering of spin waves. Spin wave propagation in structures with locally–controlled anisotropy will be studied by means of micromagnetic simulations and by Brillouin light scattering experiments.

Master's Thesis goals:

Perform a literature search on the topic of steering of spin waves.
Design a spin–wave steering experiment and perform micromagnetic simulations.
Based on the results of micromagnetic simulations prepare suitable test samples.
Study spin–wave propagation in prepared samples by Brillouin light scattering microscopy.

Recommended bibliography:

URBÁNEK, Michal, Lukáš FLAJŠMAN, Viola KŘIŽÁKOVÁ, Jonáš GLOSS, Michal HORKÝ, Michael SCHMID a Peter VARGA. Research Update: Focused ion beam direct writing of magnetic patterns with controlled structural and magnetic properties [online]. B.m.: APL Materials. 2018. ISSN 2166-532X. Available from: doi:10.1063/1.5029367

TRETIAKOV, Oleg A., Massimiliano MORINI, Sergiy VASYLKEVYCH a Valeriy SLASTIKOV. Engineering Curvature-Induced Anisotropy in Thin Ferromagnetic Films [online]. B.m.: Physical Review Letters. 2017. ISSN 0031-9007. Available from: doi:10.1103/physrevlett.119.077203

Deadline for submission Master's Thesis is given by the Schedule of the Academic year 2020/21

In Brno,

L. S.

prof. RNDr. Tomáš Šikola, CSc.
Director of the Institute

doc. Ing. Jaroslav Katolický, Ph.D.
FME dean

ABSTRAKT

Zařízení založená na spinových vlnách mají potenciál být využita ve výpočetní technice s nízkou spotřebou energie. Pro úspěšné využití je samozřejmě potřeba spojit více takových zařízení na jednom čipu, součástí čehož musí být zatáčení spinových vln zahnutými vlnovody. Problém zatáčení spinových vln v dipolárně výměnném režimu zatím nebyl uspokojivě vyřešen, vyzkoušené přístupy vedly ke ztrátě intenzity a fázové koherence. V této diplomové práci jsme zkoumali dva systémy, které by mohly být využity k zatáčení spinových vln. Prvním z nich jsou tenké metastabilní vrstvy slitiny železa a niklu. Paramagnetická metastabilní fcc vrstva, která byla epitaxně narostena na substrátu z mědi, může být transformována do stabilní ferromagnetické bcc fáze pomocí fokusovaného iontového svazku. Tato technika nám dává prostorovou kontrolu nad transformačním procesem a strategie skenování svazkem nám dokonce umožňuje určit směr mangetické anisotropie. Magnetické vlastnosti struktur vytvořených touto metodou a lom spinových vln mezi doménami s odlišným směrem magnetické anisotropie byly změřeny pomocí mikroskopie Brillouinova rozptylu světla. Druhým zkoumaným systémem jsou zvlněné vlnovody, jejichž zvlnění indukuje magnetickou anisotropii. Zvlnění magnetické vrstvy je vytvořeno depozicí nemagnetických vlnek na substrátu indukovanou fokusovaným elektronovým svazkem a následnou depozicí magnetického materiálu. Byly vyrobeny různé návrhy zatočených zvlněných vlnovodů a změřili jsme šíření spinových vln jejich zatáčkami pomocí mikroskopie Brillouinova rozptylu světla. Využili jsme také mikromagnetické simulace pro získání hlubšího porozumění zkoumané problematiky a pro hledání vhodných návrhů experimentů.

Klíčová slova

Spinové vlny, magnetická anisotropie, Brillouinův rozptyl světla, lom vln

ABSTRACT

Devices based on spin waves have the potential to be used in low-power data processing. Naturally, a successful application would require many of those devices to be interconnected on a chip. Such a chip would have to include steering of spin waves through turned waveguides. The issue of steering dipole-exchange spin waves through waveguides has not been sufficiently solved so far, as the tested designs lead to a loss of intensity and phase coherence. In the presented thesis, we have studied two systems, which could be exploited for spin-wave steering. First, we dealt with metastable iron-nickel thin films. The paramagnetic metastable fcc layer epitaxially grown on a Cu substrate can be transformed into a stable ferromagnetic bcc phase by a focused ion beam. This technique gives us spatial control over the transformation process, and the scanning strategy even allows us to determine the direction of magnetic anisotropy. Magnetic properties of structures prepared by this technique, together with spin-wave refraction between domains with different anisotropy directions, were characterized by Brillouin light scattering microscopy. Moreover, we have studied spin-wave propagation in a system with corrugation-induced magnetic anisotropy. The corrugated magnetic film is created by focused electron beam-induced deposition of nonmagnetic ridges on a substrate and subsequent deposition of the magnetic material. Turned corrugated waveguides of different designs were prepared and we have measured spin-wave propagation through them by Brillouin light scattering microscopy. Micromagnetic simulations were also employed to provide further insight and to help us identify good experimental designs.

Key words

Spin waves, magnetic anisotropy, Brillouin light scattering, refraction

ROUČKA, Václav. *Spin wave propagation in structures with locally modified magnetic anisotropy*. Brno, 2021. Master's Thesis. Brno University of Technology, Faculty of Mechanical Engineering, Institute of Physical Engineering. Supervisor Michal Urbánek.

I hereby declare that I have written my master's thesis on the theme of *Spin wave propagation in structures with locally modified magnetic anisotropy* independently, under the guidance of the master's thesis supervisor, Ing. Michal Urbánek, Ph.D., and using the technical literature and other sources of information which are all properly quoted in the thesis and detailed in the list of literature at the end of the thesis.

Date

Bc. Václav Roučka

Acknowledgement

I am very grateful to my supervisor Michal Urbánek for his excellent guidance of this thesis. His extensive knowledge in the field of magnonics was profoundly helpful and his comments regarding this thesis resulted in higher quality of this text. I also need to express my gratitude towards Igor Turčan, who teached me several experimental techniques – focused electron beam induced deposition, electron beam lithography, deposition in evaporator, lift-off, and who measured some fabricated structures in the atomic force microscope for me. Furthermore, part of this thesis related to the wavy waveguides was possible only due to the prior research he has conducted on that system. He has also helped me with preparation of my last sample and proof-read my thesis. Further thanks are aimed at Ondřej Wojewoda, who teached me to use the Brillouin light scattering microscope. Moreover, I thank him for the insightful theoretical discussions we had. I would also like to thank Jakub Holobrádek, who introduced me to the metastable iron-nickel thin films and teached me how to transform them using the focused ion beam. Regarding the metastable films, I should also thank to all who participated in research of this system in the group under supervision of Michal Urbánek in the past, that is, to Lukáš Flajšman and Viola Křižáková. Lukáš Flajšman also deserves my gratitude for teaching me to perform micromagnetic simulations in MuMax. Finally, I am thankful to my parents for their support, which allowed me to fully focus on my studies and to work on this thesis.

Václav Roučka

Financial support from the Thermo Fisher Scientific is gratefully acknowledged.

CzechNanoLab project LM2018110 funded by MEYS CR is gratefully acknowledged for the financial support of the measurements/sample fabrication at CEITEC Nano Research Infrastructure.

Contents

Introduction 1

1 Micromagnetic theory and spin waves 2

1.1 Micromagnetic energies 2

1.1.1 Zeeman energy 2

1.1.2 Demagnetization energy 2

1.1.3 Exchange energy 4

1.1.4 Crystalline anisotropy energy 4

1.1.5 Magnetoelastic anisotropy energy 5

1.2 Magnetic order and dynamics 6

1.2.1 Static micromagnetism and effective field 6

1.2.2 Magnetization dynamics 8

1.3 Spin waves 10

1.3.1 Dispersion relation 10

1.3.2 Group velocity and propagation length 16

1.3.3 Refraction and steering of spin waves 17

2 Techniques 23

2.1 Electron beam lithography 23

2.2 Brillouin light scattering microscopy 24

2.3 Kerr microscopy 27

2.4 Micromagnetic simulations 28

3 Metastable iron-nickel system 31

3.1 Magnetic structures in metastable films 31

3.2 Prepared magnetic structures 36

3.2.1 Magneto-optical measurements of anisotropy 36

3.2.2 Brillouin light scattering – thermal spectra 39

3.2.3 Brillouin light scattering – decay length 42

4 Wavy waveguides system 44

4.1 Fabrication of wavy samples 44

4.2 Geometrically induced anisotropy 46

4.2.1 Theoretical mechanism 47

4.2.2 Experimental investigation of anisotropy 54

5 Refraction of spin waves 57

5.1 Refraction from domain (6) to domain (5) 58

5.2 Refraction from domain (5) to domain (6) 60

5.3 Refraction from domain (6) to domain (alp) 62
6 Turning of spin waves 64
6.1 Simulations of alternative turn designs 64
6.2 Wavy waveguide turns of transversal design 68
6.3 Wavy waveguide turns of tilted design 73
Conclusion 77
References 79
List of used abbreviations 84

Introduction

Further development of computing electronics based on the CMOS technology (Complementary Metal-Oxide-Semiconductor) is starting to approach its economic and physical limits [1]. For this reason, new technologies with prospects of usage in information processing and related areas are being explored. One of them are devices based on spin waves. Spin waves are small collective excitations of magnetic order, and their quasiparticles are called magnons. They offer a wide range advantages – their wave nature adds another degree of freedom, the phase; there is no Joule heating because no moving charges are involved, this also allows utilization of insulating materials; their frequencies (which limit the device's operating speed) range from GHz to THz; their wavelengths (which limit the device's size) can be downscaled down to a few nanometers; and their nonlinear phenomena allow for manipulation of one signal by another [2]. Many simple spin wave-based devices, such as a majority gate [3] or an all-magnon transistor [4], have already been experimentally demonstrated.

A successful spin wave-based application would require many of such devices to be interconnected on a chip. Unfortunately, the issue of steering dipolar and dipole-exchange spin waves through turned waveguides has not been sufficiently solved so far. The tested designs with their shortcomings are reviewed at the end of the first chapter. In the presented thesis, we study two systems, which could be exploited for spin-wave steering.

In the first chapter we outline the basics of micromagnetic theory starting from the different magnetic energies, which govern the behavior of magnetic system, and leading up to the spin waves with their highly anisotropic dispersion relation. At the end of that chapter, we shortly review the research of refraction and turning of spin waves. The second chapter covers the techniques used to reach the goals of this thesis, which includes the electron beam lithography, Brillouin light scattering microscopy, magneto-optical Kerr microscopy and micromagnetic simulations.

The third chapter deals with the metastable iron-nickel thin films, which are epitaxially grown on fcc copper substrates in their paramagnetic fcc phase. We then describe the process of transforming these films into stable ferromagnetic bcc phase using the focused ion beam and how we can create domains with different anisotropy directions. Magnetic properties of the transformed domains are measured.

In the fourth chapter we first introduce the process of fabricating wavy waveguides, which is based on creating a corrugation on a substrate by focused electron beam induced deposition and subsequent deposition of a magnetic film on top of it. Then we discuss the origin of the geometrically induced anisotropy in these structures and its experimental demonstrations.

The fifth chapter contains our Brillouin light scattering measurements of spin waves refracting between transformed iron-nickel domains with different anisotropy directions.

In the sixth and final chapter we present our investigation of spin wave steering in turned waveguides with locally varying anisotropy direction. Two different turned waveguide designs are compared in micromagnetic simulations. Then we show experimental realizations of these designs in the wavy waveguide system. Brillouin light scattering microscopy measurements reveal that one of the designs fails, but in the other we observe a successful propagation of the spin wave through the turn.

1 Micromagnetic theory and spin waves

In this chapter, we briefly outline a theoretical description of magnetic phenomena relevant for the goals of this thesis. First, the micromagnetic theory is introduced, and the most important energies governing the behavior of magnetic systems are described. Then, in section 1.2, we present the equations, which guide the statics and dynamics of magnetic systems. And lastly, in section 1.3, we characterize spin waves and their properties such as dispersion relation and group velocity, and we also review studies on refraction and steering of these waves.

Micromagnetic theory utilizes findings of quantum-mechanical theory of magnetism, which includes effects essential for a successful description of magnetism but deals with discrete spins, and incorporates them into description using continuous quantities from the Maxwell equations [5], [6]. This theory is valid if spins neighboring over several lattice constants, that is, on the so-called mesoscopic scale, are almost parallel [5]. The distribution of discrete magnetic moments $\vec{\mu}_i$ connected to individual spins $\vec{S}_i$ is in this theory represented by a continuous quantity – magnetization $\vec{M}(\vec{r})$, which is defined as spatial average of magnetic moments over this small volume. In any given material the norm (size) of this vector field is constant and is called the saturation magnetization M_S.

1.1 Micromagnetic energies

Micromagnetism generally deals with the problem of solving the spatial and possibly also temporal distribution and direction of magnetization $\vec{M}(\vec{r},t)$. In a nutshell, determination of these functions relies on finding the (Gibbs free) energy density and consecutively minimizing the total (integrated over volume of a magnet) energy or solving the equation of motion for magnetization [6] as will be discussed in the next section. Solution of these problems relies on the concept of effective magnetic field, which is derived from the total energy density. Therefore, in the following subsections, we will present the different contributions to this energy density.

1.1.1 Zeeman energy

Zeeman energy is the energy of a magnetic moment in an external magnetic field $\vec{H}_{\mathrm{ext}}$. The corresponding energy density in micromagnetism is

$$E_{\mathrm{Z}} = -\mu_0 \vec{M} \cdot \vec{H}_{\mathrm{ext}}. \tag{1.1}$$

The energy is minimal when the magnetization is parallel to the external field.

1.1.2 Demagnetization energy

Demagnetization energy, sometimes called dipolar energy, is in principle the same as Zeeman energy, but the associated magnetic field is created by the magnetization of the studied system instead of some external source or electrical current. The field is called the demagnetization or dipolar field $\vec{H}_{\mathrm{d}}$ and the energy density is

$$E_{\mathrm{d}} = -\frac{1}{2}\mu_0 \vec{M} \cdot \vec{H}_{\mathrm{d}}. \tag{1.2}$$

The prefactor ½ ensures, that when we integrate over the volume of the magnet to obtain the total energy, we count energy associated with magnetization in position A creating field that acts on magnetization in position B and B acting on A only once, as one energy.

Magnetic flux density is $\vec{B} = \mu_0(\vec{H} + \vec{M})$ [7, p. 35]. Origin of the demagnetization field can be quickly derived from the Maxwell equations, if we assume the external field and any current density to be zero

$$\vec{\nabla} \cdot \vec{B} = \mu_0 \vec{\nabla} \cdot (\vec{H}_\mathrm{d} + \vec{M}) = 0, \tag{1.3}$$

$$\vec{\nabla} \cdot \vec{H}_\mathrm{d} = -\vec{\nabla} \cdot \vec{M}. \tag{1.4}$$

The problems of micromagnetism involve magnetic fields changing in time, but generally working in the magnetostatic approximation produces accurate models. Then the Ampere's law with zero current density reads $\vec{\nabla} \times \vec{H} = \vec{0}$, which allows us to describe the demagnetization field by a gradient of a scalar potential φ_d as

$$\vec{H}_\mathrm{d} = -\vec{\nabla}\varphi_\mathrm{d}. \tag{1.5}$$

Expression on the right side of (1.4) can be named the magnetic charge density $\rho_M = -\vec{\nabla} \cdot \vec{M}$. Inserting all of this into equation (1.4) gives us the Poisson's equation

$$\vec{\nabla}^2 \varphi_\mathrm{d} = -\rho_M. \tag{1.6}$$

This is an analogy to the electrostatic problem of finding the electric potential for a given charge distribution. But here the charges are present due to inhomogeneities in orientation of magnetization (or more rarely due to inhomogeneities in the size of saturation magnetization) and due to the magnetization pointing out of the sample on the material border (important surface charges $\sigma_M = \vec{\mathrm{n}} \cdot \vec{M}$, $\vec{\mathrm{n}}$ is normal to the surface). This classical problem can be solved by the means of Green's function $G(\vec{r})$ [5]

$$G(\vec{r}) = \frac{1}{4\pi|\vec{r}|}, \tag{1.7}$$

$$\varphi_\mathrm{d}(\vec{r}) = \int G(\vec{r} - \vec{r}')\rho_M(\vec{r}')\mathrm{d}^3\vec{r}' = \int \frac{-\vec{\nabla}' \cdot \vec{M}(\vec{r}')}{4\pi|\vec{r} - \vec{r}'|}\mathrm{d}^3\vec{r}'. \tag{1.8}$$

Sometimes it is advantageous to work directly with magnetization rather than with its divergence. This can be achieved by integrating (1.8) by parts and by considering the integration volume to encompass all magnetic material and to end in void. This results in the first term to be zero, and we can compute the magnetostatic potential as

$$\varphi_\mathrm{d}(\vec{r}) = \int \vec{\nabla}' \left(\frac{1}{4\pi|\vec{r} - \vec{r}'|}\right) \vec{M}(\vec{r}')\mathrm{d}^3\vec{r}'. \tag{1.9}$$

Returning to the demagnetizing field

$$\vec{H}_\mathrm{d}(\vec{r}) = -\vec{\nabla} \int \vec{\nabla}' \left(\frac{1}{4\pi|\vec{r} - \vec{r}'|}\right) \vec{M}(\vec{r}')\mathrm{d}^3\vec{r}'. \tag{1.10}$$

For certain problems involving spin waves [8], [9] it is convenient to work with the so-called magnetostatic tensorial Green's function $\hat{\Gamma}(\vec{r} - \vec{r}')$. Using its formalism, the demagnetizing field can be calculated from any given magnetization configuration as

$$\vec{H}_\mathrm{d}(\vec{r}) = \int \hat{\Gamma}(\vec{r} - \vec{r}')\vec{M}(\vec{r}')\mathrm{d}^3\vec{r}'. \tag{1.11}$$

And the various components of this tensor are defined as

$$\Gamma_{\alpha\beta}(\vec{r} - \vec{r}') = -\frac{\partial}{\partial\alpha\partial\beta'}\left(\frac{1}{4\pi|\vec{r} - \vec{r}'|}\right), \tag{1.12}$$

where $\alpha, \beta = x, y, z$.

Effects of the dipolar interaction are demonstrated in Fig. 1.1 and can be formulated as the charge avoidance principle – magnetization tends to configure in a way to minimize creation of the magnetic charges. Especially large (surface) charges can be created on the material borders, so the magnetization favors aligning parallelly to the surfaces. In the bulk the magnetization tends to have small divergence and charges of the same sign prefer not to be close to each other [7, p. 238].

1.1.3 Exchange energy

Classical electrodynamics could not explain the characteristic trait of ferromagnetic materials – their nonzero macroscopic magnetization even without the presence of an external magnetic field. This disagreement of theory and empirical observations was resolved with the development of quantum mechanics and introduction of the exchange interaction by Heisenberg in 1928 [10].

Existence of the exchange interaction relies on the Pauli's exclusion principle and the Coulomb interaction. Pauli's principle states, that the total wave function of a system of identical fermions (two electrons in different atoms in our case) must be antisymmetric with regards to exchange of any two particles. This can be achieved by antisymmetry in the space functions or in the spin functions (but not both together, which would result in symmetry of the total function). In other words, the total antisymmetric wave function consists either of a symmetric space function and an antisymmetric spin function or of an antisymmetric space function and a symmetric spin function. Energies of these two different states are generally not the same and can be evaluated by using the Hamiltonian, which contains the Coulomb interaction. Because of the clear connections between the space and spin functions the energy difference can be rewritten in terms of spins. The Heisenberg's exchange Hamiltonian for a system of (dimensionless) spins $\vec{S}_i$ localized at sites indexed by *i* and *j* is [7, p. 137]

$$\mathcal{H}_{\mathrm{ex}} = -2 \sum_{i>j} J_{ij}\, \vec{S}_i \cdot \vec{S}_j, \tag{1.13}$$

where J_{ij} is the exchange integral computed using the space function-related Hamiltonian containing the Coulomb interaction and the space wave functions of electrons on the sites *i* and *j*. Since the wave functions of electrons in non-neighboring atoms practically do not overlap, the exchange integral is significant only for the nearest neighbors and consequently the exchange interaction is an extremely close-range phenomenon, nevertheless a strong one. Positive values of J_{ij} lead to a preference of parallel alignment of spins, that is, ferromagnetism while negative values lead to antiparallel alignment and antiferromagnetism.

In the continuous micromagnetic framework, the Heisenberg exchange energy density can be described using the exchange constant A_{ex}, positive for ferromagnets, and the normalized magnetization $\vec{m} = \vec{M}/M_S$ as [5]

$$E_{\mathrm{ex}} = A_{\mathrm{ex}} \left(\vec{\nabla} \cdot \frac{\vec{M}}{M_S} \right)^2 = A_{\mathrm{ex}} \left(\vec{\nabla} \cdot \vec{m} \right)^2. \tag{1.14}$$

1.1.4 Crystalline anisotropy energy

The next contribution to the Gibbs free energy, which will be mentioned, stems from symmetries of the crystal lattice and is called the crystalline or magnetocrystalline anisotropy energy E_{anis}. Its origin lies in the spin-orbit coupling and in the case of some non-cubic lattices also in the dipolar interaction [7, p. 172].

In magnetic crystals with this property, it is energetically favorable for the magnetization to align in certain directions defined by the crystallographic axes. The simplest case is the uniaxial anisotropy, which is naturally present in the hexagonal lattices, and its energy density can be written as [7, p. 170]

$$E_{\mathrm{uni}} = K_{\mathrm{u}} \sin^2\theta + K_{\mathrm{u2}} \sin^4\theta, \tag{1.15}$$

where θ is the angle between magnetization and the uniaxial anisotropy axis. In this notation magnetization will prefer aligning along this axis if the constants K_{u} and K_{u2} are positive. Such axis is then called easy axis (and the plane perpendicular to this axis can be called hard plane). In the opposite case of negative anisotropy constants, the magnetization favors aligning perpendicular to this axis and we speak of hard axis and easy plane. Usually only the first (K_{u}) term is significant.

In crystals with cubic symmetry the magnetocrystalline anisotropy energy density can be described using cosines α_i of the magnetizations angle to the crystal axes

$$E_{\mathrm{cub}} = K_{\mathrm{c1}}(\alpha_1^2\alpha_2^2 + \alpha_2^2\alpha_3^2 + \alpha_3^2\alpha_1^2) + K_{\mathrm{c2}}(\alpha_1^2\alpha_2^2\alpha_3^2). \tag{1.16}$$

If we consider only the first term, then there are four easy axes $\langle 111 \rangle$ for negative K_{c1} and three easy axes $\langle 100 \rangle$ for positive values of this material constant [11, p. 202]. The latter situation corresponds to iron with $K_{\mathrm{c1}} = 48\ \mathrm{kJ/m^3}$ and $K_{\mathrm{c2}} = \pm 5\ \mathrm{kJ/m^3}$ [11, p. 227]. Again, in many applications it is sufficient to consider only the first term.

The magnetocrystalline anisotropy should not be confused with the so-called shape anisotropy, which has its origin in the demagnetizing field and depends on the samples shape instead of some intrinsic material characteristic.

1.1.5 Magnetoelastic anisotropy energy

Magnetoelastic anisotropy energy is similar to the crystalline anisotropy energy in being a function of only the local stress/crystal and magnetization direction. Magnetoelastic anisotropy energy comes from the inverse magnetostrictive effect, according to which mechanical stress creates new sources of energy depending on the directions (and magnitude) of magnetization and stress. Origin of this effect is again the spin-orbit interaction [11, p. 258].

The magnetoelastic anisotropy energy density in cubic crystals can be written as [11, p. 261]

$$\begin{aligned} E_{\mathrm{me}} = -\frac{3}{2}\lambda_{100}\sigma(\alpha_1^2\gamma_1^2 + \alpha_2^2\gamma_2^2 + \alpha_3^2\gamma_3^2) \\ - 3\lambda_{111}\sigma(\alpha_1\alpha_2\gamma_1\gamma_2 + \alpha_2\alpha_3\gamma_2\gamma_3 + \alpha_3\alpha_1\gamma_3\gamma_1), \end{aligned} \tag{1.17}$$

where σ is the magnitude of stress (N/m^2), γ_i are the direction cosines of the stress and λ_{100}, λ_{111} are the magnetostrictive coefficients in directions $\langle 100 \rangle, \langle 111 \rangle$. If the stress is applied along the $[100]$ direction, the energy density is simplified to

$$E_{\mathrm{me}} = -\frac{3}{2}\lambda_{100}\,\sigma \cos^2(\theta), \tag{1.18}$$

where θ is the angle between magnetization and $[100]$. Using $\cos^2(\theta) = 1 - \sin^2(\theta)$ and subtracting the constant term, we get

$$E_{\mathrm{me}} = \frac{3}{2}\lambda_{100}\,\sigma \sin^2(\theta). \tag{1.19}$$

In materials with positive magnetostrictive coefficient λ_{100}, such as iron [11, p. 249], and with positive (tensile) stress σ this case presents an uniaxial easy-axis anisotropy along $[100]$.

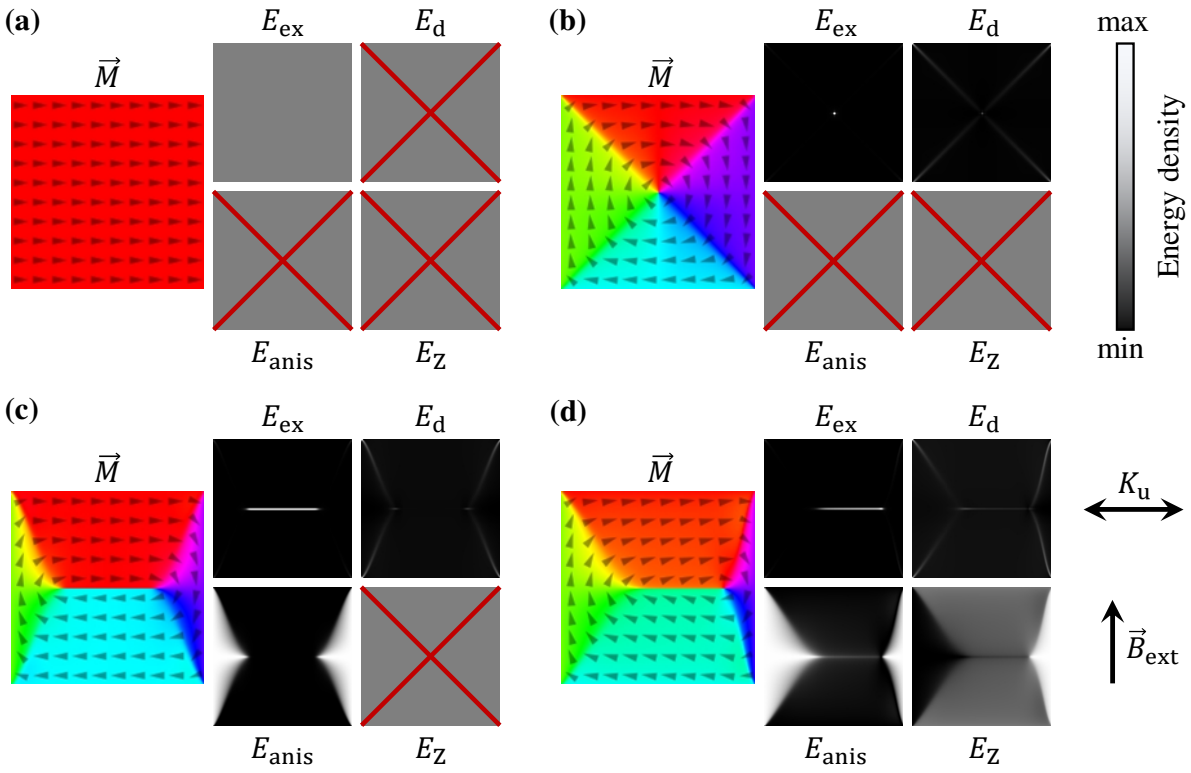

Fig.1.1: Simulated configurations of magnetization in a $3 \times 3\ \mu m^2$ square caused by gradually adding the different interactions to illustrate their effect. **(a)** Magnetization configuration when only the exchange interaction is included. The magnetization is parallel everywhere and consequently the exchange energy density is zero everywhere. **(b)** Configuration with added demagnetizing/dipolar interaction. Magnetization aligns along the surfaces of the sample to avoid creation of surface charges (charge avoidance principle). The resulting vortex-like configuration (Landau pattern) has a high divergence in the center. **(c)** Addition of the uniaxial easy-axis anisotropy in the left-right direction leads to an expansion of the domains, in which the magnetization is aligned along this axis. **(d)** Including an external field applied pointing to the top shrinks the domain, where the field and magnetization is antiparallel and expands the one in which they are parallel. In the two remaining domains the field slightly tilts the magnetization from the easy axis.

1.2 Magnetic order and dynamics

This section is dedicated to introducing first the equations governing the static magnetic order along with the concept of effective magnetic field, which contains contributions from all magnetic interactions. Then, the Landau-Lifschitz-Gilbert equation, which describes also the temporal evolution of magnetic systems, is presented.

1.2.1 Static micromagnetism and effective field

The total (Gibbs free) energy density E is the following sum of the aforementioned contributions

$$E = E_Z + E_d + E_{ex} + E_{anis} + E_{me}. \tag{1.20}$$

The equilibrium magnetization configuration corresponds to the state of minimal total energy, which is obtained as an integral of the total energy density over the volume of the magnetic system. The total energy is therefore a functional of the function $E\left[\vec{M}(\vec{r})\right]$ and proper treatment of this problem relies on variational calculus. Variations to the valid solutions of magnetization $\vec{M}(\vec{r})$ must lead to zero variation to the total energy. There can be more than one valid solution, for example a very thin rod without any anisotropy or external field can be magnetized in either direction along its axis. After inclusion of condition securing the size of magnetization to be constant $\left|\vec{M}(\vec{r})\right| = M_S$ we can attain from the variational equation the desired differential equations[1] for the equilibrium state [6]

$$\vec{M} \times \vec{H}_{\mathrm{eff}} = \vec{0}, \tag{1.21}$$

where we use the effective magnetic field $\vec{H}_{\mathrm{eff}}$. This equation implies, that the magnetization must be parallel to the effective field at every point in space. Effective field is derived from the total energy density as [6]

$$\vec{H}_{\mathrm{eff}} = -\frac{1}{\mu_0}\frac{\partial E}{\partial \vec{M}} = \vec{H}_{\mathrm{Z}} + \vec{H}_{\mathrm{d}} + \frac{2A_{\mathrm{ex}}}{\mu_0 M_S}\vec{\nabla}^2\vec{m} + \vec{H}_{\mathrm{anis}} + \vec{H}_{\mathrm{me}}, \tag{1.22}$$

with the last two terms representing the effective fields of crystalline and magnetoelastic anisotropy, defined naturally as

$$\vec{H}_{\mathrm{anis}} = -\frac{1}{\mu_0}\frac{\partial E_{\mathrm{anis}}}{\partial \vec{M}}\,, \vec{H}_{\mathrm{me}} = -\frac{1}{\mu_0}\frac{\partial E_{\mathrm{me}}}{\partial \vec{M}}. \tag{1.23}$$

In the common situation of magnetization being aligned along the easy axis we can express the effects of anisotropy in the sometimes-convenient terms of anisotropy field. This construct produces the same torque on magnetic moments as the torque caused by the proper effective field of anisotropy, when the magnetization deviates from the easy axis only slightly. The anisotropy field is parallel to the easy direction and its magnitude is given by the following equations in cubic crystals [11, p. 226]

$$H_{\mathrm{c},\langle 100\rangle} = \frac{2K_{\mathrm{c1}}}{\mu_0 M_S}, \tag{1.24}$$

for the easy axes $\langle 100\rangle$ (positive K_{c1}) and for easy axes $\langle 111\rangle$ (negative K_{c1})

$$H_{\mathrm{c},\langle 111\rangle} = \frac{-4(3K_{\mathrm{c1}} + K_{\mathrm{c2}})}{9\mu_0 M_S}. \tag{1.25}$$

Likewise, in systems with uniaxial anisotropy the anisotropy field is

$$H_{\mathrm{uni}} = \frac{2K_{\mathrm{u}}}{\mu_0 M_S}. \tag{1.26}$$

The uniaxial anisotropy field has additional meaning – it is equal to the external field required to saturate the magnetization in the hard plane when K_{u2} is zero.

We can also calculate the proper effective field of uniaxial anisotropy by rewriting (1.15) using a unit vector pointing along the axis of anisotropy $\vec{e}_{\mathrm{uni}}$ as $E_{\mathrm{uni}} = K_{\mathrm{u}}[1 - (\vec{m}\cdot\vec{e}_{\mathrm{uni}})^2]$ and by performing the derivation (1.23)

[1] Additional equation $\vec{M} \times \vec{\nabla}_n \vec{M} = \vec{0}$ must be fulfilled on the surface [6].

$$\vec{H}_{\mathrm{uni}} = -\frac{1}{\mu_0}\frac{\partial E_{\mathrm{uni}}}{\partial \vec{M}} = \frac{2K_{\mathrm{u}}}{\mu_0 M_S}(\vec{m}\cdot\vec{e}_{\mathrm{uni}})\vec{e}_{\mathrm{uni}}. \tag{1.27}$$

We will be interested in an anisotropy with axis lying in the *xy*-plane. The unit vector of such anisotropy can be written using the angle between the *y*-axis and the anisotropy-axis φ as

$$\vec{e}_{\mathrm{uni}} = \sin\varphi\,\vec{e}_{\mathrm{x}} + \cos\varphi\,\vec{e}_{\mathrm{y}}. \tag{1.28}$$

Performing the multiplications in (1.27) leads to

$$\vec{H}_{\mathrm{uni}} = \frac{2K_{\mathrm{u}}}{\mu_0 M_S}\begin{pmatrix} m_x\sin^2\varphi + m_y\sin\varphi\cos\varphi \\ m_x\sin\varphi\cos\varphi + m_y\cos^2\varphi \\ 0 \end{pmatrix}. \tag{1.29}$$

This can be written using matrix multiplication, which allows us to introduce the tensor of uniaxial anisotropy $\widehat{N}_{\mathrm{uni}}$, in our case

$$\vec{H}_{\mathrm{uni}} = -\widehat{N}_{\mathrm{uni}}\vec{M} = -\frac{2K_{\mathrm{u}}}{\mu_0 M_S^2}\begin{pmatrix} -\sin^2\varphi & -\sin\varphi\cos\varphi & 0 \\ -\sin\varphi\cos\varphi & -\cos^2\varphi & 0 \\ 0 & 0 & 0 \end{pmatrix}\begin{pmatrix} M_x \\ M_y \\ M_z \end{pmatrix}. \tag{1.30}$$

1.2.2 Magnetization dynamics

Equation (1.21) remarkably resembles the expression of torque $\vec{T}$, which acts on a magnetic moment $\vec{\mu}$ in magnetic field $\vec{H}_{\mathrm{ext}}$

$$\vec{T} = \mu_0\vec{\mu}\times\vec{H}_{\mathrm{ext}}. \tag{1.31}$$

According to classical mechanics, torque causes the angular momentum $\vec{L}$ to change over time.

$$\frac{\mathrm{d}\vec{L}}{\mathrm{d}t} = \vec{T} = \mu_0\vec{\mu}\times\vec{H}_{\mathrm{ext}}. \tag{1.32}$$

Additionally, considering a simple model of a rotating charged object, which by the laws of classical electrodynamics and mechanics has a magnetic moment $\vec{\mu}$ and an angular momentum $\vec{L}$ created by its rotation, allows us to link these two quantities of the object by the gyromagnetic ratio γ[1] as $\vec{\mu} = \gamma\vec{L}$. By combining these ideas, we arrive at the equation of motion for the magnetic moment of the object

$$\frac{\mathrm{d}\vec{\mu}}{\mathrm{d}t} = \gamma\mu_0\vec{\mu}\times\vec{H}_{\mathrm{ext}}. \tag{1.33}$$

In light of this equation, we can unsurprisingly interpret (1.21) as describing states with zero torque and therefore states, that are static due to the moments being aligned parallel to the field. A moment not aligned this way would perform the Larmor precession around the magnetic field at the angular frequency $\omega = \gamma\mu_0 H_{\mathrm{ext}}$.

Problem with equation (1.33) as the equation of motion for magnetization is its derivation inside classical physics, which leads to an error in the gyromagnetic ratio if we wanted to apply it on electrons and their spins. It also doesn't include effects of other interactions, such as the exchange interaction. A more solid quantum-mechanical derivation of the equation guiding the time evolution of the mean value of the spin of an electron [12] rewards us with the proper

[1] Classical objects with identical distributions of charge and mass have the gyromagnetic ratio equal to $q/2m$. The gyromagnetic ratio in the LLG equation is concerned with spins and magnetic moments of negatively charged electrons and has the negative sign explicitly taken out, resulting in additional minus sign in the equation.

gyromagnetic ratio, which includes the g-factor g. This gyromagnetic ratio is given by $-\gamma = -ge/2m_e$ (including the minus sign). Where m_e is the electrons mass, e is the (positive) elementary charge and the dimensionless g-factor is usually around 2, but varies slightly across materials. Moreover, the inclusion of additional interactions can be achieved by establishing the equation of motion by means of Hamilton's principle of stationary action using a Lagrangian, which consists of the sum of previously mentioned contributions to the total free energy as the potential energy and of a clever expression made of magnetization and the proper gyromagnetic ratio representing the kinetic energy [5]. The result exploits the concept of effective magnetic field again and is called the Landau-Lifschitz equation of motion

$$\frac{\partial \vec{M}}{\partial t} = -\gamma \mu_0 \vec{M} \times \vec{H}_{\text{eff}}. \tag{1.34}$$

Motion satisfying this equation could theoretically continue into eternity. Real systems are subject to some energy dissipation. In magnetization dynamics, the dissipation is typically incorporated using an approach introduced by Gilbert, who added additional phenomenological damping term to this equation. This damping is quantified using the Gilbert damping parameter α, a material constant. Finally, the Landau-Lifschitz-Gilbert (LLG) equation of motion reads

$$\frac{\partial \vec{M}}{\partial t} = -\gamma \mu_0 \vec{M} \times \vec{H}_{\text{eff}} + \frac{\alpha}{M_S} \vec{M} \times \frac{\partial \vec{M}}{\partial t}. \tag{1.35}$$

This equation can be rewritten to carry the time derivative only on one side as [13]

$$(1+\alpha^2)\frac{\partial \vec{M}}{\partial t} = -\gamma \mu_0 \vec{M} \times \vec{H}_{\text{eff}} - \frac{\gamma \mu_0 \alpha}{M_S} \vec{M} \times \left(\vec{M} \times \vec{H}_{\text{eff}}\right). \tag{1.36}$$

Fig.1.2 (a) depicts the typical movement of magnetization slightly misaligned from its equilibrium. The first term of LLG equation causes the magnetization to precess around the effective field and addition of the second, damping term leads (without continuous excitation) to a spiral trajectory. In many spatially confined structures, the precession is rather elliptical.

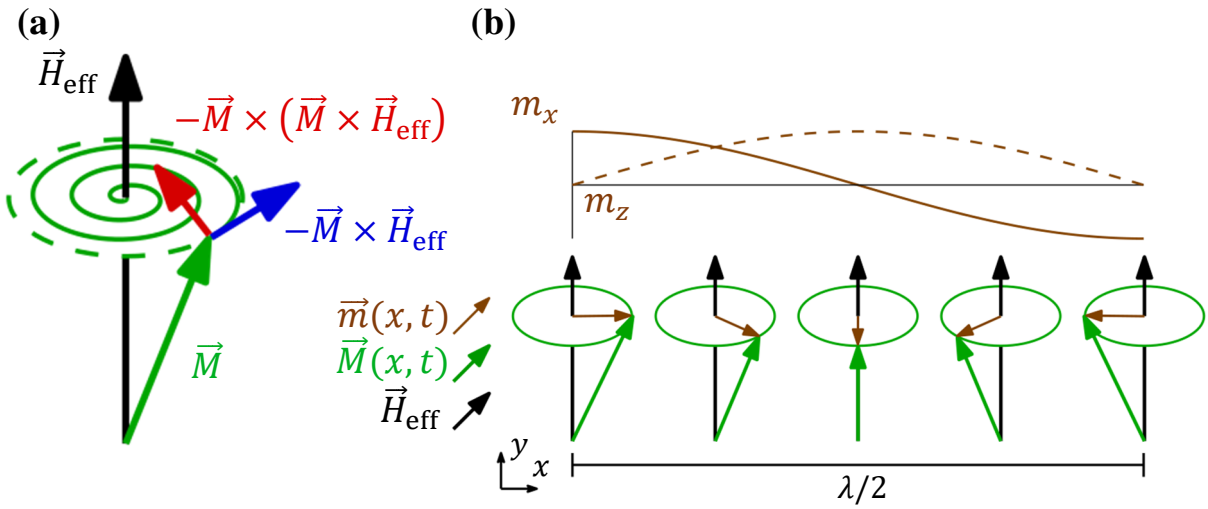

Fig.1.2: **(a)** Precession of magnetization (green) around an effective field (black) with the "torque" term (blue), which drives the precession, and the damping term (red), which makes the magnetization move towards the equilibrium configuration. **(b)** Scheme of a spin wave propagating to the right. The dynamical part $\vec{m}$ (brown) is very small compared to the saturation magnetization and the precession is right-handed with the temporal evolution.

1.3 Spin waves

The dipolar and exchange interactions couple spins/magnetization at different locations of a magnetic sample, which allows excitations of the magnetic order to propagate through the magnetic material. If these excitations have a small amplitude (in the sense, that we can neglect nonlinear terms in the LLG equation), the LLG equation allows a wave solution in the form of spin waves. Spin waves can be characterized by their (angular) frequency ω and wave vector $\vec{k}$ and their (bosonic) quasiparticles magnons carry the energy $E_{\text{magnon}} = \hbar\omega$ and momentum $\vec{p}_{\text{magnon}} = \hbar\vec{k}$. Spin waves have the character of precession, whose phase changes over time and space as is illustrated in Fig.1.2 (b). In ferromagnets the time evolution of this precession is always right-handed.

In this section we will provide a derivation of the magnetostatic spin wave dispersion relation, which exhibits a strong anisotropic character due to the demagnetization (dipolar) field. Then a more general dipole-exchange dispersion will be presented and spin wave group velocity with propagation length will be discussed. At the end, relevant experimental and theoretical findings about the refraction and steering of spin waves will be reviewed.

1.3.1 Dispersion relation

We begin by outlining the geometry of our problem of spin wave propagation in in-plane magnetized thin films as shown in Fig.1.3. The thin film of thickness *d* is considered to be infinite in the *x* and *y* directions and the *y*-axis is defined to be parallel with the equilibrium magnetization (and field). We will be following the derivation performed by Damon and Eshbach [14], which is based on the work of Walker [15].

Spin waves are small excitations of the magnetic order and therefore we can conveniently separate the magnetization vector into two parts – a static $\vec{M}_0$, which has the size of M_S, and dynamic $\vec{m}(\vec{r},t)$, which is small $|\vec{m}| \ll M_S$ and because size of the magnetization vector is constant $|\vec{M}| = M_S$, the $\vec{m}$ is also perpendicular to $\vec{M}_0$ in this small excitation approximation:

$$\vec{M}(\vec{r},t) = \vec{M}_0 + \vec{m}(\vec{r},t) = \begin{pmatrix} 0 \\ M_S \\ 0 \end{pmatrix} + \begin{pmatrix} m_x \\ 0 \\ m_z \end{pmatrix}. \tag{1.37}$$

The same separation can be done with the effective field, which consists of the external and demagnetization fields in our analysis (neglecting exchange and anisotropy fields for the moment). Note, that the dynamic field $\vec{h}(\vec{r},t)$ could be either of those fields, but in our analysis it will be created purely by the dipolar field of the small excitation $\vec{m}$.

$$\vec{H}(\vec{r},t) = \vec{H}_{\text{ext}} + \vec{H}_{\text{d}} = \vec{H}_0 + \vec{h}(\vec{r},t) = \begin{pmatrix} 0 \\ H_0 \\ 0 \end{pmatrix} + \begin{pmatrix} h_x \\ 0 \\ h_z \end{pmatrix}. \tag{1.38}$$

Inserting these vectors in the Landau-Lifschitz equation of motion (1.34) (neglecting damping) leads to

$$\frac{\partial(\vec{M}_0 + \vec{m})}{\partial t} = -\gamma\mu_0\left(\vec{M}_0 \times \vec{H}_0 + \vec{m} \times \vec{H}_0 + \vec{M}_0 \times \vec{h} + \vec{m} \times \vec{h}\right). \tag{1.39}$$

The first vector multiplication is zero because its vectors are parallel, and we neglect the last term because it is of second order, which also allows us to ignore any h_y. Considering the time dependence to be harmonic for the dynamic magnetization and field $\sim e^{i\omega t}$ we write

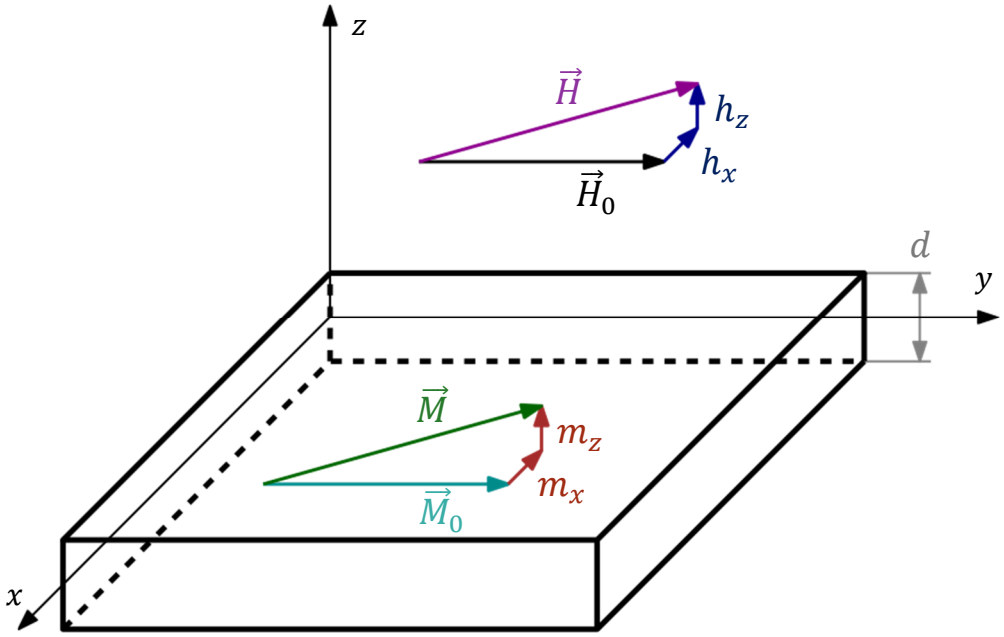

Fig.1.3: Geometry of our problem. Equilibrium magnetization and field are aligned along the *y*-axis and the thin film is infinitely extended in the *xy*-plane, in which the spin waves propagate. The film has a thickness *d* in the *z*-direction.

$$i\omega\vec{m} = -\gamma\mu_0\left(\vec{m}\times\vec{H}_0 + \vec{M}_0\times\vec{h}\right). \tag{1.40}$$

We establish the substitutions

$$\omega_H = \gamma\mu_0 H_0, \quad \omega_M = \gamma\mu_0 M_S. \tag{1.41}$$

Then, we can write the two nonzero equations from (1.40) directly with the different components as

$$i\omega m_x = \omega_M h_z - \omega_H m_z, \tag{1.42}$$

$$i\omega m_z = -\omega_M h_x + \omega_H m_x. \tag{1.43}$$

We want to obtain a dependency of the dynamic magnetization on the dynamic field components. This can be done by rearranging these two equations to

$$\begin{pmatrix} m_x \\ m_z \end{pmatrix} = \frac{\omega_M}{\omega_H^2 - \omega^2}\begin{pmatrix} \omega_H & i\omega \\ -i\omega & \omega_H \end{pmatrix}\begin{pmatrix} h_x \\ h_z \end{pmatrix}. \tag{1.44}$$

We introduce some more substitutions

$$\chi = \frac{\omega_M\omega_H}{\omega_H^2 - \omega^2}, \quad \kappa = \frac{\omega_M\omega}{\omega_H^2 - \omega^2}. \tag{1.45}$$

Using this, we can write the relation (1.44) with the susceptibility tensor $\hat{\chi}$ for all three components

$$\vec{m} = \hat{\chi}\vec{h} = \begin{pmatrix} \chi & 0 & i\kappa \\ 0 & 0 & 0 \\ -i\kappa & 0 & \chi \end{pmatrix}\vec{h}. \tag{1.46}$$

For further analysis we will need to work with the magnetic flux density, which can be also separated into a static $\vec{B}_0$ (in *y*-axis) and a small dynamic part $\vec{b}(\vec{r},t)$. The material relations connect our three quantities through the susceptibility or permeability tensors $\hat{\mu}$ as [7, p. 35]

$$\vec{b} = \mu_0\left(\vec{h} + \vec{m}\right) = \mu_0\left(\hat{1} + \hat{\chi}\right)\vec{h} = \mu_0\hat{\mu}\vec{h}. \tag{1.47}$$

According to previous equations the permeability tensors $\hat{\mu}$ is

$$\hat{\mu} = \begin{pmatrix} 1+\chi & 0 & i\kappa \\ 0 & 1 & 0 \\ -i\kappa & 0 & 1+\chi \end{pmatrix}. \tag{1.48}$$

In our case outlined in Fig.1.3, the external field is the static part $\vec{H}_0$ and the dynamic field $\vec{h}$ is composed purely from the demagnetizing field. As was discussed in subsection 1.1.2, we can introduce the magnetostatic (scalar) potential φ to describe the demagnetizing field (1.5) in the magnetostatic framework. Writing the Gauss law for magnetic flux density (1.3) for our system, we arrive at

$$\vec{\nabla} \cdot \left(\hat{\mu} \cdot \vec{\nabla}\varphi\right) = 0. \tag{1.49}$$

Writing the individual derivations of φ and performing the matrix multiplication leads to the Walker equation

$$(1+\chi)\left[\frac{\partial^2\varphi}{\partial x^2} + \frac{\partial^2\varphi}{\partial z^2}\right] + \frac{\partial^2\varphi}{\partial y^2} = 0. \tag{1.50}$$

Outside of the thin film $\chi = 0$ and (1.50) takes the form of Laplace's equation. These equations can be solved by separation of variables [14], where the individual parts then lead to solutions by complex exponentials. Boundary conditions, which will be mentioned in a moment, will require the exponentials to have the same wave vector for the *x* and *y* directions and only in the perpendicular direction the solution is different in the three regions (below, in and above the thin film). Considering geometry of the problem, the potential inside the film will be

$$\varphi^i = \left[A\sin\left(k_z^i z\right) + B\cos\left(k_z^i z\right)\right]\mathrm{e}^{ik_x x + ik_y y}. \tag{1.51}$$

Above ($z > d/2$) the film the solution will be

$$\varphi^e = C\mathrm{e}^{-k_z^e z}\mathrm{e}^{ik_x x + ik_y y}. \tag{1.52}$$

And below ($z < d/2$)

$$\varphi^e = D\mathrm{e}^{k_z^e z}\mathrm{e}^{ik_x x + ik_y y}. \tag{1.53}$$

Inserting these solutions back into (1.50) yields first equations necessary for exploration of the spin wave dispersion relation

$$(1+\chi)\left[k_x^2 + k_z^{i,2}\right] + k_y^2 = 0, \tag{1.54}$$

$$k_x^2 + k_y^2 - k_z^{e,2} = 0. \tag{1.55}$$

No dissipation of energy is included in our model and so the wave vectors k_x and k_y must be real. Additionally, to avoid diverging solutions in (1.52) and (1.53), $k_z^e > 0$ must be fulfilled. The k_z^i can be real or imaginary, with the former corresponding to volume modes and the latter to surface modes.

Two boundary conditions must be met at the interfaces at $z = \pm d/2$. First, the normal component of the magnetic flux density must be continuous, which can be expressed using (1.47) and (1.5) as

$$-i\kappa\frac{\partial\varphi^i}{\partial x} + (1+\chi)\frac{\partial\varphi^i}{\partial z}\bigg|_{z=\pm d/2} = \frac{\partial\varphi^e}{\partial z}\bigg|_{z=\pm d/2}. \tag{1.56}$$

And second, the tangential component of magnetic field must be continuous, which can be expressed (due to the same *x* and *y* dependency of φ^i and φ^e) simply as

$$\varphi^i\big|_{z=\pm d/2} = \varphi^e|_{z=\pm d/2}. \tag{1.57}$$

Inserting (1.51), (1.52) and (1.53) into (1.57) can be used to determine the dependency of amplitudes of the potential A and B on amplitudes C and D. Then, solving the two equations (1.56) for C/D and equating them results in a new equation for the wave vectors [14]

$$k_z^{e,2} + 2k_z^i k_z^e(1+\chi)\cot\left(k_z^i d\right) - k_z^{i,2}(1+\chi)^2 - (\kappa k_x)^2 = 0. \tag{1.58}$$

Equations (1.58), (1.54) and (1.55) determine the allowed values of $\omega, k_x, k_y, k_z^i, k_z^e$, that is, the mode spectrum, for a given set of parameters H_0, M_S, d. Two variables can be further eliminated, and we could obtain one equation for ω, k_x, k_y [14]. Unfortunately, we cannot arrive at an explicit dispersion relation $\omega(k_x, k_y)$ this way and the implicit function has a very complicated form. Therefore, in the following we will constrict ourselves on inspection of two characteristic cases of spin wave propagation, which show the anisotropy of their dispersion relation.

In the first case, the direction of propagation of spin waves in plane of the film is perpendicular to the equilibrium magnetization. We call these waves magnetostatic surface spin waves, or the Damon-Eshbach mode. According to the direction of propagation, we set $k_y = 0$. To satisfy equations (1.54) and (1.55) the wave vector components must be equal to

$$k = k_x = k_z^e = \frac{k_z^i}{i}, \tag{1.59}$$

where we introduce k for simplicity. It is apparent from (1.59), that in the film the wave will have an exponential profile. Waves traveling in one direction will localize at one interface and decay into the film while waves propagating in the opposite direction will localize on the other interface [16]. Hence the name surface waves. The boundary conditions (1.57) then take the form

$$A\sin(ikd/2) + B\cos(ikd/2) = C\mathrm{e}^{-kd/2}, \tag{1.60}$$

$$-A\sin(ikd/2) + B\cos(ikd/2) = D\mathrm{e}^{-kd/2}. \tag{1.61}$$

Likewise, the boundary conditions (1.56) then read

$$\kappa k\left[A\sin\left(\frac{ikd}{2}\right) + B\cos\left(\frac{ikd}{2}\right)\right] + i(1+\chi)k\left[A\cos\left(\frac{ikd}{2}\right) - B\sin\left(\frac{ikd}{2}\right)\right] = -kC\mathrm{e}^{-kd/2}, \tag{1.62}$$

$$\kappa k\left[-A\sin\left(\frac{ikd}{2}\right) + B\cos\left(\frac{ikd}{2}\right)\right] + i(1+\chi)k\left[A\cos\left(\frac{ikd}{2}\right) + B\sin\left(\frac{ikd}{2}\right)\right] = kD\mathrm{e}^{-kd/2}. \tag{1.63}$$

By inserting the first two equations into the second two equations to eliminate C and D and by rearranging the result, we can arrive at equations for A and B in the format

$$\begin{pmatrix} i\chi\cos\left(\frac{ikd}{2}\right) + i\mathrm{e}^{\frac{kd}{2}} & \kappa\cos\left(\frac{ikd}{2}\right) \\ \kappa\sin\left(\frac{ikd}{2}\right) & -i\chi\sin\left(\frac{ikd}{2}\right) + \mathrm{e}^{\frac{kd}{2}} \end{pmatrix}\begin{pmatrix} A \\ B \end{pmatrix} = \begin{pmatrix} 0 \\ 0 \end{pmatrix}. \tag{1.64}$$

For nontrivial solution, the rows of the matrix must be linearly dependent. Therefore, we continue our derivation by calculating the determinant of this matrix and by setting it to be zero. Then by finding the positive root of the resulting quadratic polynomial for ω^2 we receive the dispersion relation of the Damon-Eshbach mode

$$\omega^2 = \omega_H(\omega_H + \omega_M) - \frac{\omega_M^2}{4}(\mathrm{e}^{-2kd} - 1). \tag{1.65}$$

The second case deals with waves traveling parallel to the equilibrium magnetization, the backward volume waves. Their dispersion relation can be obtained using the same approach as for the surface waves, but the solution inside the film will be sinusoidal instead of exponential and we would have to deal with more solutions corresponding to different profiles [17, p. 159]. Dispersion relation of the lowest order backward volume mode is [17, p. 159]

$$\omega^2 = \omega_H\left(\omega_H + \omega_M \frac{1 - \mathrm{e}^{-kd}}{kd}\right). \tag{1.66}$$

Dispersions of these two borderline cases are plotted in Fig.1.4 (a). The surface waves have the steepest incline and the backward volume waves exhibit the steepest decline in their dispersion of all possible directions of propagation. As will be discussed later, the negative slope of the dispersion means that the group velocity will have the opposite direction from the wave vector and phase velocity, hence the adjective backward. Waves traveling at intermediate angles between these two cases will continuously change their character from backward volume waves to surface waves.

It is clear from geometrical considerations of the tangentially magnetized film, that for $k \to 0$ frequencies of both modes should match. This uniform precession mode is called ferromagnetic resonance and its (angular) frequency is

$$\omega_{\mathrm{FMR}} = \sqrt{\omega_H(\omega_H + \omega_M)} = \gamma\mu_0\sqrt{H_0(H_0 + M_S)}. \tag{1.67}$$

In our analysis we have presumed, that H_0 is made purely by H_{ext}, but in the simple case of the external field being aligned along the easy axis of an anisotropy we can add the anisotropy field [e.g. (1.26)] simply as $H_0 = H_{\mathrm{ext}} + H_{\mathrm{uni}}$. If the effective field of the equilibrium $\vec{H}_0$ consists of nonparallel contributions, then the static external field gets expressed only in the component parallel to the equilibrium magnetization $H_{\mathrm{ext}} \to H_{\mathrm{ext}}\cos(\varphi_H)$ as its components in other directions get cancelled by the other effective field contributions, such as from anisotropy. However, effects of these other contributions are better not to be argued for this way because they influence the system also through $\vec{h}$, which deserves a proper treatment and effects of the static and small dynamic components get mixed in the resulting dispersion.

A more general derivation of dispersion relation for spin waves in thin films was done by Kalinikos and Slavin [9], whose model also included the exchange interaction. Later they also included the effects of magnetocrystalline anisotropy [18]. Following their results, we can calculate the frequency of spin waves in in-plane magnetized thin films from the in-plane wave vector of magnitude $k = \sqrt{k_x^2 + k_y^2}$ and direction $\varphi_{\vec{k}} = \mathrm{atan}\,(k_x/k_y)$ and from the in-plane uniaxial anisotropy and external field, which have their axis/direction tilted from the equilibrium magnetization by φ_K and φ_H, as[1]

[1] We have retrieved (1.68) from eq. (27) in [18] for the first (uniform) mode with unpinned/free boundary spins and the anisotropy tensor in (1.30) describing an easy-axis uniaxial anisotropy in the film plane (It should be noted that [18] uses different labeling of axes). The angles φ_K and φ_H could be found by solving the static energy-minimization problem first.

$$\omega = \gamma\mu_0 \sqrt{\left[H_{\text{ext}}\cos(\varphi_H) + \frac{2A_{\text{ex}}}{\mu_0 M_S}k^2 + \frac{2K_{\text{u}}}{\mu_0 M_S}\cos^2(\varphi_K) + M_S(1-P)\right]} \cdot \sqrt{\left[H_{\text{ext}}\cos(\varphi_H) + \frac{2A_{\text{ex}}}{\mu_0 M_S}k^2 + \frac{2K_{\text{u}}}{\mu_0 M_S}\cos(2\varphi_K) + M_S P\sin^2(\varphi_{\vec{k}})\right]}. \tag{1.68}$$

The parameter P is defined as

$$P = 1 - \frac{1 - \mathrm{e}^{-kd}}{kd}. \tag{1.69}$$

We can see in (1.68), that the exchange interaction adds a quadratic term to the dispersion relation and that this effect is isotropic with respect to the propagation direction. The quadratic form of this term corresponds to the short-range nature of the exchange interaction. Short wavelength waves are dominated by it and are consequently called exchange spin waves, but it is negligible for long wavelengths, that are dominated by the long-range demagnetizing field and are called dipole or magnetostatic spin waves. As was already shown for the purely magnetostatic waves in Fig.1.4 (a), the dipolar interaction introduces anisotropy in the dispersion relation, which is apparent again in (1.68) from the last term. Finally, the anisotropic dipole-exchange spin wave spectrum calculated from (1.68) is displayed in Fig.1.4 (b).

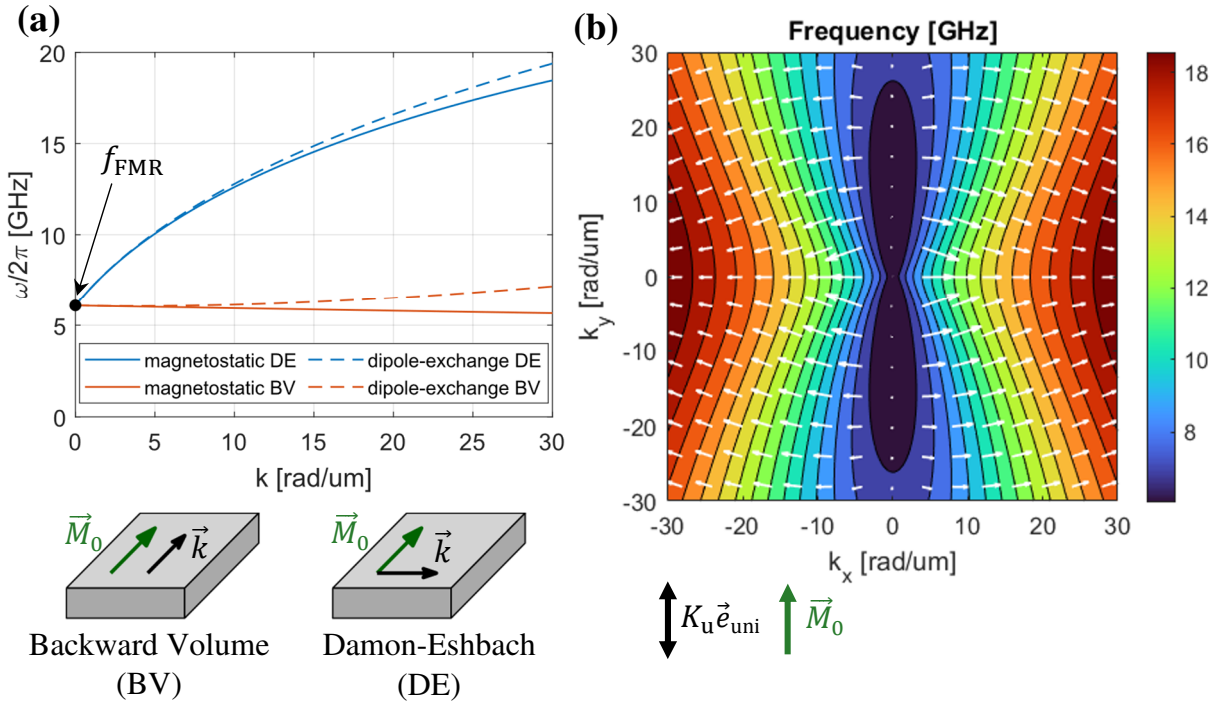

Fig.1.4: **(a)** Dispersion relations of spin waves calculated from the magnetostatic models (1.65) and (1.66) (full lines) and the dipole-exchange dispersion obtained from (1.68) (dashed lines). All curves meet at $k = 0$ corresponding to the spatially uniform ferromagnetic resonance. **(b)** Two-dimensional dispersion relation from (1.68), which shows the dependency of spin wave frequency on the in-plane wave vector. The strong anisotropy of frequency on the propagation direction is caused by the dipolar interaction. White arrows show the group velocity. Following parameters were used: $\gamma = 2\pi \cdot 29.3$ rad/Ts, $M_S = 1\,410$ kA/m, $A_{\text{ex}} = 11$ pJ/m, $d = 10$ nm, $H_{\text{ext}} = 0$ T, $K_{\text{u}} = 16.92$ kJ/m^3.

1.3.2 Group velocity and propagation length

The phase of precession of a spin wave changes along the direction of the wave vector $\vec{k}$ and by using the frequency we can also express the speed of the wave's wavefront with a quantity called phase velocity

$$\vec{v}_{\mathrm{ph}} = \frac{\omega}{\vec{k}}. \tag{1.70}$$

Moreover, when dealing with a wave packet localized around a mode $\omega, \vec{k}$ we can define its group velocity $\vec{v}_{\mathrm{g}}$, which directs propagation of the packet in the real space, as

$$\vec{v}_{\mathrm{g}} = \frac{\partial \omega}{\partial \vec{k}}. \tag{1.71}$$

We have displayed the group velocity of spin waves in a thin film on top of their dispersion relation in Fig.1.4 (b). Anisotropy of the dispersion relation causes that the phase and group velocities are generally not parallel. For the backward volume waves the group velocity is (small and) even antiparallel to the phase velocity. Furthermore, spin wave modes in large areas of the reciprocal space exhibit group velocities that are almost parallel causing interesting phenomena such as the formation of caustic beams [19].

Related to the group velocity is the decay length of spin waves l_{pl}, that is commonly defined as the distance, after which the propagating waves amplitude attenuates by $1/e$. A more basic concept is the relaxation time (sometimes lifetime) τ, again defined by the attenuation by the factor of $1/e$. A spin wave packet of group velocity v_{g} and relaxation time τ will have the decay length

$$l_{\mathrm{pl}} = v_g \tau. \tag{1.72}$$

The relaxation time is connected to the damping parameter α in the LLG equation and the modes frequency. A uniform precession of magnetization without the presence of continuous excitation will attenuate by $1/e$ after [17, p. 171]

$$\tau_0 = \frac{1}{\alpha \omega}. \tag{1.73}$$

More generally, relaxation time of a spin wave can be calculated as [17, p. 172]

$$\frac{1}{\tau} = \frac{1}{\tau_0} \frac{\partial \omega}{\partial \omega_H}. \tag{1.74}$$

The main conclusion regarding the propagation length is, that if we want to propagate the waves over greater distances, we need to have high group velocity, which is achieved for the magnetostatic waves by working near the Damon-Eshbach mode [as can be seen in Fig.1.4 (b)], by using materials with higher saturation magnetization M_S and by depositing thicker magnetic layers (as can be seen from the dependencies on kd in the dispersion relations), furthermore, we need materials with low intrinsic damping α and we want to operate at rather lower frequencies ω.

1.3.3 Refraction and steering of spin waves

Refraction and reflection are common phenomena of waves arriving at interfaces separating distinct media, in which they have different dispersion relations, or more specifically, in which the allowed wave vectors on the wave's frequency are different. The most known example of this is the refraction of light between air and glass or water. This example is simple in the fact, that the dispersions on both sides are isotropic and the only difference is the difference in the refraction index, which dictates the ratio of wave vector in the given medium to the light's wave vector in vacuum. Refraction of spin waves is much more complicated, because the dispersion relations are, on top of the differences caused by different material and geometrical parameters, anisotropic, as was shown in Fig.1.4 (b).

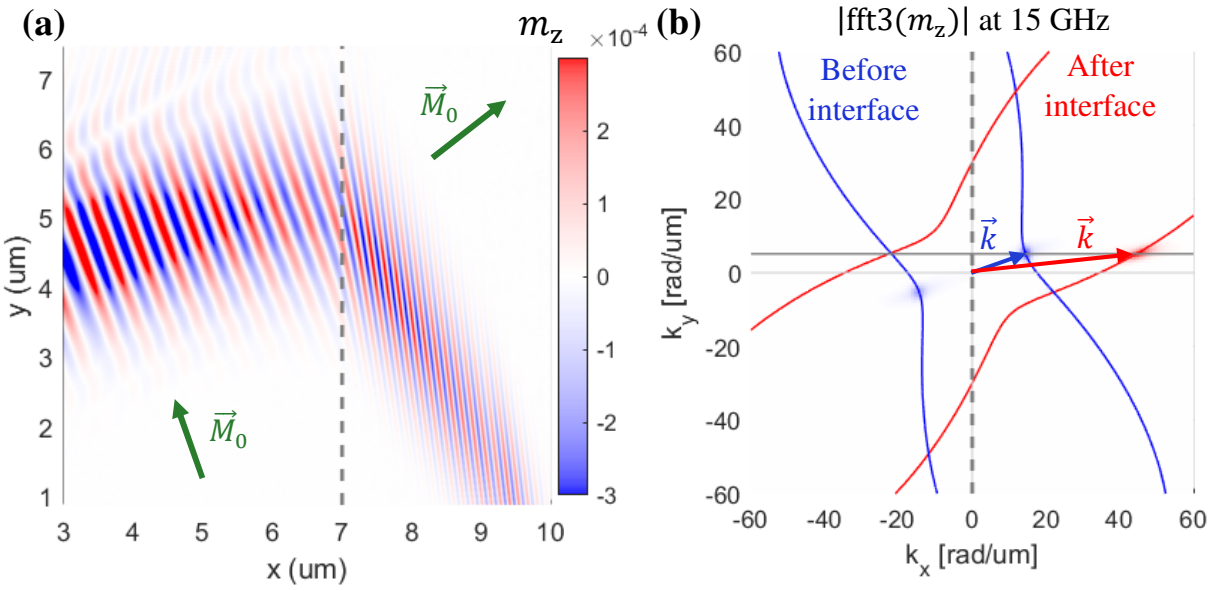

Fig.1.5: Micromagnetic simulation demonstrating refraction of spin waves. **(a)** A (Damon-Eshbach) spin wave with a gaussian profile is excited in the left region and refracts on the highlighted interface. Angle between directions of the anisotropies is 70°, other parameters are constant. Refraction of waves back into the initial propagation direction along the interface is sometimes called negative refraction. **(b)** Simulated response of m_z was Fourier transformed in three dimensions (x,y,t) in the two regions separately and we looked at the excitation frequency (15 GHz). We color-code the results to show both regions in one graph with blue color belonging to the space before (left of) interface and red to region behind interface. The blue peak clearly shows that the incident wave is of the Damon-Eshbach mode. Wave vector component parallel to the interface (dashed line) is preserved during refraction. Spin wave behind the interface (red mode) then propagates in the direction given by its group velocity [that is perpendicular to the isofrequency lines as ruled by (1.71)] and its phase changes in the direction of its wave vector. Isofrequency lines in the two regions were calculated using (1.68). Following parameters were used: $\omega/2\pi = 15$ GHz, $\gamma = 2\pi \cdot 29.3$ rad/Ts, $M_S = 1\,410$ kA/m, $A_{\mathrm{ex}} = 11$ pJ/m, $d = 10$ nm, $H_{\mathrm{ext}} = 0$ T, $K_{\mathrm{u}} = 16.92$ kJ/m^3 and $\alpha = 0.002$ (lower than in our real systems to focus our attention on the refraction). Direction of anisotropy in left region is 20° from the y-axis counterclockwise and in the right region 50° clockwise.

When spin waves refract on an interface, the component of the incoming wave's wave vector parallel to the interface is preserved in the refracted (transmitted) and reflected waves while in the perpendicular direction the translational symmetry is broken, and the corresponding wave vector component can change [20]. Example of a refracting spin wave is described in Fig.1.5, where the two media have the same parameters and only the direction of uniaxial anisotropy differs, which resembles one of our experimental systems (chapter 3).

Refraction of spin waves has already been studied in several systems. For example, in reference [21] the authors have investigated refraction on interfaces between yttrium-iron-garnet and trilayers of this ferrite, air and copper, whose presence alters the dispersion of spin waves. They have shown behavior of the refraction, that could be described by a refractive index dependent on the angle of incidence. They have demonstrated a negative refraction (example of which is in Fig.1.5). Other researchers [22] have simulated refraction and reflection on domain walls in the presence of the Dzyaloshinskii-Moriya interaction and they have shown a total reflection for certain incidence angles, which could be exploited for guiding of spin waves. Similar system was experimentally studied by time-resolved magneto-optical imaging [23] but without the presence of Dzyaloshinskii-Moriya interaction and at 90° domain walls instead of 180°. This investigated system was similar to one of ours and results showing the dependence of the refracted wave's wave vector angle on the incident wave vector angle are displayed in Fig.1.6 (a). Since the dispersion relation of spin waves is a function of the film's thickness, we can also observe refraction and reflection on steps in the thickness. This was thoroughly investigated by Stigloher [20], [24] in films made of permalloy by phase sensitive Brillouin light scattering microscopy and time-resolved magneto-optical Kerr effect. Main results of these experiments are summarized in Fig.1.6. The thickness step was also successfully exploited for design of a spin-wave lens [25].

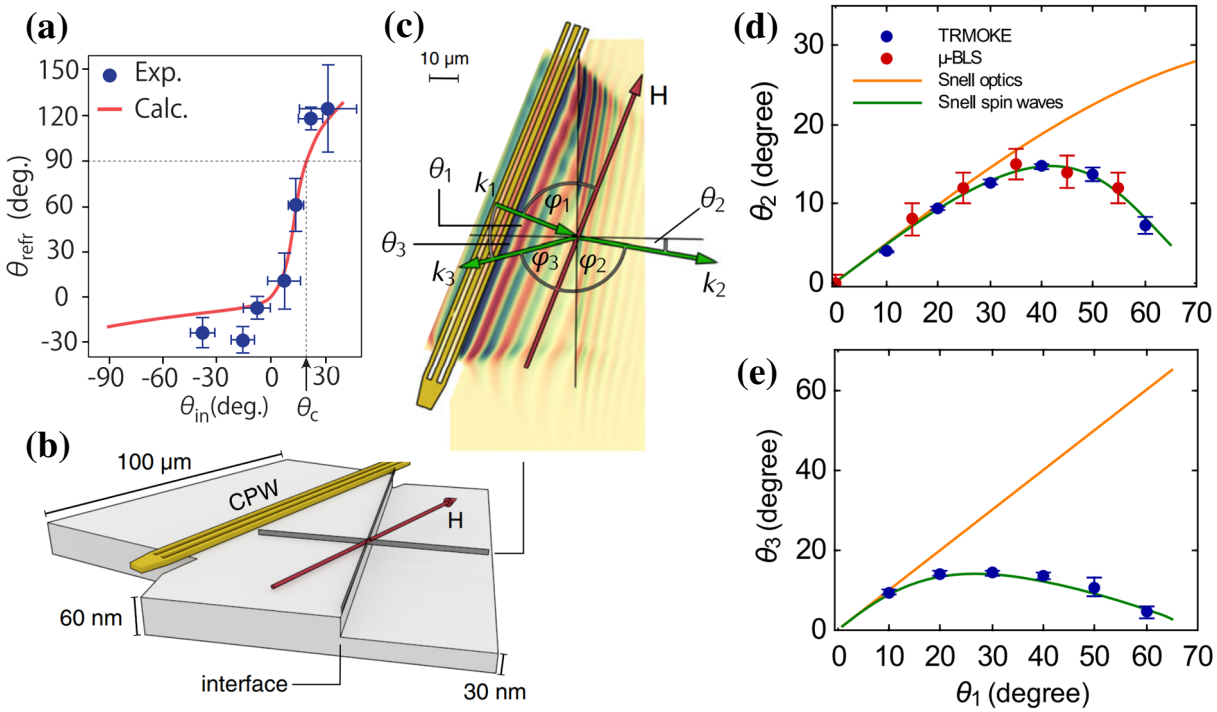

Fig.1.6: **(a)** Dependency of the refracted wave vector's angle on the incident wave's wave vector during refraction between 90° domains and domain wall separating these domains symmetrically (45° from each magnetization direction) [23]. **(b)** Geometry of experiments involving refraction on steps of the film's thickness [20]. Antenna parallel to the external field excited the Damon-Eshbach mode, which refracts on the angled step. **(c)** Top view of (b) with exemplary data and outlined wave vectors and their angles. **(d)** Experimental results of refracted waves and **(e)** reflected waves angles depending on the incident wave vector's angle [24].

Saturation magnetization M_S decreases with increasing temperature, which can be used for design of samples with continuously changing refractive index (gradient-index). Simulations have shown that rectangular regions with a specific gradient saturation magnetization can act as a focusing lens for spin waves [26]. The same researchers have also experimentally demonstrated spin-wave steering using a region with gradient saturation magnetization created by heating the region non-uniformly with a laser [27]. Frequencies of the magnetostatic backward volume and Damon-Eshbach spin waves are in a given film separate, as was already shown in Fig.1.4 (a). But lowering the saturation magnetization in the region with Damon-Eshbach waves shifts these modes to lower frequencies and can lead to a frequency overlap, which was used in the study. The authors have demonstrated that the incident backward volume wave refracts on the initial nonuniform step in saturation magnetization and then continuously transforms its wave vector component in the direction of magnetization gradient in a way, which almost leads to conversion to the Damon-Eshbach mode as is shown in Fig.1.7.

Temperature induced magnetization gradient created by laser light was also experimentally proved to focus or defocus spin waves [28]. In the experiment a spin wave beam coming from a spatially confined waveguide entered a semi-infinite area, at the beginning of which a laser spot was focused. Any mode located in the spot coming into area with different saturation magnetization must change its wave vector to satisfy the local dispersion relation on the mode's frequency and since the translational symmetry is broken in the direction of the magnetization gradient, the wave vector changes only in the local gradient's direction [Fig.1.7 (e)]. This leads to a focusing behavior for the backward volume waves [displayed in Fig.1.7 (c) and (d)] and to defocusing for the Damon-Eshbach waves [28].

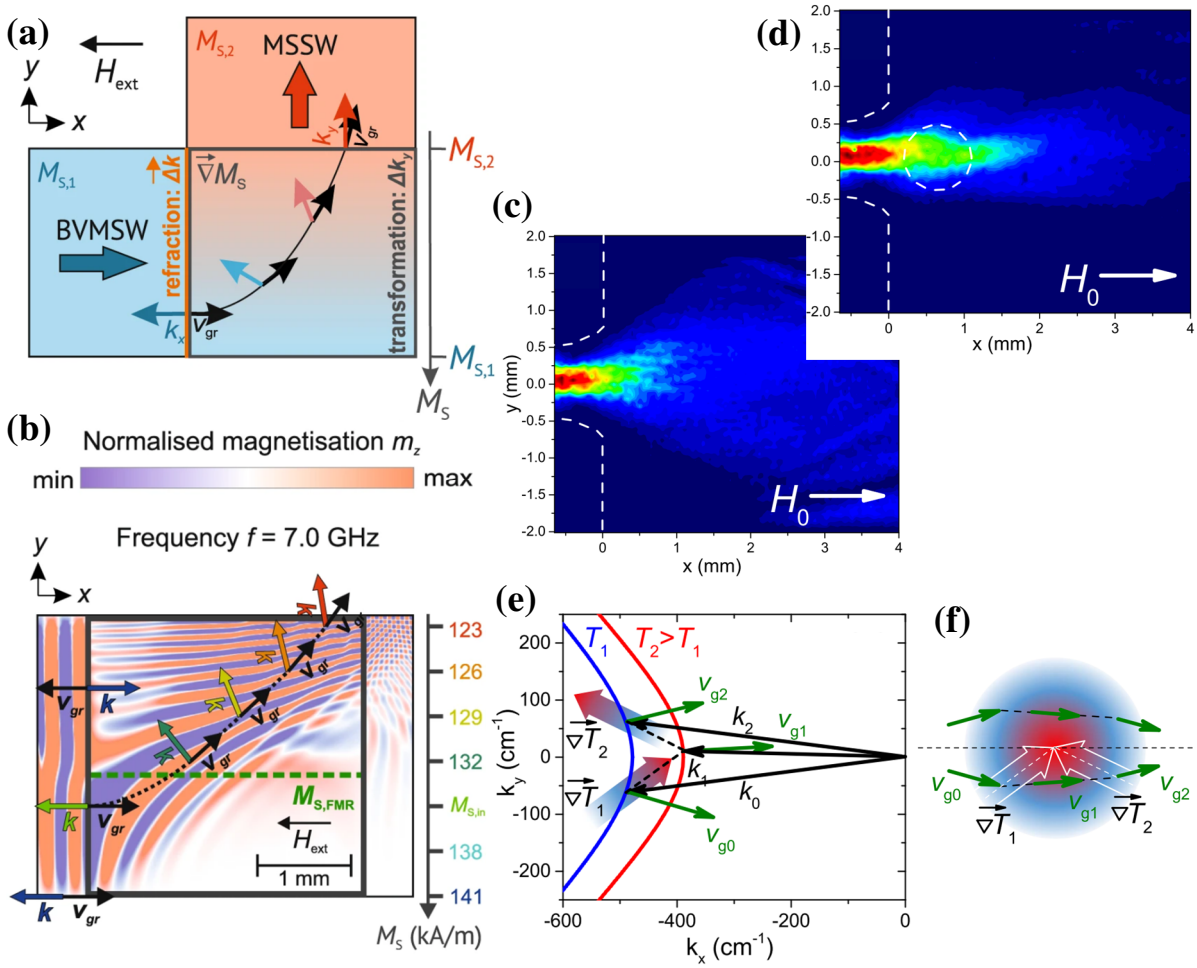

Fig.1.7: **(a)** Design of experiment for conversion of backward volume magnetostatic waves into Damon-Eshbach (magnetostatic surface) waves using a region with temperature-induced magnetization gradient [27]. **(b)** Micromagnetic simulation showcasing operation of this experiment, which was also tested using vector network analyzer – spin wave spectroscopy [27]. **(c)** BLS intensity map of a backward volume wave coming into semi-infinite area shows spread of the wave [28]. **(d)** The same incident wave is focused by a laser spot induced magnetization gradient (dashed circle corresponds to laser spot). **(e)** Scheme of mechanism leading to the focusing behavior – wave vector must match the local dispersion relation on the constant frequency and only the component parallel to the gradient can change. **(f)** Visualization of the mechanism from (e) in the real space at the laser spot – throughout the spot the wave is always changing direction of the group velocity towards the "optical axis" [28].

Alternatively, saturation magnetization can be locally modified by implantation of Ga ions [29]–[32].

Refraction of exchange spin waves was investigated in out-of-plane magnetized structures (isotropic dispersion) with gradient saturation magnetization or anisotropy strength in [33]. They have shown, using an analytical model and micromagnetic simulations, that the gradient regions can coherently refract waves at a desirable angle. This could be exploited for steering of spin waves as they have demonstrated in simulations, whose results are displayed in Fig.1.8 (a). The authors have argued that the local modification of anisotropy strength could be achieved by means of electric-field induced anisotropy [34] and variation of an insulating spacer's thickness. It was also shown by micromagnetic simulations [35], that dipole-exchange spin waves in 100 nm and 200 nm wide waveguides, which are magnetized along the edges and operate in the backward volume geometry, can pass a turn quite coherently for wavelengths of size around the width of the waveguide but scatter into more width-modes for shorter wavelengths. Unfortunately, spin waves in the backward volume geometry have short propagation length due to their low group velocity.

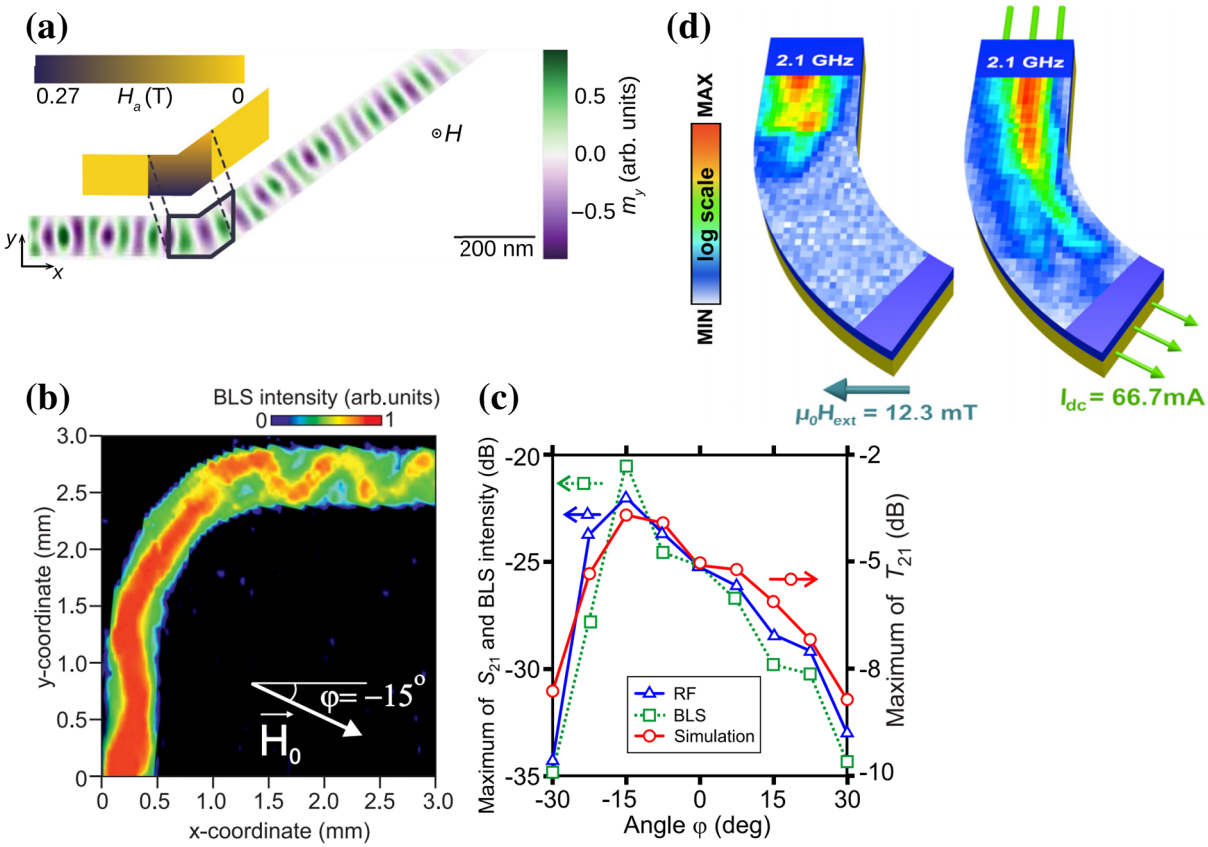

Fig.1.8: **(a)** An exchange spin wave excited left of turn coherently refracts in region with gradient of the out-of-plane uniaxial anisotropy strength [33]. **(b)** Brillouin light scattering image of intensity of a spin wave passing through a large uniformly magnetized yttrium-iron-garnet turn [36]. **(c)** Transmission of the spin-wave intensity while passing through the structure in (b) for different angles of the external field [36]. **(d)** Brillouin light scattering image of intensity of a wave reflecting from a uniformly magnetized turn and of a wave passing through the transversally magnetized turn [37]. Width of the waveguide is 2 μm and the material is permalloy, which explains the differences to (b).

Shifting our focus on magnetostatic waves, we should preview a system that could be considered the baseline for spin waves propagating through a turned waveguide – a simple turned ferromagnetic waveguide magnetized by a uniform external magnetic field. Such a system was explored in reference [36] by Brillouin light scattering, simulations, and vector network analyzer. It is clearly visible from Fig.1.8 (b), that coherency of the wave is not preserved (which is impossible due to the anisotropy of dispersion relation) and Fig1.8 (c) reveals that the intensity of transmitted waves drops significantly (however, intrinsic damping is included). The main concerns are the inhomogeneity of internal magnetic field, anisotropy of the dispersion and repeated reflections from borders of the waveguide [36]. The importance of inhomogeneity of the internal magnetic field (that is, external plus demagnetizing field) was also explored in spin-wave T-junctions by time-resolved magneto-optical Kerr microscope and simulations [38], which show the possibility to steer the wave into the desired arm of the junction.

A good idea to resolve the issues with inhomogeneity of the internal field and to maintain the spin wave in the desired mode (Damon-Eshbach with high group velocity and propagation length) is to make the magnetization align transversally to the waveguide in every position of the turned waveguide. This idea was examined in a system, in which the magnetization was ordered by a non-uniform external magnetic field created by current in an underlying conducting strip [37]. The spin waves reflected from the turn due to the inhomogeneity of internal field when the waveguide was magnetized by a uniform external field, but propagated through the turn if the magnetization was ordered into being transversal by the current in underlying conductor, as is displayed in Fig.1.8 (d). A significant disadvantage of this approach is the usage of current, which leads to Joule heating and the device cannot be considered low-power.

2 Techniques

The goal of this chapter is to describe the different techniques used to prepare and analyze our samples. We exclude the two fabrication techniques specific for the metastable iron-nickel system (focused ion beam induced transformation) and wavy waveguide system (corrugation created by focused electron beam induced deposition), which are outlined in their respective chapters. The following sections deal with electron beam lithography (EBL), Brillouin light scattering microscopy (BLS), Kerr microscopy and with micromagnetic simulations.

2.1 Electron beam lithography

Electron beam lithography is a very flexible and reliable technique used for fabrication of nanostructures, whose features can be (with the right process parameters) smaller than 10 nm [39]. While such resolution is not necessary for our application, as the smallest feature size is about 1 micrometer, we will still benefit from its reliability, especially when it comes to alignment of the newly created structures with regards to the existing structures.

In the first step of EBL, we lay our sample on a hot plate heated to 150 °C for a few minutes to make the surface cleaner by evaporating certain impurities (water). The sample is then placed in a spin-coater, where we first put a droplet of resist on it using a pipette and then initiate the spinning to spread the droplet into a uniform layer of resist. Our samples' sizes are around 5 mm and we use 35 µl of PMMA [poly(methyl methacrylate)] AR-P 679.04 made by *Allresist*. Running the spin-coater at 4000 rotations per minute for 55 seconds produces approximately 200-300 nm thick layer of resist. The sample is then placed back on the hot plate (150 °C) for three minutes to harden the resist.

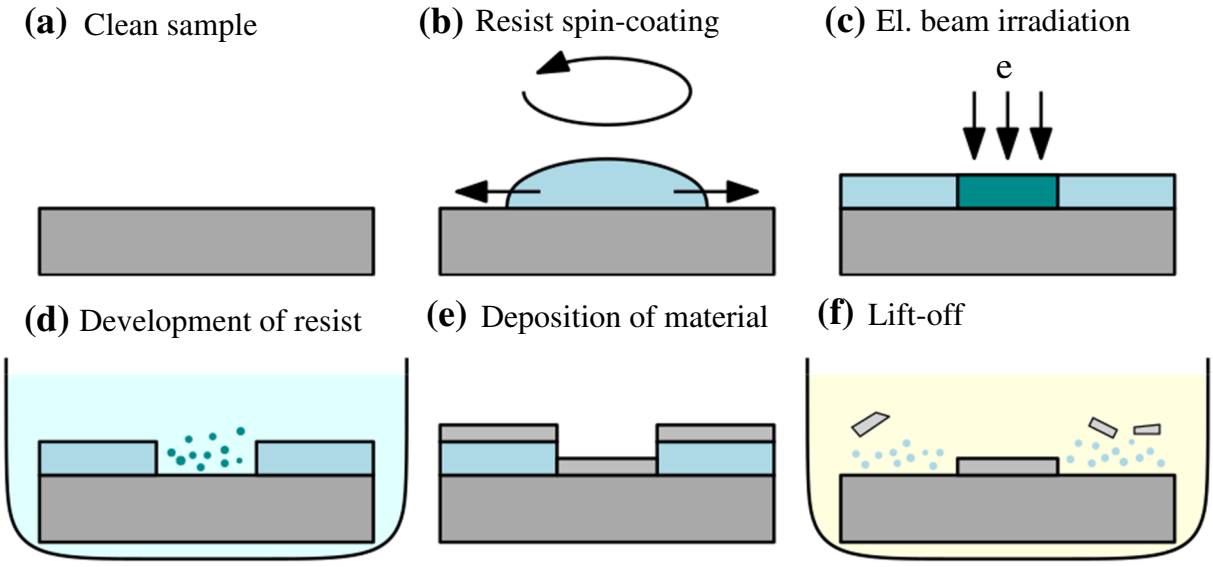

Fig.2.1: Schematic of the main steps of fabricating structures using the EBL. **(a)** We begin with a clean sample. **(b)** A droplet of resist is pipetted on the sample and the spin-coater spreads it into a uniform layer. **(c)** Electron beam irradiates chosen regions of resist. **(d)** Irradiated resist is dissolved in an appropriate chemical substance (developer). **(e)** Deposition of material in the evaporator. **(f)** Lift-off: acetone dissolves remaining resist, only the desired structure remains on the sample.

After the creation of a homogeneous layer of resist, we put the sample in the scanning electron microscope / electron beam writer (Tescan MIRA3Raith LIS). Pre-made (by EBL or focused ion beam) orientation marks help us navigate around the sample and align the structures we are fabricating with structures that are already present on the sample. Regions of planned structures are irradiated[1] by the electron beam with a dose of 220 μC/cm^2. Then, putting the sample in the appropriate developer (AR 600-56) for three minutes dissolves the irradiated resist. The development is stopped by bathing the sample in isopropyl alcohol (IPA).

At this stage we utilize the evaporator (electron beam evaporator BESTEC) to deposit layers of desired materials (permalloy or SiO_2/Cu/Au multilayer for excitation antennas). Total thickness of these layers must be smaller than thickness of the resist to keep the material grown on top of the non-irradiated resist and directly on the sample disconnected, which is fulfilled without any issues because the permalloy is always 10 nm thick, and the antenna multilayer's thickness is around 160 nm. As the final step we perform the lift-off, which is a process of dissolving the remaining resist and effectively removing also the unwanted material on top of it, while the material deposited directly on the sample remains. In our case of the organic PMMA resist we submerge the sample in acetone for at least one hour.

2.2 Brillouin light scattering microscopy

Brillouin light scattering is a process, during which photons inelastically scatter on quasiparticles like magnons (spin waves) or phonons (lattice vibrations). Our interest is focused on the experimental technique built on this process, namely the Brillouin light scattering microscopy (sometimes spectroscopy) (BLS). This technique became a well-established tool for characterization of spin waves due to its ability to map the waves intensity with sub-micron resolution and simultaneously measure their frequency. Variations to this technique were developed, that can additionally measure phase of the waves or be directly wave-vector sensitive [40], [41].

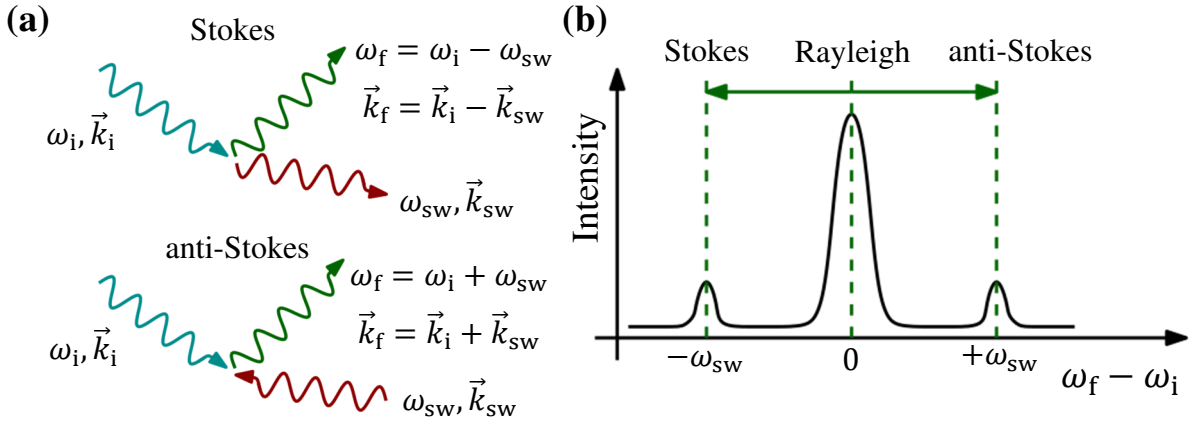

Fig.2.2: **(a)** Diagrams of the inelastic Brillouin light scattering. **(b)** Sketch of a BLS spectrum showing positions of the Stokes and anti-Stokes peaks relative to the elastically scattered Rayleigh peak. In real experiments there is a whole band of possible magnon frequencies, and we measure the anti-Stokes side of spectrum.

[1] This is the so-called positive process, in which the irradiated resist is removed during its development. The opposite would be the negative process, in which the non-irradiated regions are washed away during the development.

In the quantum-mechanical approach the Brillouin light scattering process can be described by photons scattering on magnons. During this scattering, the photons can either lose their energy and generate a magnon (Stokes process) or they can gain the magnon's energy and annihilate him (anti-Stokes process), which is schematically displayed in Fig.2.2 (a). According to the laws of conservation of energy and momentum the scattered photon's frequency (energy) ω_f and wave vector (momentum) k_f will be

$$\omega_\mathrm{f} = \omega_\mathrm{i} \pm \omega_\mathrm{sw}, \tag{2.1}$$

$$\vec{k}_\mathrm{f} = \vec{k}_\mathrm{i} \pm \vec{k}_\mathrm{sw}, \tag{2.2}$$

where ω_i and k_i are the incident photon's frequency and wave vector, ω_sw and k_sw correspond to the magnon and the minus (plus) signs are valid for the Stokes (anti-Stokes) process, during which the magnon is generated (annihilated). It should be noted that the intensity of the scattered light is proportional to the intensity of the measured spin wave [40].

The conservation law of momentum as presented above is valid only for scattering in infinite media. In real experiments the scattering process happens at the interface of the magnetic body and air, which breaks the translation symmetry in the normal direction and consequently only the in-plane component of momentum is conserved [42]. The in-plane wave vector component of the light involved in the scattering is then given by its wave vector size $2\pi/\lambda$ and the angle of incidence θ_i. Moreover, we can use this fact to compute the maximal detectable magnon wave vector, which corresponds to the situation, when the light incoming under the largest incidence angle $\theta_\mathrm{i}^\mathrm{max}$ scatters back in its original direction. In this case, the transferred momentum is equal to double the initial photon's momentum, or

$$k_\mathrm{sw}^\mathrm{max} = 2\frac{2\pi}{\lambda}\sin\theta_\mathrm{i}^\mathrm{max}. \tag{2.3}$$

In the used setup we employ a green laser ($\lambda = 532$ nm) and the numerical aperture of our objective (LD EC Epiplan-Neofluar 100x/0.75 BD) is $\sin\theta_\mathrm{i}^\mathrm{max} = 0.75$ leading to the maximal detectable wave vector $k_\mathrm{sw}^\mathrm{max} \cong 18\ \mathrm{rad/\mu m}$.

In Brillouin light scattering microscopy, which is designed for high spatial resolution, we illuminate the sample with a wide range of incidence angles resulting in the laser spot (limited by diffraction) having a diameter of approximately 250 nm [42]. This also means, that we detect a wide range of magnon wave vectors at the same time (with the limit described above). Not only will we measure different BLS frequency shifts depending on the sample's parameters, but the parallel detection of a whole range of wave vectors implies, that we detect many different modes, which, according to the spin-wave dispersion relation, have a certain range of frequencies.

To investigate the spectrum of scattered photons a tandem Fabry-Perot interferometer is employed. A Fabry-Perot interferometer (FPi) is made of two parallel mirrors with high reflectivity separated by a distance of L. In the experimental setup the scattered photons enter the interferometer through backside of one of the mirrors and we detect them behind the second mirror after they pass though the interferometer. Characteristic feature of the FPi is that the transmission has sharp peaks for wavelengths, that form a standing wave in the cavity between the mirrors, and has suppressed transmission elsewhere. The condition for existence of the standing wave is that the twice reflected light must interfere constructively with the incoming light, that is, the optical path of the twice reflected light must be equal to an integer multiple n of the wavelength λ_n

$$2L = n\lambda_n = n\frac{c}{f_n}. \tag{2.4}$$

Therefore, the frequency difference Δf between two neighboring transmission peaks, which is commonly called free spectral range (FSR), is

$$\Delta f = FSR = \frac{c}{2L}. \tag{2.5}$$

It is clear from this equation, how we can perform the spectral scan of photons on different frequencies – we can adjust the separation of mirrors L during the measurement, changing position of the transmission peak.

Unfortunately, width of the transmission peaks is, for a given setup, proportional to the FSR, meaning, that increasing the scanned frequency (by shortening the cavity) also increases the spectral width of transmission [41]. To improve the spectral resolution and range a system of two successive FPis is used, hence the name tandem Fabry-Perot interferometer. Transmission of the joint system is then a multiplication of the transmission functions of the individual FPis, which are all displayed in Fig.2.3 (b) and (c) for the cavity sizes $L_1 = 5.32$ mm and $L_2 = 5.05$ mm. Corresponding free spectral ranges of the individual interferometers are quite low $FSR_1 = 281$ MHz and $FSR_2 = 296$ MHz. The transmission peaks of the FPis are aligned at a certain frequency allowing photons at this frequency to pass through both interferometers. But the neighboring peaks do not coincide and the total transmission at their frequency is almost zero (amplitude of the small "ghost" peaks does not overreach 1% of the main peak [41]). After 20 FSRs of the first FPi and 19 FSRs of the second FPi the transmission maxima meet again and another transmission peak of the tandem FPi occurs. The free spectral range of such a tandem system is therefore much larger (5.63 GHz).

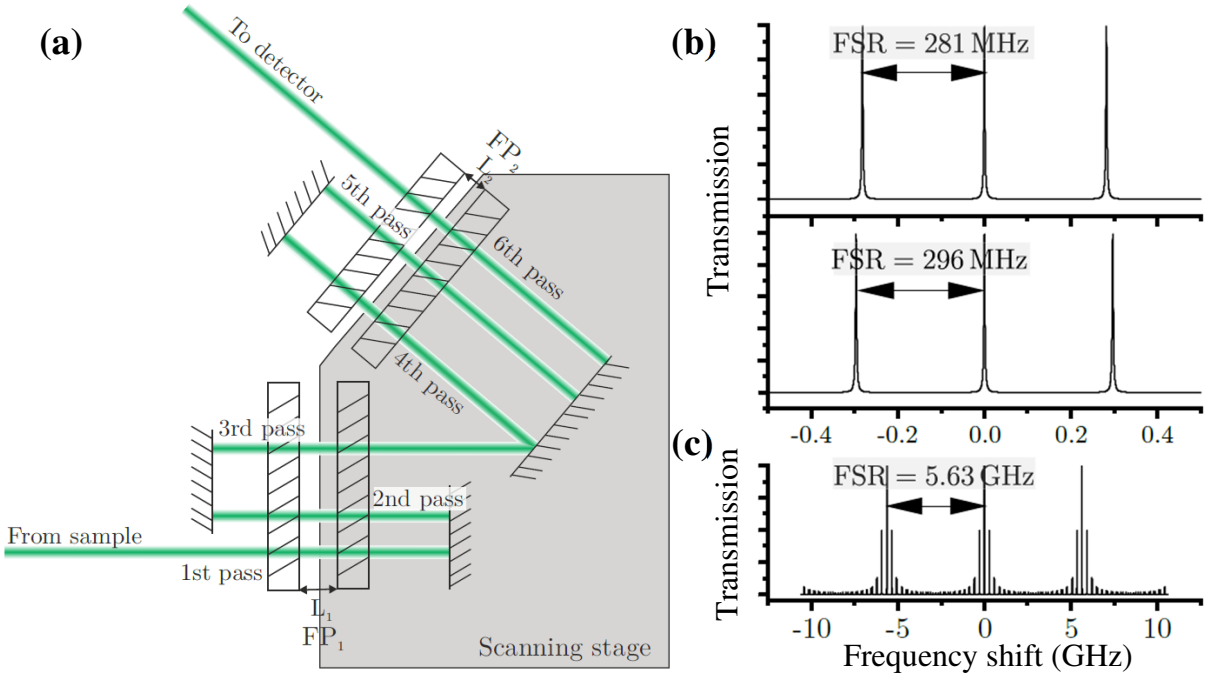

Fig.2.3: **(a)** Schematic of the six-pass tandem Fabry-Perot interferometer. **(b)** Transmission spectra of the two individual FPis with mirror separations $L_1 = 5.32$ mm and $L_2 = 5.05$ mm. **(c)** Transmission spectrum of the tandem interferometer composed of the FPis from (b). Vertical axis is „zoomed" to lower values to highlight side peaks, which reach 1% of the main peak at maximum. All taken from [41].

As was suggested above, the spectral scanning can be performed by changing the distances between mirrors. In the tandem FPi the situation is a little more complicated, because in order to keep the two main transmission peaks aligned while we shift them, we have to keep the ratio L_1/L_2 constant. This can be done by placing one side of each individual FPi on the same scanning stage, which moves along the optical path of one of the FPis, while the other FPi is tilted by a fixed angle. Contrast can be further improved by guiding the scattered photons through the FPis several times as is shown in a scheme of a tandem Fabry-Perot interferometer in Fig.2.3 (a).

2.3 Kerr microscopy

Under usual circumstances an electromagnetic wave reflected from an interface keeps its polarization and the portion of reflected light is dependent on the refractive indices of the bordering materials as is described by the well-known Fresnel formulas. However, upon reflection from magnetic materials light can slightly change its polarization state. This subtle effect is called the magneto-optical Kerr effect.

Light, that is initially linearly polarized, can [depending on the geometry, see Fig.2.4 (a)] become elliptically polarized, when reflected from a magnetized material. The new elliptical polarization state can be described by two parameters – Kerr rotation θ_K and Kerr ellipticity ϵ_K [defined in Fig.2.4 (b)]. In the longitudinal configuration, which we are using in our experiments, the magnitude of these parameters is proportional to the magnetization component in the plane of incidence [43].

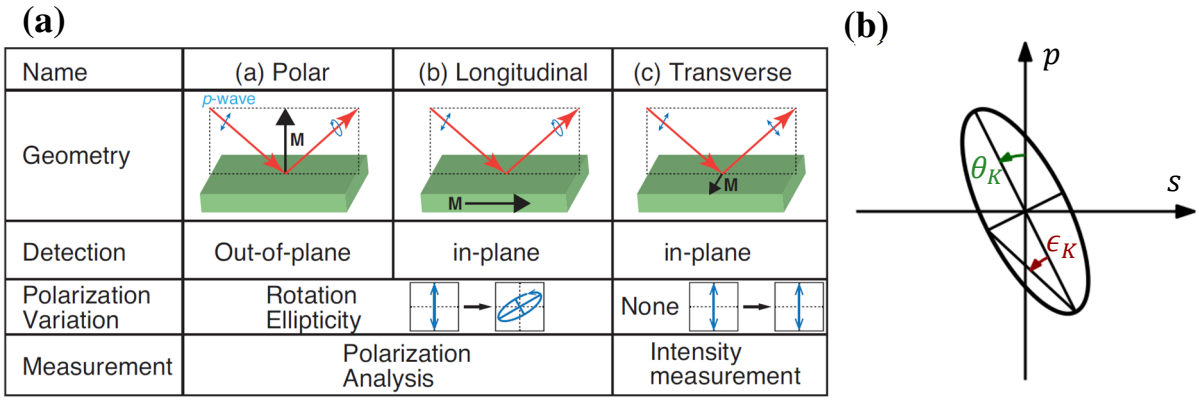

Fig.2.4: **(a)** Diagrams of the different measurement geometries, taken from [44]. Dashed rectangles express the plane of incidence. During the polar and longitudinal measurements, the Kerr effect changes linearly polarized light into elliptically polarized. In the transverse configuration only the intensity is modified. We employ the longitudinal configuration. **(b)** Elliptical polarization state described by the Kerr rotation θ_K and ellipticity ϵ_K, created from initial p-polarization. Typical values of these angles are units of milliradians.

In the Kerr microscope the incoming light is polarized by a first polarizer, reflected from the magnetic sample obtaining some Kerr rotation and then passes through an analyzer, which is rotated by $\pi/2 + \varepsilon_0$ to the polarizer, where ε_0 is small. Without any Kerr rotation the intensity behind the analyzer would follow the Malus's law $I = I_0 \sin^2 \varepsilon_0$. Including the Kerr rotation in the model changes the total angle to [42] $\varepsilon = \varepsilon_0 + \theta_K$. By Taylor's expansion of the sine squared [42], we can write the intensity as $I = I_0(\sin^2 \varepsilon_0 + \theta_K 2 \sin \varepsilon_0)$. This shows that the

signal detected on the camera is linearly dependent on the Kerr rotation and therefore linearly dependent on the magnetization component in the plane of incidence.

2.4 Micromagnetic simulations

Getting information about the behavior of magnetic systems through experiments is indispensable, but commonly quite lengthy, because usually one must first complete several fabrication steps and only then perform the measurement. Moreover, output of the measurement itself generally has certain limitations, for example when it comes to spatial or spectral resolution, and we detect only specific quantities (e.g. only signal proportional to the longitudinal component of magnetization in the longitudinal Kerr microscopy). Solving the Landau-Lifschitz-Gilbert equation (1.36) analytically offers advantages over the experimental outputs with its mentioned limitations, but in practice, due to its extreme complexity, this approach is possible only for some simple geometries and problems. This void was filled with numerical simulations, which offer insight into the magnetic system unachievable by experiments and are limited only by the available computational power.

There are two main numerical methods for solving micromagnetic problems [5] – 1) the finite element method, in which the simulated area is subdivided into (possibly) nonuniform, finite elements and functions are approximated by some simple nodal basis functions. Using the governing differential equation and boundary conditions, the problem leads to a system of linear equations for the coefficients of each nodal basis function, which together approximate the desired solution. 2) the finite difference method, which is based on discretization of functions over some uniform grid and replacing of derivatives by finite differences. The solution is found by numerically integrating the equation of motion by discrete time steps. A complete example of this approach is presented in [45], where the authors implement the method in fewer than 70 lines of NumPy/Python code. Advantage of the finite difference method is its uniform grid, which allows for straightforward computation of the discrete Fourier transformations without any interpolation.

Typically, the LLG equation includes the common effective field terms mentioned in section 1.2 along with some other effects such as the Dzyaloshinskii-Moriya interaction or the spin-transfer torques. Recently, effort has been focused not only on increasing the simulation speed but also on including a higher number of physical phenomena of the modelled systems [46].

We are using the open-source GPU-accelerated micromagnetic simulation program MuMax3 built on the finite difference method [47]. In the script defining each simulation we set the 3D rectangular grid, geometry of the magnet, region-specific material constants (such as the saturation magnetization or anisotropy magnitude and direction), time and space dependent external magnetic field, periodic boundary conditions (PBC) and more. The PBCs essentially create a chosen number of copies of the simulated area in the selected directions on each side. The periodicity implies that for example the exchange interaction, which normally involves only the nearest neighboring cells, connects the bordering cells on one side of the simulation to the corresponding cells on the opposite side. Less trivially, the demagnetizing field of all the copies is added to the simulated area. One consequence of this is the disappearance of the surface charges directly on sides of the simulated area, where the PBCs are used.

To obtain the temporal and spatial evolution of the simulated magnetic system the LLG equation (1.36) is numerically integrated over time using the following explicit Runge-Kutta

methods. When we want to run normal/real time evolution of the system, the Dormand-Prince method is used [47]. Equilibrium configuration can be found more quickly using a method, in which the precession term in the LLG equation is ignored and the damping term is amplified. In that case the integration over time is performed by the Bogacki-Shampine method [47]. After each time step we arrive at new magnetization configuration and the effective field $\vec{H}_{\mathrm{eff}}$ (1.22) is recalculated.

The magnetocrystalline anisotropy contribution to the effective field does not need to be approximated for the finite difference method, because it is a purely local property and is evaluated cell-wise. Effective field of the uniaxial anisotropy can be written using the normalized magnetization $\vec{m}$ and a unit vector $\vec{e}_{\mathrm{uni}}$ indicating the anisotropy direction as [47]

$$\vec{H}_{\mathrm{uni}} = \frac{2K_{\mathrm{u}}}{\mu_0 M_S}(\vec{e}_{\mathrm{uni}} \cdot \vec{m})\vec{e}_{\mathrm{uni}} + \frac{4K_{\mathrm{u2}}}{\mu_0 M_S}(\vec{e}_{\mathrm{uni}} \cdot \vec{m})^3 \vec{e}_{\mathrm{uni}}. \tag{2.6}$$

The situation is more difficult with the effective field of the short-range exchange interaction, in which the second derivatives are replaced by differences. The effective field due to the Heisenberg exchange interaction can be approximated from magnetization of its six nearest neighboring cells indexed by i and from the grid step in the appropriate direction Δ_i as [47]

$$\vec{H}_{\mathrm{ex}} = \frac{2A_{\mathrm{ex}}}{\mu_0 M_S}\vec{\nabla}^2\vec{m} \cong \frac{2A_{\mathrm{ex}}}{\mu_0 M_S}\sum_i \frac{\vec{m}_i - \vec{m}}{\Delta_i^2}. \tag{2.7}$$

This approximation holds well if the angle between magnetizations of neighboring cells is not too large. To secure this, a sufficiently small grid step size compared to the exchange length l_{ex} should be chosen [47]. This parameter (characteristic to the material, around 5 nm for Permalloy) is given by [42]

$$l_{\mathrm{ex}} = \sqrt{\frac{A_{\mathrm{ex}}}{\mu_0 M_S^2}}. \tag{2.8}$$

Implementation of the demagnetizing field in the finite difference method is from the relevant interactions the most complicated one, because it is a long-range interaction calculated as an integral over the whole magnetic body (1.11). Since in the simulation the magnetization and the demagnetizing field are constant in each cell, this integral can be rewritten using a sum over all cells to obtain the demagnetizing field (at any point in space, it is just an alternative expression of the same field) and calculating the average of this field over the cell with index i, where we want to know the discretized field $\vec{H}_{\mathrm{d}}^{\,i}$ [5]

$$\begin{aligned} &\vec{H}_{\mathrm{d}}(\vec{r}) = \int \hat{\Gamma}(\vec{r} - \vec{r}')\vec{M}(\vec{r}')\mathrm{d}^3\vec{r}' \rightarrow \\ &\rightarrow \vec{H}_{\mathrm{d}}^{\,i} = \frac{1}{\Delta_x\Delta_y\Delta_z}\int_{\Omega_i}\left[M_S\sum_j\left(\int_{\Omega_j}\hat{\Gamma}(\vec{r} - \vec{r}')\mathrm{d}^3\vec{r}'\right)\vec{m}_j\right]\mathrm{d}^3\vec{r}, \end{aligned} \tag{2.9}$$

where $\vec{m}_j$ is the magnetization of the cell indexed by j, which acts as source of the demagnetizing field, and cuboid $\Omega_j \subset \mathbb{R}^3$ is its space. Ω_i is space of the cell, for which we are calculating the field.

We can exploit regularity of the grid and transform the integral to integrate over some reference cell instead of the various cells i and j in (2.9). This can be done by writing the spatial

variables $\vec{r} \in \Omega_{\vec{\imath}}$ using the multiindices of the given cell $\vec{\imath} = (i_x, i_y, i_z)$ and the equivalent position $\vec{r}_{\mathrm{ref}} \in \Omega_{\mathrm{ref}}$ in the reference cell, which can be for simplicity indexed by $(0, 0, 0)$. Then

$$\vec{r} = \vec{r}_{\mathrm{ref}} + \sum_k i_k \, \vec{\Delta}_k, \tag{2.10}$$

where $k = x, y, z$ and $\vec{\Delta}_k = \Delta_k \vec{e}_k$, with $\vec{e}_k$ being the unit vector of axis k. The cell integration region can be generally transformed this way as

$$\int_{\Omega_{\vec{\imath}}} f(\vec{r}) \mathrm{d}^3\vec{r} = \int_{\Omega_{\mathrm{ref}}} f\left(\vec{r} + \sum_k i_k \, \vec{\Delta}_k\right) \mathrm{d}^3\vec{r}. \tag{2.11}$$

Performing this for both integrals in (2.9) results in the demagnetizing field of the cell $\vec{\imath}$ being

$$\vec{H}_{\mathrm{d}}^{\vec{\imath}} = \frac{M_S}{\Delta_x \Delta_y \Delta_z} \sum_{\vec{\jmath}} \left[\int_{\Omega_{\mathrm{ref}}} \int_{\Omega_{\mathrm{ref}}} \hat{\Gamma}\left(\sum_k (i_k - j_k) \vec{\Delta}_k + \vec{r} - \vec{r}' \right) \mathrm{d}^3\vec{r}' \, \mathrm{d}^3\vec{r} \right] \vec{m}_{\vec{\jmath}}. \tag{2.12}$$

Important feature of this formula is that it takes the form of discrete convolution due to the first terms in the sum depending only on the difference $\vec{\imath} - \vec{\jmath}$ and the second terms on $\vec{\jmath}$

$$\vec{H}_{\mathrm{d}}^{\vec{\imath}} = M_S \sum_{\vec{\jmath}} \hat{\Gamma}_{\vec{\imath} - \vec{\jmath}} \, \vec{m}_{\vec{\jmath}}. \tag{2.13}$$

In this equation the tensor for $\vec{\imath} - \vec{\jmath}$ is calculated as

$$\hat{\Gamma}_{\vec{\imath} - \vec{\jmath}} = \frac{1}{\Delta_x \Delta_y \Delta_z} \int_{\Omega_{\mathrm{ref}}} \int_{\Omega_{\mathrm{ref}}} \hat{\Gamma}\left(\sum_k (i_k - j_k) \vec{\Delta}_k + \vec{r} - \vec{r}' \right) \mathrm{d}^3\vec{r}' \, \mathrm{d}^3\vec{r}. \tag{2.14}$$

According to the convolution theorem, the discrete convolution in (2.13) can be more easily calculated in the Fourier space, where it reduces to multiplication of the discrete Fourier transformations (FT) of its two inputs [5]

$$\mathrm{FT}\left(\sum_{\vec{\jmath}} \hat{\Gamma}_{\vec{\imath} - \vec{\jmath}} \, \vec{m}_{\vec{\jmath}} \right) = \mathrm{FT}\left(\hat{\Gamma} * \vec{m} \right) = \mathrm{FT}\left(\hat{\Gamma} \right) \mathrm{FT}(\vec{m}). \tag{2.15}$$

It should be noted that the size of the two matrices $\hat{\Gamma}$ and $\vec{m}$ is not the same, because one is indexed only by $\vec{\jmath}$ while the other is indexed by all the possible combinations of $\vec{\imath} - \vec{\jmath}$. This issue can be solved by zero-padding of the magnetization matrix $\vec{m}$ to match the size for multiplication in (2.15) and afterward taking only the appropriate submatrix of the size of $\vec{m}$ (same as $\vec{H}_{\mathrm{d}}$) as the result [5].

Great advantage of using the convolutional / discrete Fourier transform approach is its speed. The fast Fourier transform algorithm of the discrete FT is, as the name suggests, very fast – its computing complexity scales with the number of cells n as $O[n \cdot \log(n)]$ instead of the $O(n^2)$ for the direct application of discrete FT's definition. Moreover, the FT of the discrete demagnetizing tensor $\hat{\Gamma}$ (2.14) needs to be computed (which can be done analytically [5]) only once, because it depends only on the grid parameters (or it can even be loaded from some previous simulation with the same grid). The demagnetizing field $\vec{H}_{\mathrm{d}}$ can be calculated in each time step by computing $\mathrm{FT}(\vec{m})$, multiplying it cell-wise in the Fourier domain with the already known $\mathrm{FT}\left(\hat{\Gamma}\right)$ and inverse Fourier transforming the product.

3 Metastable iron-nickel system

Magnetic micro- and nanostructures are traditionally prepared by some combination of optical or electron beam lithography and lift-off (section 2.1), etching [48], focused electron beam induced deposition [30] or ion implantation [32]. The fabrication technique presented in this chapter is based on transformation of metastable paramagnetic iron-nickel crystal lattice into stable ferromagnetic phase by focused ion beam (FIB). This fabrication process provides two advantages over the conventional techniques. Firstly, it is a single-step process. And secondly, it offers a high degree of local controllability – only the area scanned by FIB gets transformed, and on top of that, direction of the FIB scanning determines the axis of magnetic anisotropy.

In this chapter, we will describe this fabrication technique, which involves growth of the metastable paramagnetic iron-nickel film and transformation into stable ferromagnetic phase by FIB-scanning. Then, magnetic properties of transformed structures will be investigated.

3.1 Magnetic structures in metastable films

At room temperature, iron (Fe) forms the body centered cubic lattice (bcc) in the bulk and is ferromagnetic in this phase. Above 900 °C the crystallographic structure of iron in bulk is face centered cubic (fcc) and the material is paramagnetic. It was found that the latter high-temperature phase can be stabilized even at the room temperature in thin iron films by epitaxial growth on an fcc copper substrate with small lattice mismatch to the fcc iron [49]. Indeed, the bcc Fe lattice constant is 2.680 Å, while the fcc Fe lattice constant is 3.588 Å, and the Cu substrate in the fcc phase has the lattice constant 3.615 Å.

Phase of the deposited layer of iron strongly depends on the layer's thickness – crystalline structure of the iron films of thickness under 4 monolayers is governed by interfacial effects and the phase is magnetic bcc. Films of thickness between 4 and 10 monolayers exist in the metastable fcc structure, and thicker Fe films spontaneously enter the stable bcc phase [50]. The maximum thickness of 10 monolayers is limiting and stabilization of thicker fcc iron layers was desired. Fortunately, there are two approaches enabling us to increase the maximal thickness. First, the iron layer can be grown with a presence of carbon monoxide in the vacuum chamber, which allows stabilization of up to 22 monolayer thick fcc iron [51]. And second, intermixing nickel, which occurs in the fcc structure at room temperature, with the iron allows stabilization of metastable fcc layers without any thickness limitation [52]. Phase diagram of the stabilized thin film's phase in dependence on the carbon monoxide pressure and nickel concentration is presented in Fig.3.1. Metastable iron-nickel films with nickel concentration 22% were more closely investigated in [53], where (as a side topic) growth on different substrates was tried and further investigation of the influence of carbon monoxide pressure during deposition was performed. Metastable iron-nickel film on a Cu substrate used in this thesis (internal name Cu15) was prepared by Jonáš Gloss.

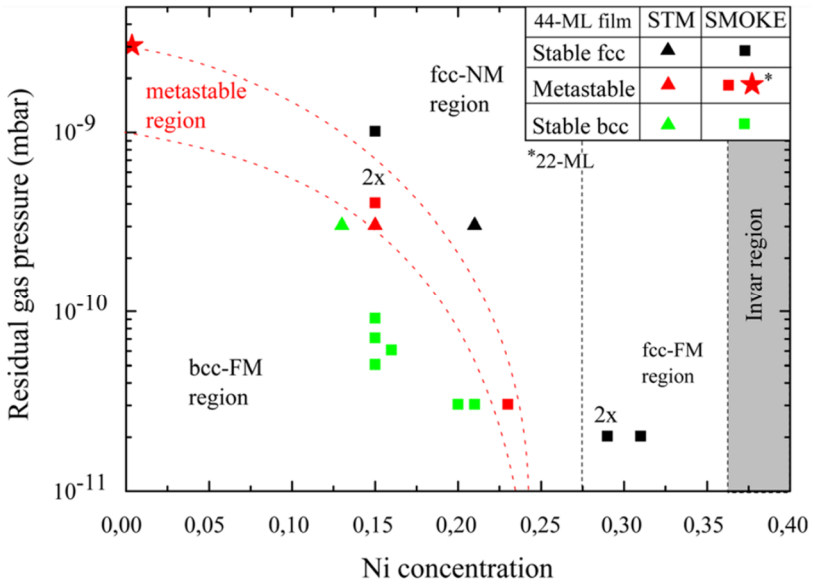

Fig.3.1: Structural and magnetic phase diagram of the stabilized thin layer in dependence on the carbon monoxide pressure and nickel concentration in the iron-nickel alloy. Structural properties were investigated by scanning tunneling microscopy and magnetic properties by surface magneto-optical Kerr effect. We are interested in the (red) metastable region. Taken from [52]. Further investigations of films with 22% nickel concentration reveal that the metastable phase can be stabilized in a wider range of carbon monoxide backpressures than it appears from this plot [53].

Metastability of the fcc iron-nickel structure means, that this phase constitutes only a "local" minimum of energy, while the stable bcc phase corresponds to the "global" minimum of energy. Transformation from the metastable to the stable phase was achieved in the various films using irradiation by argon ions [49], [51], [52]. The transformed films in these studies were measured by scanning-tunneling microscopy, low-energy electron diffraction and magneto-optical Kerr microscopy and it was confirmed that they have changed their crystalline structure from fcc to bcc and became ferromagnetic.

It is argued [42] that the incident ions transfer their energy and momentum to atoms of the film upon impact, which leads to local melting of the metastable crystal if the ion dose in the given spot is high enough. Then the material recrystallizes with some probability into the stable ferromagnetic bcc structure. Transforming the film in spots adjacent to already recrystallized bcc areas is easier than creation of new bcc nuclei and consequently the typical pattern of transformation is nucleation at several locations and (needle-like [52]) spread of the bcc crystal from them [42].

Transformation in the previously mentioned articles [49], [51], [52] was performed using broad low-energy argon-ion beam irradiation. However, in this thesis we are using the focused ion beam of gallium ions to transform the metastable layers, which gives us spatial control over the process. This approach was investigated by Urbánek et. al. [54]. The authors have demonstrated that the transformation can be performed by either scanning the metastable layer with the full appropriate ion dose in one scan or by performing multiple (100) scans of similar total dose, as is presented in Fig.3.2 (a) and (b). The FIB parameters were essentially the same as the parameters used for this Thesis – acceleration voltage 30 kV, current approx. 150 pA, beam spot size 30 nm, scanning step 10 nm (to secure overlapping of neighboring spots) and the dwell time is adjusted to control the dose [42], [53], [54]. The fabrication was done on a system combining scanning electron microscope (SEM) and FIB (Tescan Lyra3).

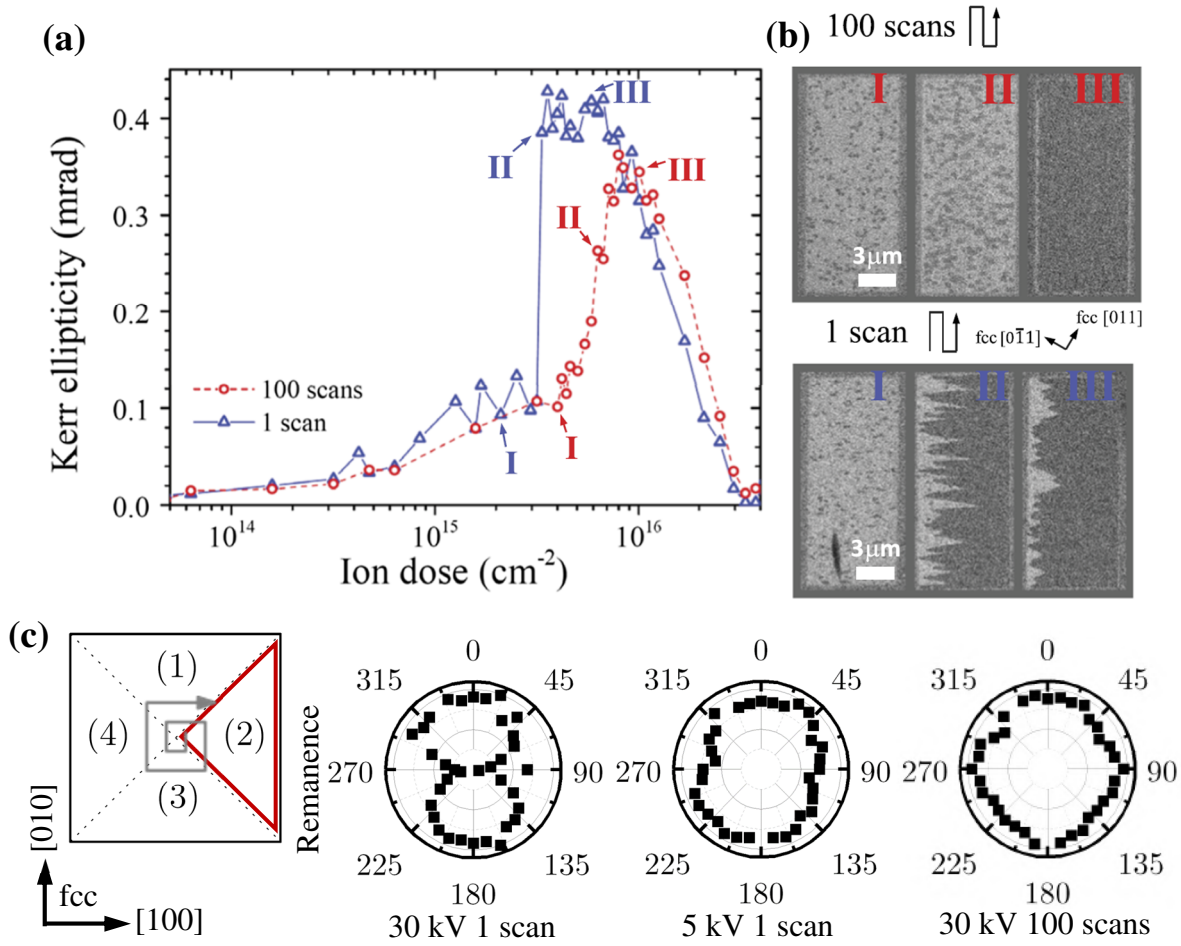

Fig.3.2: **(a)** Results of experiment studying the appropriate ion dose for transformation – the Kerr ellipticity, which is proportional to magnetization, in dependence on the ion dose, which was used in attempt to transform a rectangle. Few examples of these (semi-) transformed rectangles are shown in (b). Adapted from [54]. **(b)** SEM images of some (semi-) transformed rectangles. Contrast between the different domains (medium gray – untransformed fcc, light gray – bombarded but untransformed, dark gray – fully transformed bcc) is caused by the channeling effect [55]. Adapted from [54]. **(c)** Kerr measurements in region (2) of squares transformed by FIB scanning from the middle in square-like spiral along [100] and [010] directions of fcc. This scanning strategy results in creation of 4 crystal domains (as in Fig.3.3 top row). Hysteresis loops were taken for fields applied under different angles (measured from the [010] direction). Normalized remanent magnetization as function of this angle is plotted for different acceleration voltages and number of scans used during the fabrication. Only the structure transformed by one 30 kV scan shows clear anisotropic behavior. Adapted from [53].

It is clear from Fig.3.2 (a) that the single scan offers two advantages – first, we need lower total dose, which also means shorter total time of the process, and second, the lower dose leads to larger magnetization, because the film was less bombarded and is less intermixed and less sputtered away. It was also reported [54] that film transformed by a single scan exhibits clear magnetic uniaxial anisotropy, while the film transformed by 100 scans does not. This finding was replicated in [53], where the author also tested different acceleration voltage (5 kV) with the result showing good anisotropic behavior only for rectangles transformed by a single 30 kV scan, while the 5 kV single scan created structure with only very weak sign of anisotropy and 100 scans resulted in no anisotropy, as is presented in Fig.3.2 (c).

Weakness or nonexistence of magnetic anisotropy is in these cases caused by inhomogeneity of the crystal domains [53]. When we FIB-scan a square area with a square-like spiral from the center outwards, we transform the metastable film into 4 or 8 crystal domains depending on whether the scanning lines are parallel to [100] and [010] or [110] and [$\bar{1}$10], as is displayed in Fig.3.3. These scanning strategies present a reliable way to prepare roughly homogeneous and predictable domains. However, judging by the SEM contrast, the transformed squares tilted by 45° (bottom row) seem to be more homogeneous, which agrees well with previous crystallographic experiments [53]. Fig.3.3 also shows the influence of ion dose in a close range (each column corresponds to a different dose). Lower doses don't transform the metastable film properly and the result is not homogeneous, while too high doses lower the magnetic qualities [which can be seen in Fig.3.2 (a)]. A dose test is typically done before fabrication of desired structures. For example, in the fabrication process, which involved the sample in Fig.3.3, we have chosen the 4th dose (column) for further experiments.

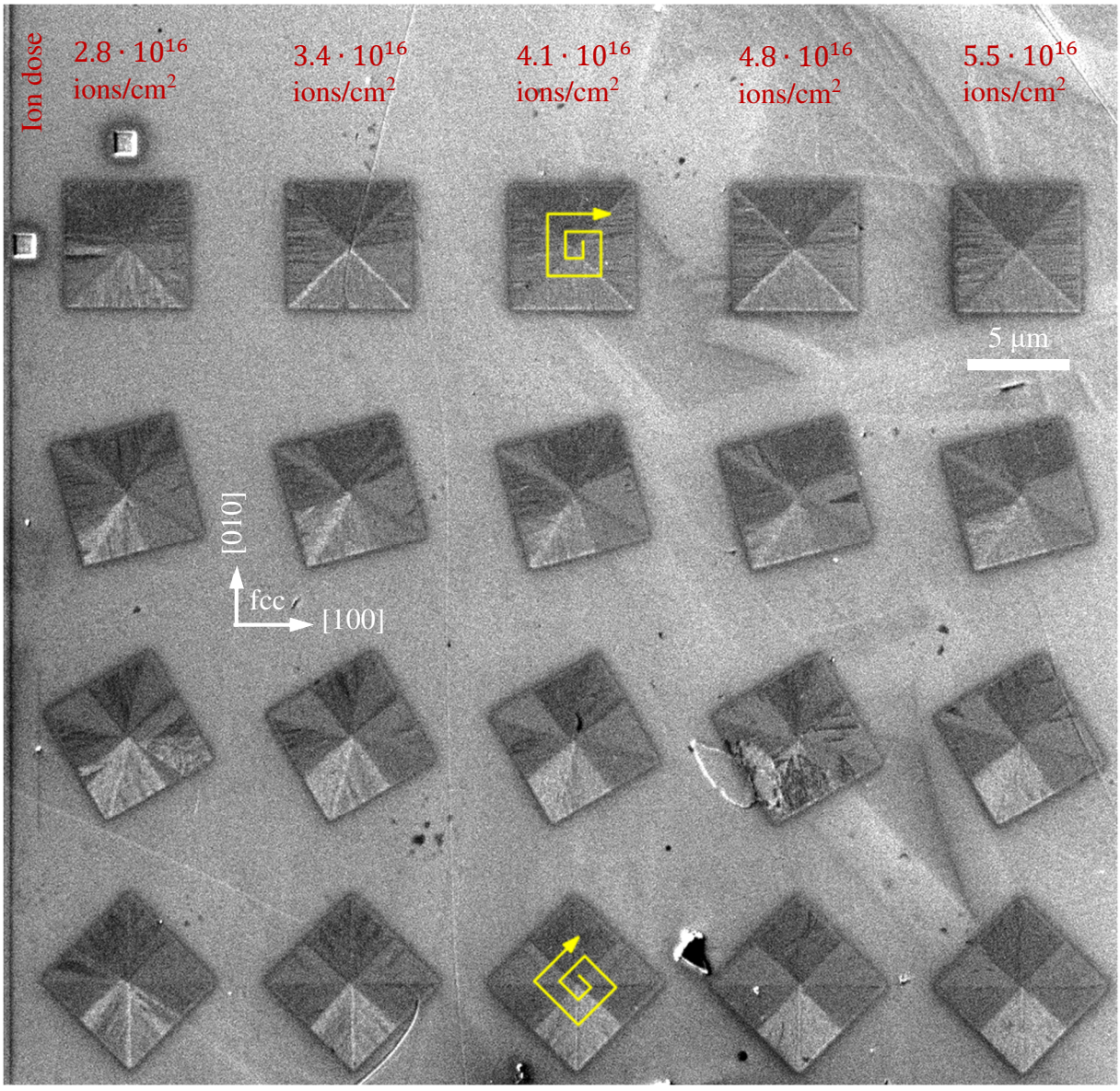

Fig.3.3: SEM image of a tilted (4°) sample with transformed squares. The squares were transformed by scanning the FIB in square-like spiral inside-out, as is sketched by the yellow traces. Each column corresponds to a different dose, which rises from left to right. Each row corresponds to a different angle of scanning.

Finding the crystallographic directions of metastable fcc lattice is performed by visualizing the pseudo-Kikuchi lines and aligning it with the axes of the SEM-FIB device [53].

Crystallographic experiments (electron backscatter diffraction) have revealed orientation of the transformed bcc lattice in the different domains [53]. It was shown, that in the more homogeneous case of 8-domain squares the bcc lattice tilts two of its faces out-of-plane, one face by approx. 5°and the second by approx. 2°. These two tilts produce the 8 unique domains, which are then distinguishable in the SEM (when the sample is tilted) due to the channeling effect [55]. The SEM and crystallographic measurements of the same structure are displayed in Fig.3.4 (a) and (b).

Furthermore, Holobrádek [53] has carried out magneto-optical Kerr measurements to investigate magnetic anisotropy in the different domains. Remanence magnetization exhibited the typical uniaxial character [as can be seen for one domain in Fig.3.4 (c)] and was parallel in each two opposite domains, which leads to 4 unique directions of the uniaxial anisotropy. Comparison of the magnetic and crystallographic measurements lead to the observation, that the easy axis is in the 8-domain square always approximately parallel to the axis, around which the bigger out-of-plane tilt of the bcc lattice can be defined [53]. It is worth pointing out, that the bcc lattice is cubic and one would therefore expect the cubic and not the uniaxial anisotropy to be present. The hypothesis, which still needs further testing and deeper explanation, is that we are dealing with magnetoelastic anisotropy, which is caused by mechanical stress [53], [54].

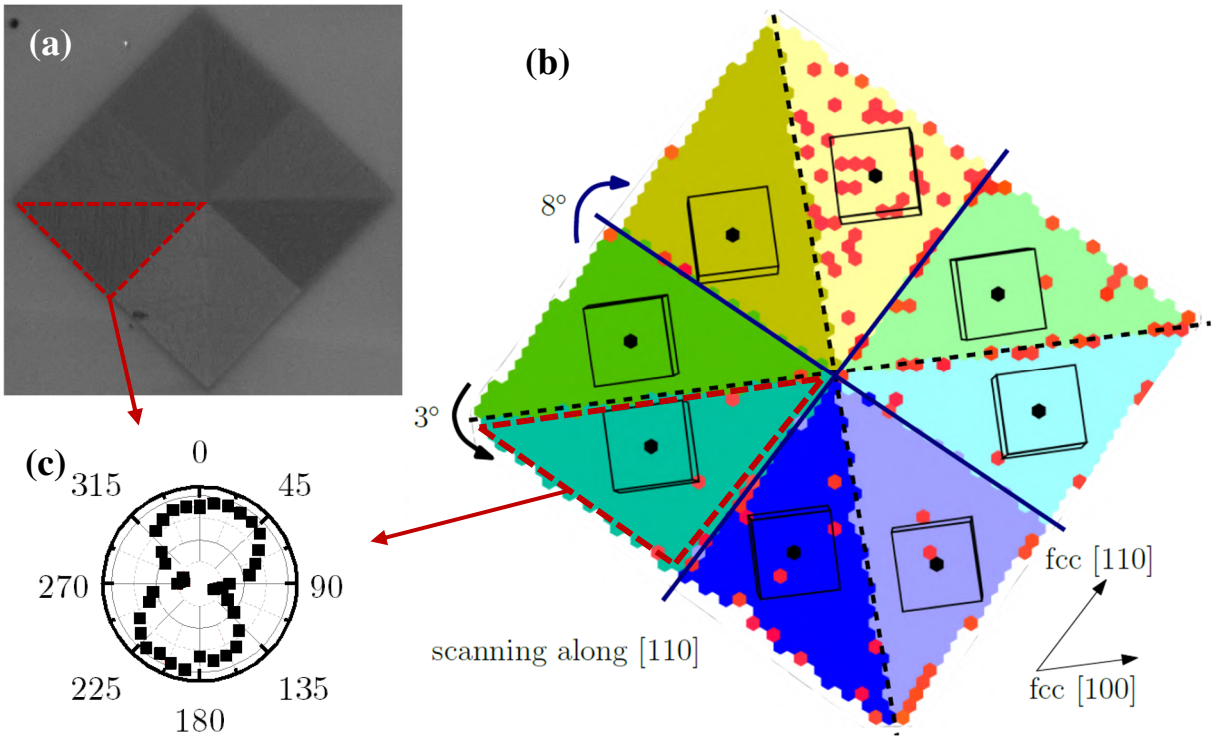

Fig.3.4: **(a)** Tilted (5°) SEM image of a transformed square with 8 domains. **(b)** Result of a crystallographic experiment (electron backscatter diffraction) showing orientation of bcc lattice in the different domains of the structure from (a). In each region the color unifies all pixels with misorientation up to 1.5° from the domains mean orientation of the lattice, which is sketched in each region. There are two types of axes (dashed black and solid navy), rotation around which by the appropriate angle can transform neighboring lattices. **(c)** Polar plot of magnetization remanence in the highlighted domain measured by Kerr microscopy in an equivalent but enlarged structure. All taken from [53].

3.2 Prepared magnetic structures

We needed to prepare structures suitable for propagation and refraction of spin waves. The 8-domain squares (introduced in the previous section) proved themselves to be reliable and homogeneous, but it is an unnecessarily large and complicated structure. Therefore, we have investigated the possibility of creation of the individual domains. It was found that they can be homogeneously and predictably transformed if we simply scan the individual triangular area the same way as the corresponding domain in the complete 45° tilted square, as is shown in Fig.3.5.

It is apparent from our experiments that the type of transformed domain is not determined only by the direction of FIB-scanning with respect to the crystallographic axes, but also by the way, in which the scanning is initiated. This can be seen in Fig.3.5 (a) where we compare the individual triangular domains, which were scanned from the apex of the triangular region (4 left structures, green arrows), with domains, which were scanned from the side (4 right structures, red arrows). The apex-initiated triangles correspond to the domains of the 45° tilted square as was intended, while the side-initiated triangles are more random and inhomogeneous. It is also worth pointing out, that the neighboring regions denominated as (1) and (2) in Fig.3.5 (a) (and other same-side pairs) were scanned in the same direction but exhibit different crystal orientations and anisotropy directions. The same remains true in single domains. This again highlights the importance of the scanning initiation.

3.2.1 Magneto-optical measurements of anisotropy

We have also performed magneto-optical Kerr microscopy measurements (which are described in section 2.3) to study the magnetic anisotropy of this structure. The sample was rotated with regards to the external field at several steps and hysteresis loops were measured each time. By saving the image from the Kerr microscope, we could reconstruct the hysteresis loop at every pixel and for every angle of field. Looking at the (normalized) remanence magnetization enables us to inspect the anisotropy. At zero external field the magnetization will align along the easy axis. Consequently, the remanent magnetization component in the initial direction of the field can be modeled by $|\cos(\theta - \theta_u)|$, where θ_u is the angle of uniaxial anisotropy axis from some axis and θ is the angle between the external field of the given hysteresis measurement and the same reference axis. In our case, we measure the angles from the [010] direction of the fcc lattice.

The anisotropy axis direction map in Fig.3.5 (b) nicely correlates with the crystal domains visible in the tilted SEM image and it agrees with the previously mentioned observation about the direction of the crystal's out-of-plane tilt and anisotropy. Remanence averaged over the individual domains of the square [Fig.3.5 (c)] confirms the earlier cited conclusion that there are four unique directions of anisotropy, because the opposite domains have the same direction. Angles between the anisotropies of neighboring domains are approximately 10 and 80 degrees, with the larger difference belonging to neighbors scanned in the same direction.

Regarding the design of structures for refraction of spin waves, different angle of interface between domains can be prepared by using the appropriate single domains and stopping the FIB-scanning at the desired angle. Also, there are needle-like regions of darker complexion visible in Fig.3.5 (a) [and some traces of them are visible in (b)], which have different (worse) magnetic properties and will be discussed below in another structure.

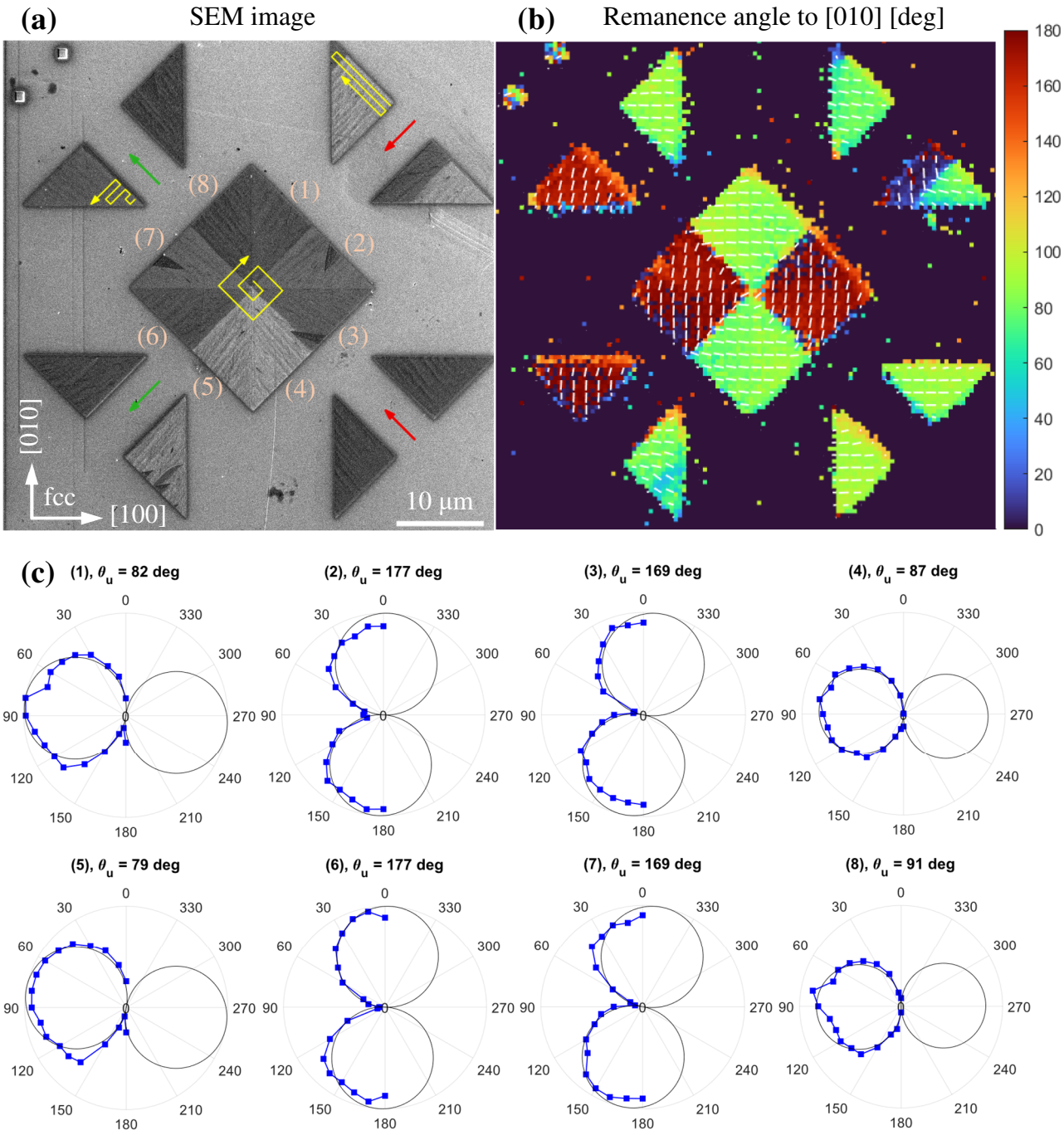

Fig.3.5: **(a)** SEM image of a tilted (4°) sample with the transformed square and individual domains. Yellow traces outline the scanning strategies and green arrows belong to the individual domains transformed from the apexes, while the red arrows to domains transformed from the sides. **(b)** Angle θ_u of the remanent magnetization from the [010] direction, which (away from edges) corresponds to direction of the easy axis of uniaxial anisotropy. This information was obtained from fits of the angular dependence of remanent magnetization with the model $|\cos(\theta - \theta_u)|$ in each (4-binned) pixel. White lines display the same information – local direction of the easy axis. **(c)** Normalized remanent magnetization in the 8 domains of the square fitted with the same model.

Example of a structure prepared for refraction of spin waves is presented below in Fig.3.6. We have chosen the domains labeled as (5) and (6) in Fig.3.5, which naturally occur as neighbors. Therefore, we could fabricate the structure using just one scanning path – from the top right corner along the $[\bar{1}10]$ direction, and the interface was guaranteed to be nice. (Regarding the other option, bordering domains prepared in two runs could have gaps of non-transformed material or small areas at the interface scanned twice due to precision limitations of the device.)

The transformation begins from the corner as intended – there are two domains and an interface along [110] between them. But at certain locations, perhaps on some defects, additional type of domain starts appearing and spreads further in widening needle-like areas. We tentatively call these domains alps. We have encountered these domains in all structures on this sample (Cu15) and they limit our ability to prepare large areas of uniform domains. Some defects, such as the line visible in Fig.3.6 (a), can initiate the conventional domains too.

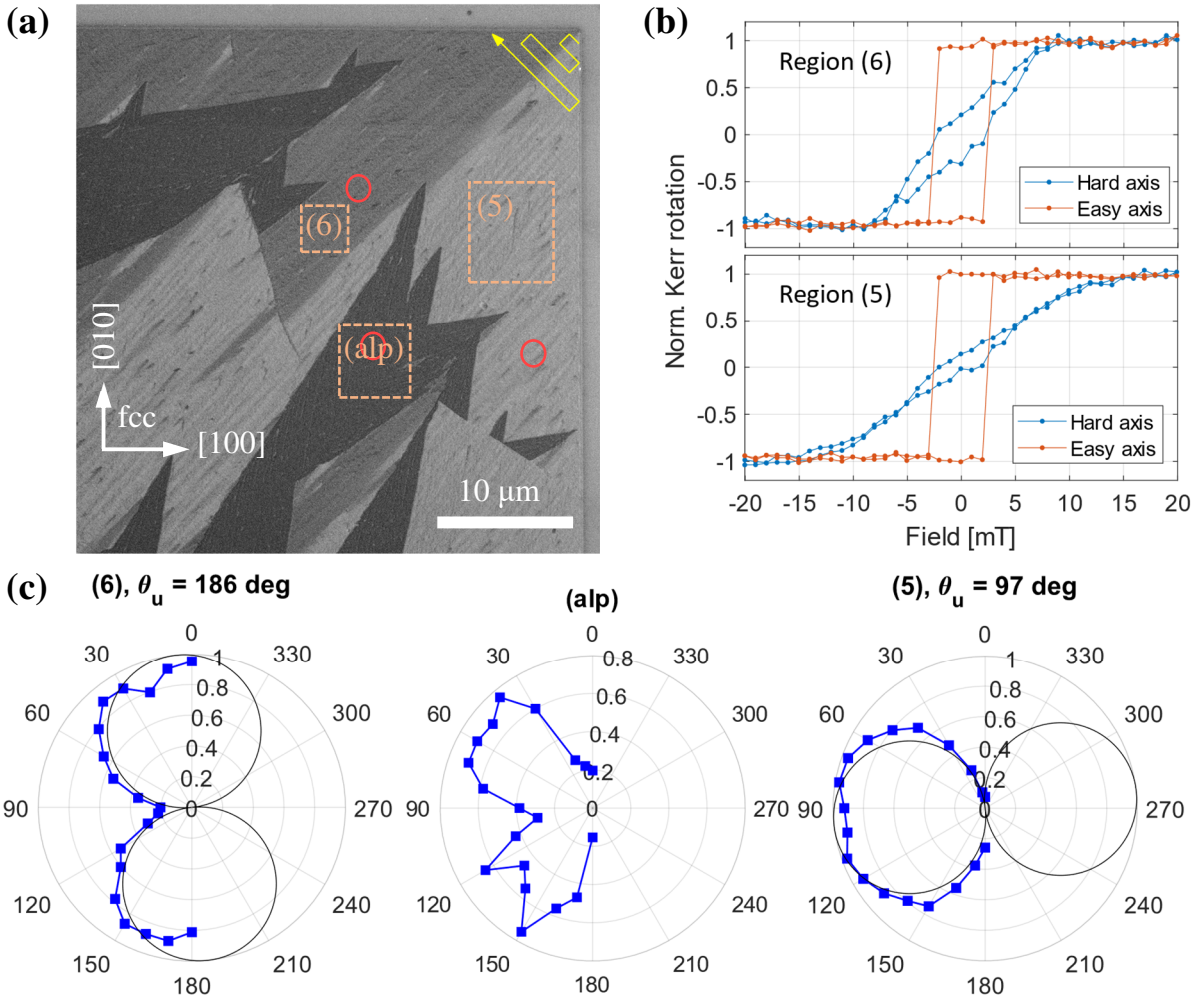

Fig.3.6: **(a)** Tilted (4°) SEM image of two bordering domains intended for refraction of spin waves. The transformation was initiated from the top right corner along the $[\bar{1}10]$ direction of fcc. Along the desired (6) and (5) domains another domain type was transformed – the alps. Red circles show positions of the laser spot in BLS measurements. **(b)** Hysteresis loops measured by Kerr microscopy in regions (6) and (5) outlined in (a) for their respective easy and hard axes. **(c)** Polar plots of (normalized) magnetization remanence in the three regions from (a). The intentionally created domains exhibit uniaxial anisotropy, while remanence in the alp resembles cubic anisotropy.

This structure was also investigated in the Kerr microscope. We have again measured hysteresis loops for a whole set of angles between the external field and [010]. In Fig.3.6 (b) we present loops of the two conventional domains (5) and (6) [retrieved from the highlighted regions in (a)] for the easy and hard axes. It appears that strength of the anisotropy is not same everywhere – in domain (6) the anisotropy field (1.26) is approximately 9 mT, while in (5) it is rather around 12 mT. Analyzing the Kerr microscopy measurement in different regions inside the two domains (not shown) also results in slightly different anisotropy fields, usually around 10 mT. A proper discussion of these results is performed below together with the results of BLS measurements.

By fitting the magnetization remanence as function of the external field angle (as above), we have obtained directions of the uniaxial anisotropy in (5) and (6) of this structure as shown in Fig.3.6 (c). It is apparent that the angles are not the same as in Fig.3.5, which shows anisotropy directions, which are flipped along the [010] axis (or rotated around the [100] axis by 180°) with respect to Fig.3.6.

Dependence of the magnetization remanence in the (alp) domains resembles cubic anisotropy, which would have two easy axes in the film's plane. Easy axes of pure iron are directed along ⟨100⟩ of its bcc lattice [7]. Remanence was measured high in the directions ⟨110⟩ of fcc [as can be seen in Fig.3.6 (c)], which suggests that the direction [110] of bcc crystal in (alp) could be parallel to [010] of fcc. It should be noted that behavior of magnetization in this domain type is very "unclean" and the pattern observed in Fig.3.6 (c) is less clear if analyzed over smaller areas. Other hypothesis is that the (alp) domain type has two possible uniaxial anisotropy directions, and the observed pattern is a mix of them. Ratio of the magnetic signal at saturation in region (6) to region (5) is around 0.9 and in (alp) to (5) ca. 0.5.

3.2.2 Brillouin light scattering – thermal spectra

We have also performed a measurement in the Brillouin light scattering microscope to obtain further information about these three domains. The laser spot was focused consecutively in locations outlined by the red circles in Fig.3.6 (a). Spectra of thermal magnons were acquired for several values of external field, which was applied in the [010] direction of fcc.

An example of these spectra is presented in Fig.3.7 (a) in the three domains at external field 60 mT. We can see that the magnon spectra are located at different frequencies and have different widths. This is caused by different magnetic properties and different orientation of local anisotropy to the (saturated) magnetization. To obtain these properties – saturation magnetization M_S and anisotropy constant K_u, we have fitted the frequency of ferromagnetic resonance (FMR, spin wave of $k = 0$) as function of the external field. The field is parallel to the easy axis of uniaxial anisotropy in the domain (6) and the FMR frequency can be modeled by (1.68) with $\varphi_K = 0,\ k = 0$ and $P = 0$ as

$$f_\parallel = \frac{\gamma}{2\pi}\sqrt{\left(B_\mathrm{ext} + \frac{2K_\mathrm{u}}{M_S}\right)\left(B_\mathrm{ext} + \frac{2K_\mathrm{u}}{M_S} + \mu_0 M_S\right)}. \tag{3.1}$$

In domain (5) the magnetization is saturated perpendicularly to the easy axis ($\varphi_K = \pi/2$) and the FMR frequency is given by

$$f_\perp = \frac{\gamma}{2\pi}\sqrt{\left(B_\mathrm{ext} - \frac{2K_\mathrm{u}}{M_S}\right)(B_\mathrm{ext} + \mu_0 M_S)}. \tag{3.2}$$

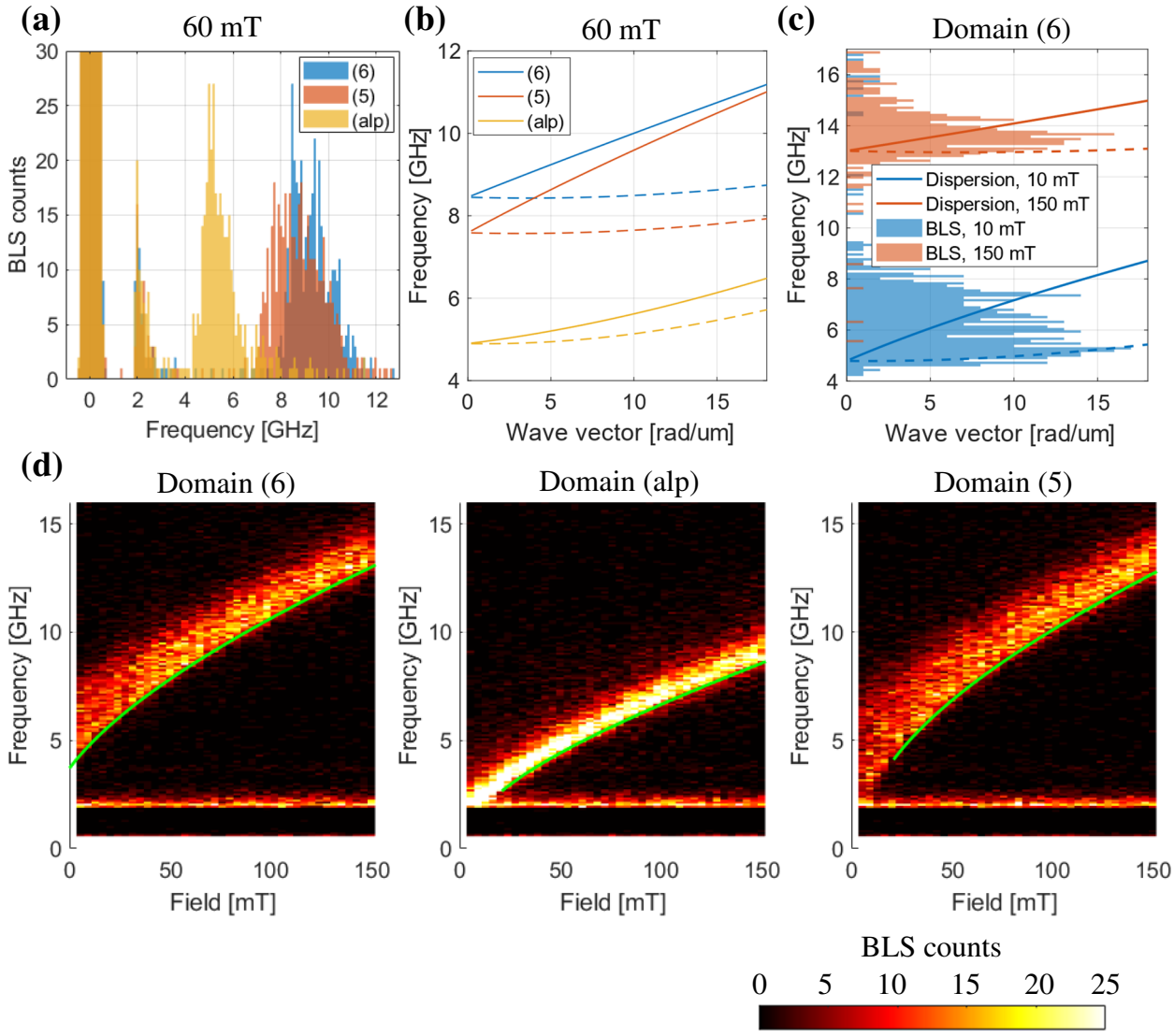

Fig.3.7: **(a)** BLS spectra measured at 60 mT with the laser spot consecutively focused on the domains (6), (alp) and (5) – approximate positions of the 250 nm-wide laser spot are outlined by red circles in Fig.3.6 (a). At 0 GHz we can see in all measurements the reference peak, which is used for stabilization of the tandem Fabry-Perot interferometer (see section 2.2). An undesired laser mode, located around 2 GHz, is also visible in all measurements. The proper magnon spectra are present between 4 GHz and 12 GHz. **(b)** Dispersion relations computed from (1.68) [in (alp) modified along (3.3)] using the found magnetic properties $(M_S, K_{u/1}, d)$ of the three domains (and properties $\gamma = 2\pi \cdot 29.3$ rad/Ts, $A_{ex} = 11$ pJ/m) at 60 mT. The borderline cases of Damon-Eshbach (DE, solid) and backward volume (BV, dashed) spin waves are plotted, spin waves with wave vector in other directions have intermediate frequencies. Graphs (a) and (b) correspond to each other. **(c)** Dispersions of DE and BV waves for the domain (6) plotted at two external fields show the reason for narrowing of the magnon spectrum with increasing field. Thickness of the layer d, which affects steepness of the dispersions, was estimated from comparisson of widths of the spectra and frequency span of dispersions computed from (1.68) using parameters from the FMR fit. **(d)** BLS spectra measured in the three domains for all external fields shown together with the fits of FMR frequencies [green lines, models (3.1) – (3.3)].

And regarding the (alp) domain, FMR frequency in thin film with cubic anisotropy magnetized along [110] is [56]

$$f_{C\langle 110\rangle} = \frac{\gamma}{2\pi}\sqrt{\left(B_{\mathrm{ext}} - \frac{2K_1}{M_S}\right)\left(B_{\mathrm{ext}} + \frac{K_1}{M_S} + \mu_0 M_S\right)}. \tag{3.3}$$

The Brillouin light scattering microscope measures spin waves of all possible wave vectors potentially up to the limit of $18\ \mathrm{rad/\mu m}$. Spin waves (in in-plane magnetized thin films) reach the highest frequency in the Damon-Eshbach mode and the lowest in the backward volume mode, all other modes will be located in the spectrum between them. By plotting the dispersions of these two borderline cases in Fig.3.7 (b) and (c) (with the correct parameters obtained as described below), we see a nice correspondence between the magnon modes and measured spectra. More importantly, we see that it is characteristic of backward volume spin waves that they don't reach significantly under the frequency of FMR. Therefore, we can obtain the FMR frequencies by looking at the beginnings of spectra – the frequencies were read out where the (slightly smoothened) spectrum first reaches 70 % of its maximum.

FMR frequencies obtained this way were fitted using the models (3.1) – (3.3) for the appropriate domains. Parameters of the fits were the saturation magnetization M_S and the anisotropy constant $K_{\mathrm{u}/1}$, while the gyromagnetic ratio was chosen to be constant $\gamma = 2\pi \cdot 29.3$ rad/Ts (and for later processing the exchange constant was set as $A_{\mathrm{ex}} = 11$ pJ/m, but in our measured range of wave vectors this changes the dispersion only minimally), which was experimentally obtained in similar transformed iron-nickle sample [57]. Resulting fitted FMR-curves are displayed together with the measured spectra in Fig.3.7 (d).

The saturation magnetization in domain (6) was found to be $M_S = 818$ kA/m and the anisotropy constant was found to be $K_{\mathrm{u}} = 6.3$ kJ/m^3 or expressed as the anisotropy field (1.26) $B_{\mathrm{u}} = 15$ mT. In domain (5) the best fit was found for $M_S = 905$ kA/m and $K_{\mathrm{u}} = 1.8$ kJ/m^3 or $B_{\mathrm{u}} = 4$ mT. Ratio of magnetizations in (6) to (5) is 0.9, which agrees well with the previously mentioned ratio of signals at saturation from the Kerr microscope. There seems to be a significant disagreement in strength of the anisotropies between the Kerr measurements and FMR-fits and in the case of FMR-fits we are also suspicious of the big difference of K_{u} between domains (6) and (5). First, the problem with obtaining the anisotropy from the BLS measurement in (5) could be some small-scale inhomogeneity at position of the laser spot. The laser spot was focused in (5) around the red circle shown in Fig.2.6 (a), near which some crystalline inhomogeneities are visible. And second, as was already mentioned above, the Kerr measurements have revealed that the apparent anisotropy field is not constant even inside the domains. This could be explained by the demagnetizing field given the large-scale inhomogeneity of the domain layout. With these considerations in mind, we expect the saturation magnetizations to be fitted approximately well along with the anisotropy in (6), while the anisotropy in (5) was probably measured more accurately by the Kerr microscopy in the large region and is likely around $K_{\mathrm{u}} \cong 6$ kJ/m^3. Given the obvious uncertainties, we do not report any confidence intervals and these results should be taken only as a first estimation. In the (alp) domain the saturation magnetization was fitted as $M_S = 342$ kA/m and the cubic anisotropy constant as $K_1 = 474$ J/m^3. Ratio of M_S in (alp) to (5) is 0.38, which is different from the 0.5 obtained from the Kerr measurement. This difference could be explained by some different material constant involved in the magneto-optical effect. Indeed, the alp domain is so different from the conventional domains that it is distinguishable from them even in a traditional light microscope.

The saturation magnetizations and magnetic anisotropies, which we have found, are somewhat lower than previously reported in a similar sample [57]. This discrepancy could be explained by a different ion dose, which was necessary for transformation (about ten times larger in our case). Other possible reason for the differences is that we have used a hot plate temperature of 150 °C in our fabrication process (see Section 2.1) or that at one point we needed to wash away unsuccessfully created antennas by an aggressive procedure using the NMP (1-Methyl-2-pyrrolidon), hot bath at 80° and an ultrasound bath.

For the purpose of plotting the dispersion relations in Fig.3.7, we have estimated the thickness of the transformed film d by comparing widths of the measured spectra in domain (6) with the frequency span of spin-wave dispersion [which was calculated from (1.68) using the parameters found in the fits of FMR] up to the limiting wave vector $18\ \mathrm{rad/\mu m}$. Good agreement was found for $d = 6$ nm, as is illustrated in Fig.3.7 (c). Fig.3.7 (b) confirms that this value is a match for measured spectra and dispersions in other domains too. This value of d should not be taken too seriously as it relies on the detection limit of $18\ \mathrm{rad/\mu m}$, which can easily be lower.

3.2.3 Brillouin light scattering – decay length

The goal of this thesis was to study spin wave propagation in structures with spatially varying anisotropy, which is (for the transformed iron-nickel films designed for refraction) covered in chapter 5. In this subsection, we only briefly inspect the decay length, a property that is unrelated to spatial variation of anisotropy.

Conductive antennas were fabricated using the EBL process (Section 2.1) on top of transformed structures [such as the one displayed in Fig.3.6 (a)] to excite spin waves. Here we study propagation of spin waves close to the Damon-Eshbach mode excited in the domains (5), (6) and (alp) on a given frequency and measured by the BLS around the same frequency. In the first two domains the measurement was performed without any external field, but in the (alp) domain type the decay length is in such case extremely low (also) due to the more complicated magnetization order, which was indicated in Fig.3.6 (c), and we have decided to apply an external field of 80 mT. Spin waves in the domains (5) and (6) were analyzed from measurements, which were designed for refraction, and we only inspect the space before any interface, while the (alp) domain decay length is analyzed from a dedicated measurement. All these measurements are shown in Fig.3.8 (a) – (c). The excitation antennas, outlined by yellow rectangles in Fig.3.8, were located on part of the left border of the measured areas.

The BLS signal was taken from rectangular areas just behind the antenna, as is sketched by the white rectangles, and we have averaged it over the direction perpendicular to propagation and subtracted the signal of thermal magnons, which was found from locations far away from the antennas. The resulting 1D signals are shown in Fig.3.8 (d) – (f) along with the fits, which were performed using cleaner parts of the signal to extract the decay length. The signal is not nice everywhere, because in the case of domains (5) and (6) there is some interference with reflected waves, which is more pronounced closer to the interfaces. And in the case of (alp) domain, the inhomogeneity of the BLS intensity map in Fig.3.8 (c) illustrates the low quality of this domain type.

It should be noted that BLS measures intensity of the spin waves ($\sim M^2$) and consequently the apparent fitted decay length should be multiplied by a factor of 2. In domain (5) the decay length of the Damon-Eshbach mode without any external field at 4 GHz was found to be $l_{(5)} = 3.4\ \mu\mathrm{m}$. In domain (6) the wave with almost the same conditions (just not exactly of the Damon-

Eshbach mode) had the decay length $l_{(6)} = 3.0$ µm. And in the (alp) domain the decay length of a spin wave at the frequency 6 GHz propagating perpendicularly to the 80 mT external field was found to be $l_{(alp)} = 1.5$ µm. The longer decay length in (5) than in (6) would agree with the previous finding of higher M_S in (5), which leads to steeper dispersion [as can be seen in Fig.3.7 (b)] and higher group velocity. However, these values should be taken only as some first estimate as deep investigation of this problematics was not a goal of this thesis.

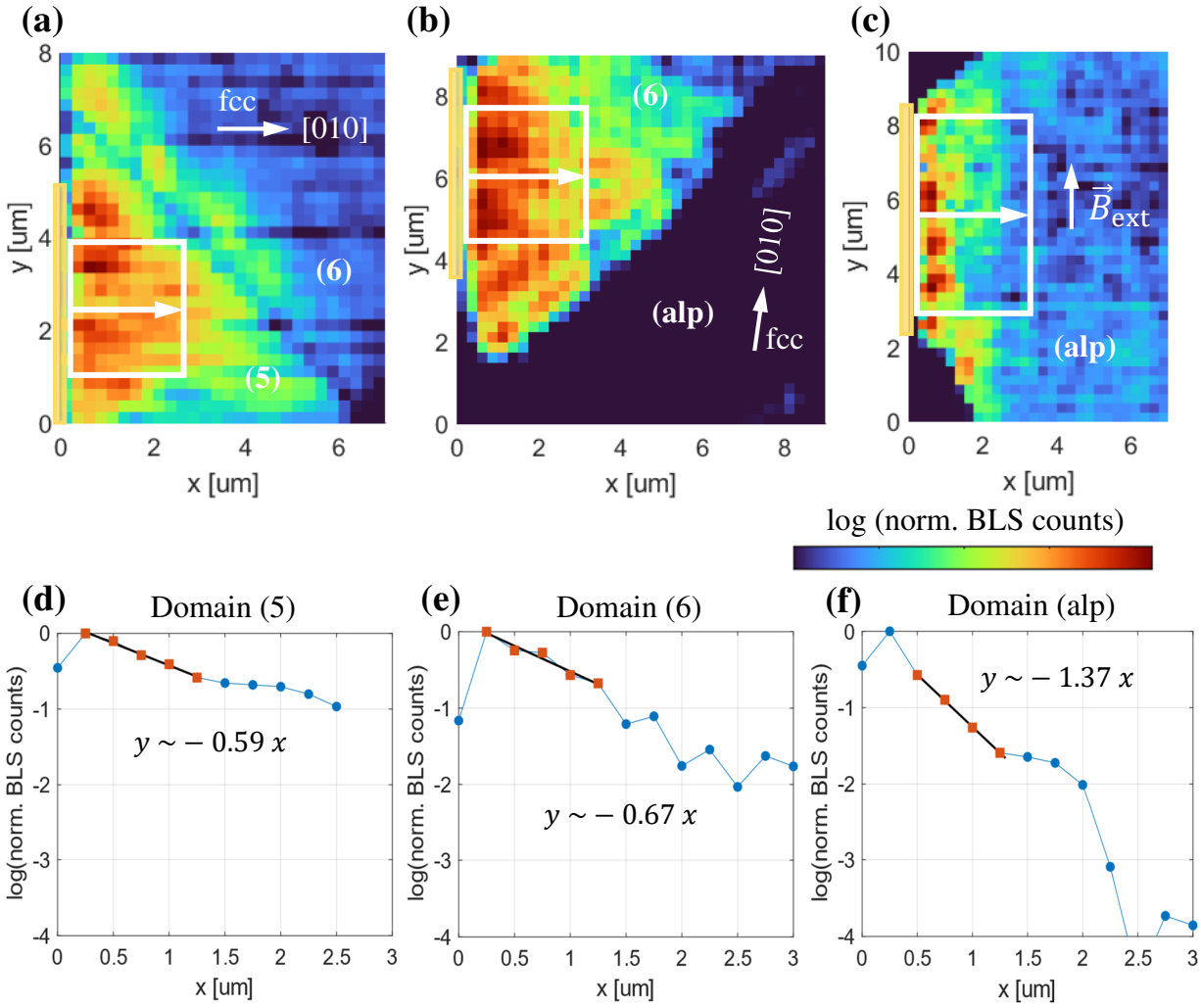

Fig.3.8: **(a)** BLS intensity map of a spin wave refracting on interface between (5) and (6). No external field was applied and the spin wave propagates as the Damon-Eshbach mode at the frequency 4 GHz. An excitation antenna was placed on part of the left border of the measured area. Signal around the top-right corner belongs purely to thermal magnons. **(b)** BLS intensity map of a spin wave intended for refraction on interface between (6) and (alp). Same parameters were used as in (a), only the mode was not exactly Damon-Eshbach (magnetization was not exactly perpendicular to excited wave vector). **(c)** Propagation of a spin wave in the (alp) domain. Magnetic field of amplitude 80 mT was applied perpendicular to the propagation direction and the frequency was 6 GHz. **(d)** Signal extracted from the white rectangle in (a), where the *y*-dependence was averaged and signal of the thermal magnons was subtracted. The logarithmized signal was fitted in a nice region (orange rectangles) by a line (black line). **(e)** Same as (d) but for the measurement of domain (6) shown in (b). **(f)** Same as (d) but for the domain (alp) shown in (c).

4 Wavy waveguides system

In this chapter we introduce the second magnetic system with modifiable magnetic anisotropy, which we have named wavy waveguides. As the name suggests, essence of this system is a periodic sine-like corrugation of a thin magnetic film, that creates an effective easy axis along the ridges of this corrugation, which in turn influences the static and dynamic behavior of the magnetic system.

Firstly, we will describe the fabrication process, which is based on focused electron beam induced deposition (FEBID). In the next section the geometrically induced anisotropy will be studied by micromagnetic simulations and demonstrated in experiments.

4.1 Fabrication of wavy samples

The idea of utilizing corrugation of magnetic films to induce magnetic anisotropy was already explored in systems prepared using the ion-beam induced erosion [58]–[61]. These studies examined the influence of period length [58] and height [59] of this modulation or the magnetic films thickness [58]–[60] on the resulting anisotropy, other studied the enlargement of frequency linewidth in the ferromagnetic resonance experiments caused by two-magnon scattering [61] if magnetization was aligned in the hard axis. These findings are relevant for the system prepared by focused electron beam induced deposition too.

In our case the fabrication of corrugated samples followed the procedures mastered by Igor Turčan as part of his doctoral research, who decided to use FEBID for its advantage in local controllability and precision of created structures over the ion beam erosion technique [62].

Our structures were fabricated on a substrate from GaAs using a scanning electron microscope (SEM) equipped with a gas injection system (GIS) (Tescan Lyra3). The GIS injects precursor (2,4,6,8,10-pentamethylcyclopentasiloxane) into the vacuum chamber very close to the electron beam. Molecules of the precursor adsorb on the samples surface and electrons from the electron beam break them into parts that stay attached to the surface (SiO_2) and volatile parts that fly away and are eventually pumped out of the chamber. The electron beam with the energy 30 keV and current 540 pA was scanned (with a step size ca 10 nm and dwell time 1 μs) several thousand times along lines, which at the end of the fabrication process correspond to the ridges of corrugation. Resulting height of the modulation h is in the order of several nanometers and spacing of the scanned lines defines the period Λ, fixed at 100 nm. The FEBID technique is sketched in Fig.4.1 (a).

In the next step we have used the electron beam lithography (described in section 2.1) to select region, where we want to deposit the magnetic material on. This region defines the waveguide and was always designed to be smaller than the area modified by FEBID to secure the waveguide being corrugated everywhere and therefore having the same desire corrugation-/geometrically induced anisotropy across the waveguide. Then the evaporator was used to deposit a $d = 10$ nm thick layer of permalloy ($Ni_{80}Fe_{20}$, $M_S = 827\ \mathrm{kA/m}, A_{\mathrm{ex}} = 13\ \mathrm{pJ/m}$), which was chosen for its reasonably low Gilbert damping constant $\alpha \cong 0.008$ and negligible crystalline anisotropy. Cross-section of a complete wavy waveguide is depicted in Fig.4.1 (b) and topography of a complete turned wavy waveguide is shown in Fig.4.2 (a).

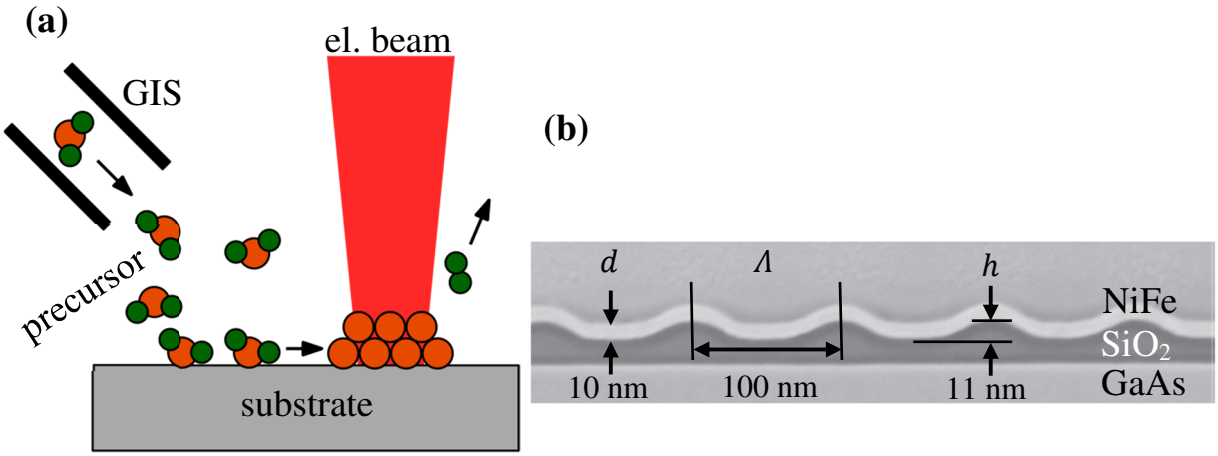

Fig.4.1: **(a)** Schematic of FEBID. GIS inserts molecules of the precursor in the chamber and some of them adsorb on the substrate's surface. Electrons then break these molecules into parts that get attached to the surface and volatile parts that get pumped away from the vacuum chamber. **(b)** Scanning transmission electron image of a cross-section of a complete wavy waveguide. The substrate is made of GaAs. SiO_2 was prepared by FEBID, which was scanned in lines, that are located on the positions of ridges of the final structure (perpendicular to the image plane). Non-zero size of the electron beam spot and the spread of secondary electrons results in the deposited lines of material having a certain width. Magnetic material was then deposited in an evaporator. Adapted from [63].

The final step of sample fabrication is about creating antennas to excite spin waves. This excitation is realized by passing a high-frequency (hf) current through a conducting strip placed on top of the magnetic waveguide. According to the Ampere's law the hf current creates a dynamic magnetic field around the strip, which drives the oscillations of magnetization in the magnetic material beneath. Width of the stripe defines the profile of this field and consequently the spatial spectrum of excited spin waves with narrower stripes exciting wider spectra. A useful and quick design clue states, that excitation efficiency's first minimum occurs for spin waves, whose wavelength is equal to the stripe's width [64] (the dynamic field tries to excite the wave in counter-phase at different places under the stripe). On the other hand, stripes that are very narrow are frail and more difficult to fabricate. Therefore, we have decided to use the width 1 micrometer. The conducting stripes are widened at the end to form the contacting pads, to which a probe with hf voltage source can be contacted.

The excitation antennas are also produced by EBL and in the evaporator. Precise structure of our antennas is Ti(5nm)/SiO_2(50nm)/Ti(5nm)/Cu(85nm)/Au(15nm), in which the purpose of titanium is adhesion and the function of SiO_2 is insulation. Copper and gold form the actual conducting stripe and contacting pads, with the gold serving also as a protection from oxidation for the copper. A finished sample with antennas is presented in Fig.4.2 (b).

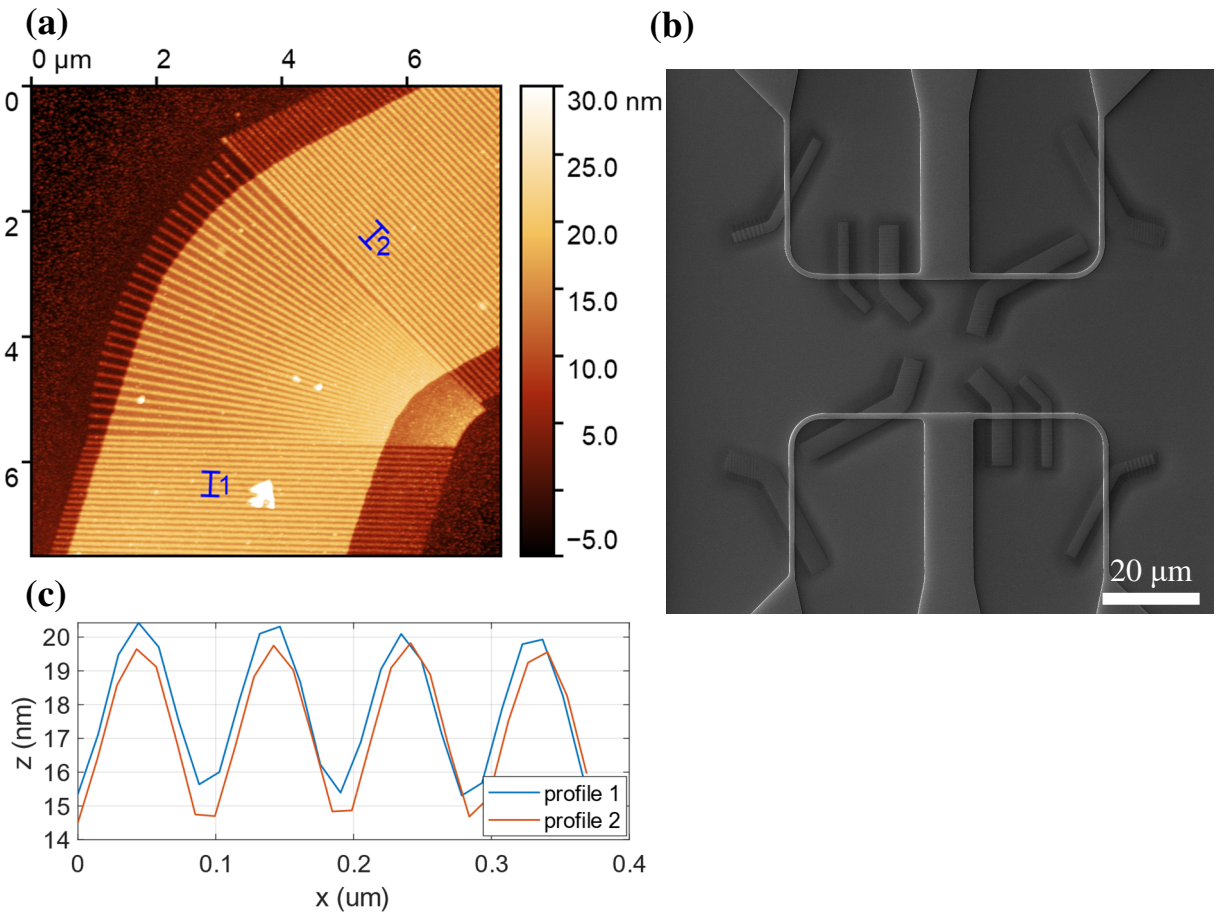

Fig.4.2: **(a)** Atomic force microscopy image of a wavy waveguide turn, measured by Igor Turčan. We can distinguish three regions – nonmodified substrate, wavy surface created by FEBID and wavy surface with permalloy on top of it. Corrugation changes period with radius in the turn leading up to fusion of the different lines on small radii. **(b)** SEM image of a complete set of structures, which includes antennas for excitation of spin waves for the Brillouin light scattering microscopy technique. **(c)** Profiles extracted from the atomic force microscopy measurement presented in (a). Corrugation was created by scanning the electron beam 5000 times along lines separated by Λ 100 nm resulting in height h around 5 nm. The height of modulation is generally larger in structures scanned more times, but its exact control is not possible this way, because it depends on many other parameters (such as the precursor pressure or the amount of precursor in the reservoir).

4.2 Geometrically induced anisotropy

In bulk magnetic samples the only anisotropy, that is present, is caused by the crystalline structure of the magnetic material as was described in subsection 1.1.4 (or by the magnetoelastic anisotropy 1.1.5). When we start restricting dimensions of the sample, the demagnetizing field (subsection 1.1.2) starts influencing the magnetization configuration according to the charge-avoidance principle, which leads to the magnetization favoring to be aligned along the longer axes of the sample. To describe this behavior, the idea of (overall) shape anisotropy is introduced. Including the corrugation of wavy waveguides in our system effectively causes another anisotropy to arise, which we will call geometrically induced anisotropy and whose origin lies again in the demagnetizing energy but, unlike for the (overall) shape anisotropy, the exchange energy contributes significantly too.

Since all of our wavy waveguide samples are made of permalloy, we don't need to bother thinking about the magnetocrystalline anisotropy. However, the (overall) shape anisotropy is relevant in our waveguides with their transversal dimensions of several micrometers, thicknesses of around 10 nm and lengths up to a few tens of micrometers.

4.2.1 Theoretical mechanism

As was noted above, the geometrically induced anisotropy, which can be for the static problem represented by the dependency of the total energy on the angle between magnetization and the corrugation, is caused by the combination of the nature of demagnetizing energy and of the magnetic body's corrugated character. The exchange interaction provides a certain contribution to the energy too and therefore makes the anisotropy stronger.

The cause of increase of the exchange energy (subsection 1.1.3) is straightforward – neighboring spin not being parallel causes an increase. The qualitative charge-avoidance principle states, that the demagnetizing energy (subsection 1.1.2) will generally be higher, if volume $\rho_M = -\vec{\nabla} \cdot \vec{M}$ and surface $\sigma_M = \vec{n} \cdot \vec{M}$ magnetic charges form ($\vec{n}$ is the outward normal to the surface). Therefore, demagnetizing energy will be greater for magnetization configurations pointing more out of the sample at its surfaces (and secondarily greater for bigger divergence of magnetization in the bulk).

This can help us explain origin of the static geometrically induced anisotropy, whose energy is high for magnetization aligned perpendicularly to the corrugation ridges and minimal for magnetization aligned along them (outlining the easy axis). Following Fig.4.3 we can start our thought process for explanation of this feature with the case, in which we set the magnetization to be parallel everywhere to minimize the exchange energy. Due to the corrugation of our magnetic body the magnetization points out of the sample at the sloped parts of the waveguide forming large surface charges. Demagnetizing field $\vec{H}_\mathrm{d}$ leads from positive charges (created by magnetization pointing out of the sample) to negative charges (magnetization pointing in the sample) meaning that it is quite antiparallel to the magnetization in most of the magnetic body and the total demagnetizing energy is very high as can be seen in Fig.4.3 (a). On the other hand, if we wanted to minimize the demagnetizing energy instead, we could order the magnetization to follow the corrugation and no surface charges would be created. However, in this case the exchange energy is higher [Fig.4.3 (d)] and even the demagnetizing energy is non-zero due to the volume magnetic charges [Fig.4.3 (c)]. Constraining the magnetization to be perpendicular to the ridges and finding the equilibrium configuration produces a more "natural[1]" result that is a mix of the two aforementioned cases. Nevertheless, even in this configuration the demagnetizing [Fig.4.3 (e)] and exchange energies [Fig.4.3 (f)] are not zero. It is clear, that these energies can be zero only if the magnetization aligns along the ridges (that is, in the *y*-axis in Fig.4.3). These insights explain the basis of the static geometrically induced anisotropic behavior.

[1] What we mean by this could be ambiguous. In our simulations the magnetization configuration in the constrained *xz*-plane is governed only by interactions, that cause the anisotropy. The same magnetization state could be achieved e.g., in samples with strong (overall) shape anisotropy forcing the magnetization to the *x*-axis. (We don't want samples of that kind due to low propagation length of the backward volume waves.) However, forcing the magnetization to the *x*-axis by e.g., an external field would lead to a different configuration (more parallel to the field / *x*-axis) and consequently to slightly different values of the demagnetizing and exchange energies, as can be seen later in Fig.4.4 (b).

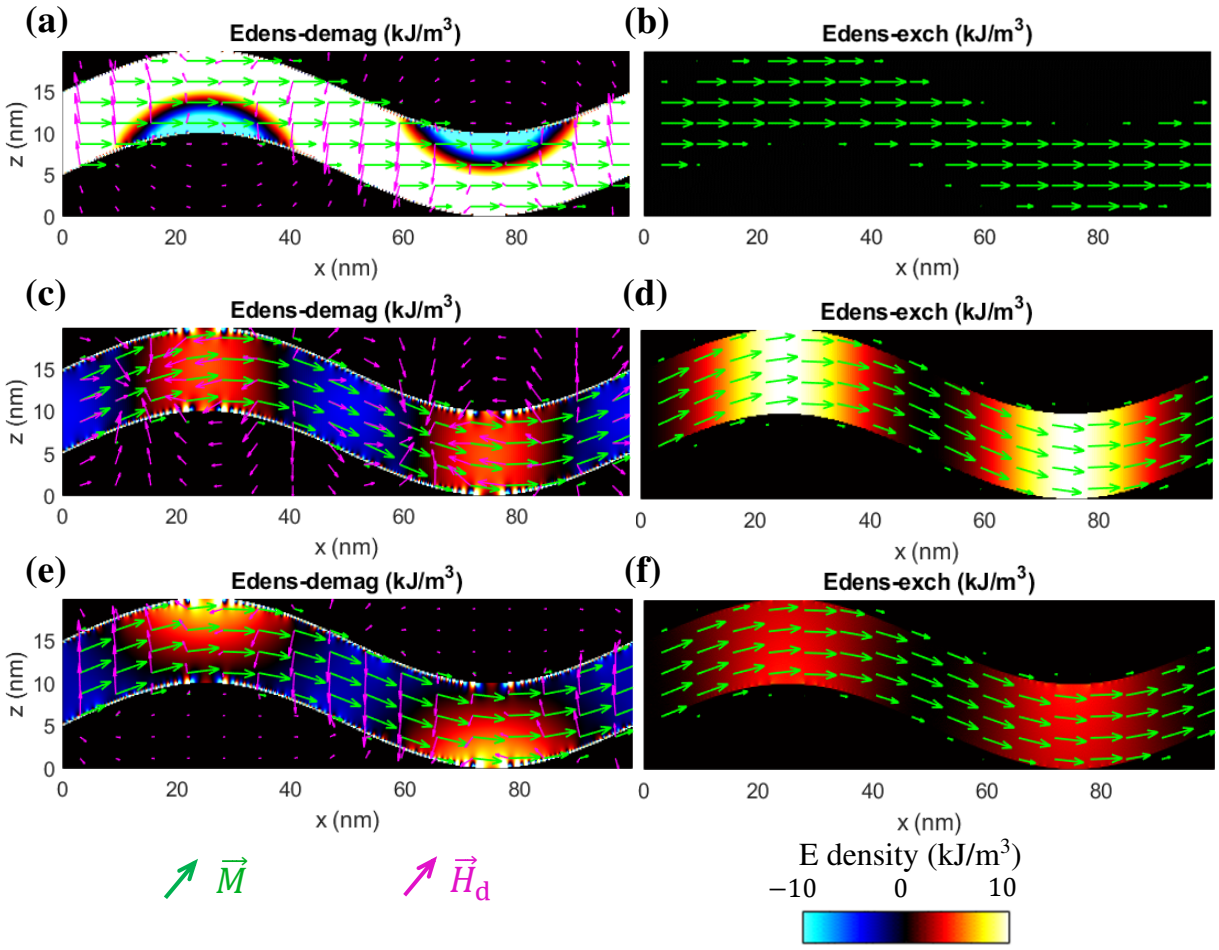

Fig.4.3: Simulations[1] explaining the static geometrically induced anisotropy, demagnetization field arrows are scaled for each figure separately. **(a)** Demagnetization energy density E_d in structure uniformly magnetized in the x-axis. The total averaged demagnetization energy density is 15.7 kJ/m^3. **(b)** Exchange energy density E_ex for the same magnetization state. Averaged exchange energy density is 0 J/m^3. **(c)** E_d in structure magnetized along the surfaces. Averaged E_d is 920 J/m^3. **(d)** E_ex for the same state, averaged E_ex is 4.8 kJ/m^3. **(e)** E_d in structure, whose magnetization was constrained to the xz-plane and relaxed to equilibrium. Averaged E_d is 1.2 kJ/m^3. **(f)** E_ex for the same magnetization state, averaged E_ex is 1.8 kJ/m^3.

Further simulations can show us, that the static geometrically induced anisotropy as a function of the angle θ between magnetization and the corrugation can be described by the typical uniaxial model (1.15) containing only the first term $\sim K_w \sin^2(\theta)$. This was investigated by rotating the plane, to which magnetization was artificially constrained, from the y-axis and saving energies of the equilibrium at each magnetization angle θ. Results of this are shown in Fig.4.4 (a).

[1] We have simulated 1 period of structure made of permalloy with parameters $\Lambda = 100$ nm, $h = 10$ nm and $d = 10$ nm. In the y-direction the simulated area was also 100 nm. Number of cells was $512 \times 512 \times 128$ and PBC $50, 50, 0$. The magnetization was set to either the parallel or sinusoidal state [for Fig.4.3 (a)-(d)] or was relaxed while being constrained in the xz-plane by an artificial hard-(y)-axis [for (e), (f)].

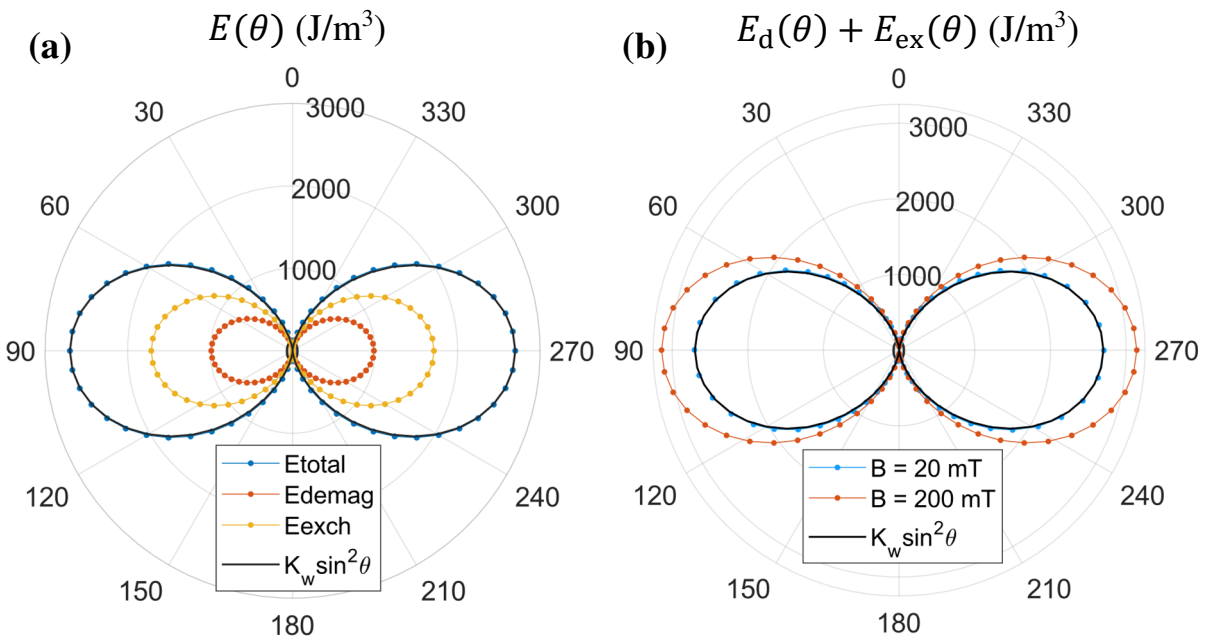

Fig.4.4: Simulations[1] of angular dependency of the averaged energy density $E(\theta)$, $\theta = 0$ corresponds alignment of magnetization along the ridges (y-axis). **(a)** Magnetization was constrained by an artificial hard axis (/ easy plane) with an angle step 5° and relaxed to equilibrium. Energies were averaged over the whole simulated area. The static behavior of the wavy waveguide system can be described by the model (1.15) of uniaxial anisotropy containing only the first term as can be seen from adding the corresponding series $K_w \sin^2(\theta)$, where $K_w (= 2.7\ \mathrm{kJ/m^3})$ was taken from the simulated energy maximum. **(b)** Simulation containing rotating uniform external field instead of the artificial anisotropy. Angle θ is defined by the angle between the equilibrium magnetization and the ridges, which is not the same as the angle of external field, especially in the lower field simulation. It can be seen that the sum of demagnetizing and exchange energies (caused by the corrugation) changes when we apply higher fields. This is caused by magnetization being more parallel with the field and consequently resembling more the high-energy state presented in Fig.4.3 (a). The $K_w \sin^2(\theta)$ series, from the simulation in (a), is added to show, that the anisotropy as defined by the constrain agrees well for configurations created by weak fields.

We have also performed simulations, in which the magnetization is rotated not by the artificial hard-axis anisotropy, but by an external field. The results are shown in Fig.4.4 (b). At low magnitudes of external field, the anisotropic behavior is the same as in the constrained case, suggesting, that the magnetization profile is still predominantly determined by the exchange and demagnetization energy. At higher fields, these two energies are higher at the expense of the Zeeman energy, because the magnetization is more parallel and resembles more the high energy case in Fig.4.3 (a).

[1] One period of structure made of permalloy with parameters $\Lambda = 100$ nm, $h = 10$ nm and $d = 10$ nm was simulated. In the y-direction the simulated area was also 100 nm. Number of cells was $128 \times 128 \times 32$ and PBC $400, 400, 0$. Parameter 'edgesmooth = 8' was used to compensate for the stairyness of the material border due to discretization.

Examining the exact dependence of the geometrically induced anisotropy on the various possible parameters Λ, h, d and M_S goes beyond the scope of this thesis. Some analytical calculations were made for the exchange energy of magnetization aligned along the surface [as in Fig4.3 (d)] in [59]. The same paper also provides some estimates for the demagnetization energy from the volume charges [as in Fig.4.3 (c)] and calculation of the demagnetizing energy due to the surface charges when the magnetization is parallel [as in Fig.4.3 (a)]. Generally, strength of this anisotropy declines with increasing period Λ of the structure [58], [65] and (beyond a first few nanometers) with increasing thickness d [58]–[60]. Naturally, it gets stronger with increasing modulation h [59], [63]. From the formulations of exchange (1.14) and demagnetization [(1.2) and (1.10)] energies it is obvious, that the exchange part of geometrically induced anisotropy is (directly) independent of M_S while the demagnetization part depends on this quantity (directly) as $\sim M_S^2$.

So far, we have been dealing with the static problem, in which the wavy waveguides behave (in the spatially averaged view) as films with normal uniaxial anisotropy if the external field is weak. Investigation of the geometrically induced anisotropy gets more complicated for the dynamic problem of ferromagnetic resonance (FMR) and even more complicated for propagating spin waves. We can provide at least a limited insight by approaching this problem the same way as in the beginning of subsection 1.3.1 – by dividing the magnetization $\vec{M}$ and effective fields $\vec{H}_{\mathrm{eff}}$ into large static and small dynamic parts as $\vec{M}(\vec{r},t) = \vec{M}_0 + \vec{m}(\vec{r},t)$, where the static part $\vec{M}_0$ has only the *y*-component and the dynamic $\vec{m}$ the *x*- and *z*-components (same for $\vec{H}_{\mathrm{eff}}$, see the mentioned subsection).

In thin flat films magnetized along the axis of a magnetocrystalline uniaxial anisotropy, the effective field of this anisotropy $\vec{H}_{\mathrm{uni}}$ (1.27) is static and parallel with the static magnetization. Applying a static external field $\vec{H}_{\mathrm{ext}}$ parallelly to them, leads to the effects of the anisotropy and the field on the magnetization precession being the same. Torque caused by these two magnetic interactions is given by the term with dynamic magnetization and the static fields $-\gamma\mu_0\vec{m}\times\left(\vec{H}_{\mathrm{ext}}+\vec{H}_{\mathrm{uni}}\right)$. This torque alone would drive a circular precession around the fields. However, the dynamic demagnetization field $\vec{h}_{\mathrm{d}}$, which for the spatially uniform FMR originates from the dynamic parts of magnetization pointing out of the film's plane and which is proportional to $-m_z$, drives the magnetization excitation purely in the in-plane *x*-direction by the torque $-\gamma\mu_0\vec{M}_0\times\vec{h}_{\mathrm{d}}$ and the total precession trajectory is then elliptical. FMR frequency of such a system is given by (3.1).

In a thin flat film without any anisotropy or external field the FMR (eigen-)frequency is zero, which is expectable since there would be no (non-damping) torque driving the magnetization in the out-of-plane direction and the demagnetization field and torque would consequently stabilize at zero too. However, the situation is different in corrugated thin films, in which the FMR frequency is non-zero even without any field or crystalline anisotropy as can be seen in results of simulations in Fig.4.5 (a) and we can attribute this feature to some dynamic geometrically induced anisotropy. The demagnetizing field $\vec{h}_{\mathrm{d}}$ (created by the dynamic components of magnetization $\vec{m}$ pointing out of the magnetic body) is in the corrugated films

spatially nonuniform. During most phases of the precession[1], its profile looks like in Fig.4.5 (b) – the demagnetizing field is approximately perpendicular to the local surface. Consequently, the elliptical precession is tilted according to the local surface, as is displayed in Fig.4.5 (c) for several locations. It is obvious from this figure that the magnetization is generally not spatially uniform in each point in time. This creates the effective field of the exchange interaction $\vec{h}_{\mathrm{ex}}$, which is proportional to $\vec{\nabla}^2\vec{m}$ [as is governed by equation (1.22)].

In the first place, we are interested in the phase of precession, during which the dynamic magnetization is aligned predominantly parallelly to the surfaces. This is analogous to the mentioned problematic phase in the flat film, which lacks any out-of-plane torque. We have plotted the dynamic parts of magnetization for this phase of precession in the corrugated film without any external field in Fig.4.5 (d). It is visible that the *z*-component of $\vec{m}$ changes very rapidly compared to the *x*-component, and consequently the $\vec{h}_{\mathrm{ex}}$ will be mostly oriented in the *z*-direction. Fig.4.5 (d) also shows the demagnetizing field $\vec{h}_{\mathrm{d}}$, which is small in this phase but still remains mostly perpendicular to the surfaces. What determines, whether the magnetization can autonomously precess and the eigen-frequency of FMR at zero field is not zero GHz, is the presence of some out-of-surface torque in this phase. (The in-plane/along-surface torque in a whole range of phases of precession is readily created by the demagnetization field.) Therefore, we display the torques corresponding to the exchange $\vec{T}_{\mathrm{ex}} = -\gamma\mu_0\vec{M}_0 \times \vec{h}_{\mathrm{ex}}$ and demagnetization fields $\vec{T}_{\mathrm{d}} = -\gamma\mu_0\vec{M}_0 \times \vec{h}_{\mathrm{d}}$ in Fig.4.5 (e). The alignment of $\vec{h}_{\mathrm{ex}}$ in *z*-direction is important here because the corresponding torque $\vec{T}_{\mathrm{ex}}$ then moves the magnetization in the *x*-direction, which contains a component that is perpendicular to the surfaces in the sloped segments of the corrugated film. This[2] allows precession of magnetization even without the presence of an external field and can be considered the origin of what we call the dynamic geometrically induced anisotropy.

An interesting feature visible in the FMR simulations of the corrugated films [displayed in Fig.4.5 (a)] is that it does not follow the typical model of FMR frequency in thin films with crystalline uniaxial anisotropy (3.1). This should not be surprising given the fundamentally different nature of the two anisotropies. With increasing field, the frequency becomes lower than it would be in a film with corresponding crystalline anisotropy and at larger fields it gets even below the FMR frequency of a film without any crystalline anisotropy. The strange nature is also reflected in the difference between the static and dynamic geometrically induced anisotropies in exactly the same simulated structure, which were obtained from the energy in hard axis [$K_w = 2.7\ \mathrm{kJ/m^3}$, Fig.4.4 (a)] and from the FMR frequency at zero field respectively [$K_w = 2.35\ \mathrm{kJ/m^3}$, Fig.4.5 (a)] (by considering the crystalline uniaxial anisotropy models).

[1] The profile of $\vec{h}_{\mathrm{d}}$ is the most different when the dynamic magnetization is parallel to the surface in one of the sloped segments. Then, the field is almost zero in the given segment, but not totally zero in the second sloped segment, because the phase of precession does not change between different locations exactly as the ellipticity is tilted. Similar case is shown in Fig.4.5 (d). Nevertheless, such narrow cases are not important for the qualitative explanation of the tilted elliptical nature of precession, because the field is proportional to the outward facing component of magnetization that is small when $\vec{m}$ is nearly parallel to the surfaces.

[2] In the peaks and valleys, even the nonuniform demagnetizing field contributes a little bit to the out-of-surface torque in this phase of precession as can be seen in Fig. 4.5 (e).

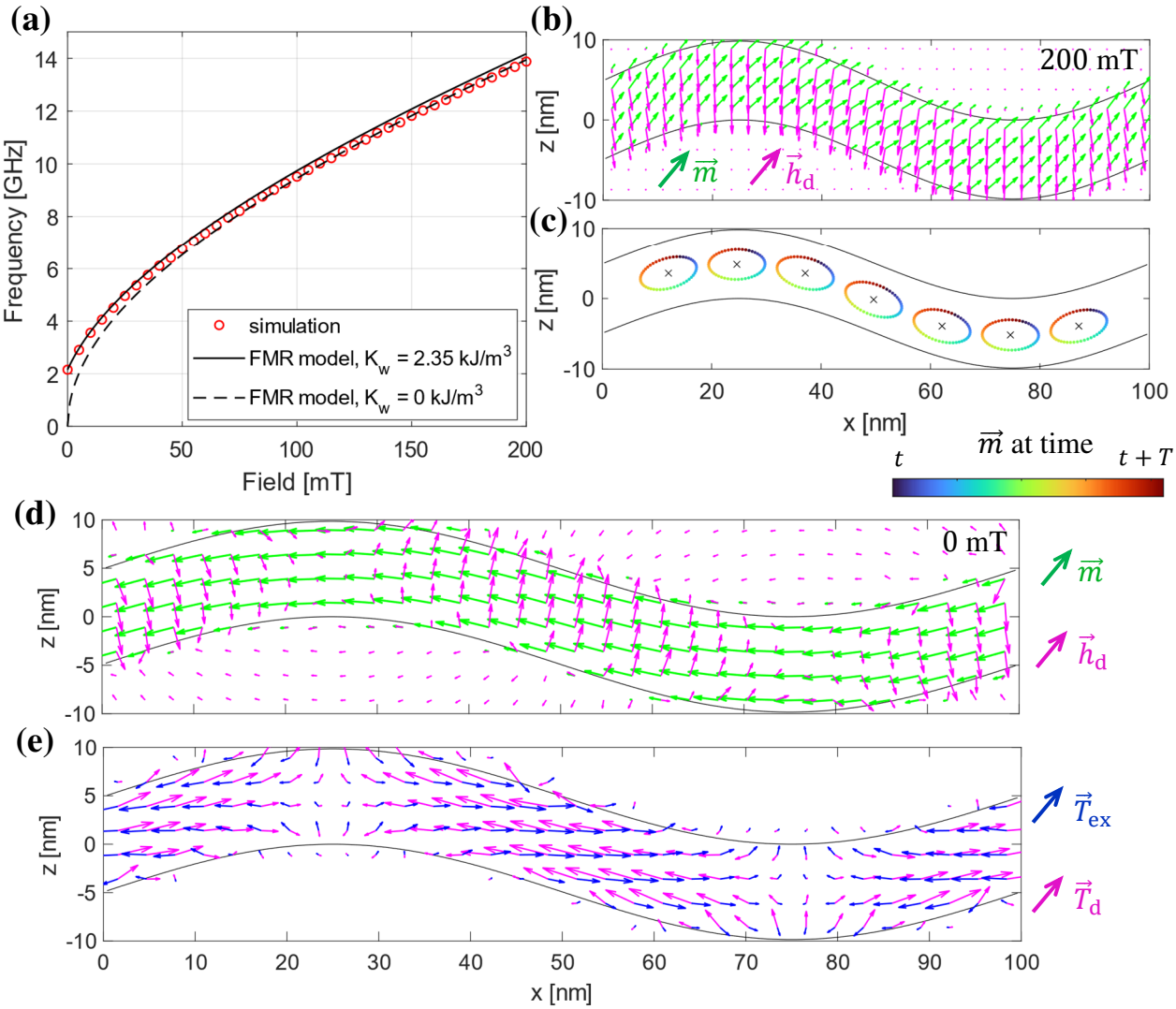

Fig.4.5: Simulations of FMR in the same corrugated film as in Fig.4.4. **(a)** The structure was relaxed at different external fields parallel with the easy (y-)direction (which was described in the static case) and then was excited with a small spatially uniform external field with a sinc-function time dependence. The response of magnetization is largest at the FMR frequency, which is displayed by the red circles. Solid black line was calculated using the model (3.1) with K_u obtained from the zero-field frequency. Dashed black line uses the same model with no anisotropy. **(b)** Snapshot of the dynamic magnetization $\vec{m}$ and demagnetization field $\vec{h}_\mathrm{d}$ in the steady state from a simulation with the external field 200 mT and harmonic excitation exactly at the FMR frequency. **(c)** Precession (multiplied by 20000) over one period is shown at several locations of the structure to highlight its tilted elliptical shape, which is caused by the demagnetization field. Obtained from the same simulation as (b). Precession is more elliptical at weaker external fields. **(d)** Snapshot of $\vec{m}$ and $\vec{h}_\mathrm{d}$ in the most in-plane phase of precession from a similar simulation but with zero external field. Amplitude of the demagnetizing field is much smaller here than in (b) because the out-of-surface component of $\vec{m}$ is small. **(e)** Torques from the same simulation and time as (d). Torque caused by the demagnetization field $\vec{T}_\mathrm{d}$ drives the magnetization precession mainly along the surfaces, while the torque of exchange field $\vec{T}_\mathrm{ex}$ has also a certain out-of-surface component, which allows precession even without any external field.

We have also simulated spin wave propagation in the wavy waveguides. 300 periods of the same structure were simulated with no external field and with only 1 cell in the *y*-direction and no edge-smoothing to make the big simulation faster. An excitation field with a sinc profile in space and time was used to excite spin waves of a whole range of frequencies and wave vectors. The response of magnetization was averaged through the *z*-direction, multiplied by the Hanning window and 2D Fourier transformed to obtain the magnitudes of the spin wave modes present in the system. Peaks of this quantity correspond to the spin wave dispersion relation and are displayed in Fig.4.6 together with a flat reference and the model (1.68), both with anisotropy constant[1] $K_\mathrm{u} = 5\ \mathrm{kJ/m^3}$ to match the frequency at zero wave vector.

We observe a discrepancy between modes in the wavy waveguide and the flat reference with increasing wave vector. At higher wave vectors the frequency is lower in the wavy structure. It could be suggested that the spin waves must travel longer distance in the corrugated structure and their wavelength is actually longer (and their wave vector smaller) that it appears to be when we trace it simply along the *x*-axis. Nevertheless, in the experimentally accessible range the discrepancy is very small as can be seen in Fig.4.6 (b). More importantly, direction of the anisotropic spin wave dispersion is defined with respect to the direction of the equilibrium magnetization, which was shown in Fig.1.4. Therefore, we can adjust the direction of corrugation to choose the mode, with which we work. Often, this means fabricating the ridges perpendicularly to the propagation to work with the high-group velocity Damon-Eshbach mode.

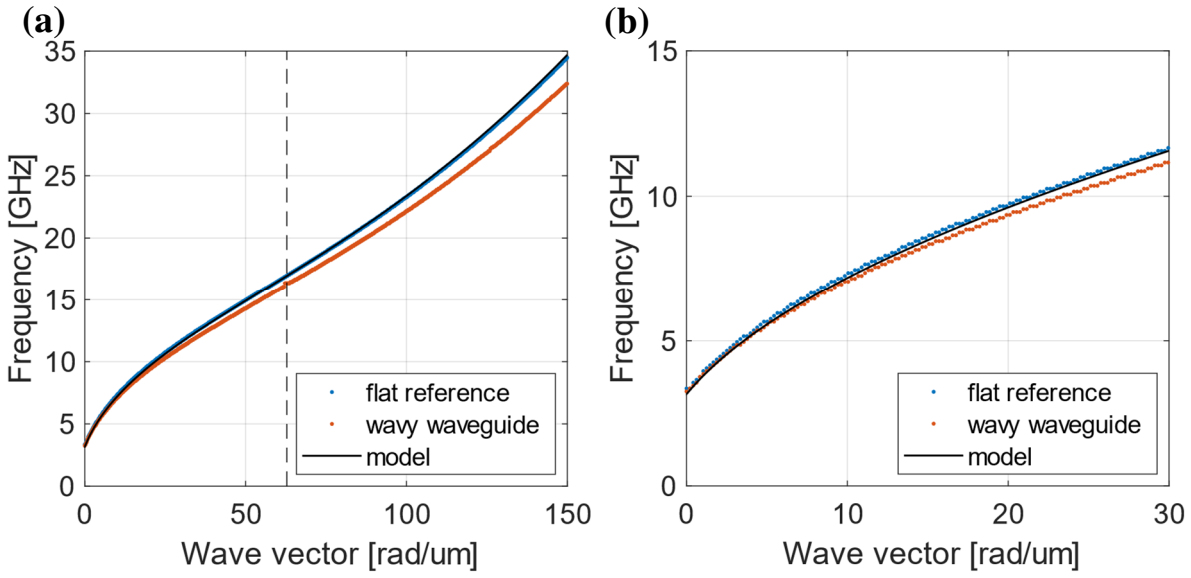

Fig.4.6: Simulation[2] of propagating Damon-Eshbach spin waves in a wavy waveguide and a flat reference waveguide. Accompanied by model (1.68) with $K_\mathrm{u} = 5\ \mathrm{kJ/m^3}$. **(a)** Dispersion relations in the whole simulated range of frequencies and wave vectors. The dashed line corresponds to the "wave vector" of geometry. **(b)** Zoomed area of wave vectors more easily accessible in the experiments.

[1] This value is different from the one in Fig.4.5 due to the different number of cells in the *y*-direction, different PBC and no edge-smoothing.

[2] 300 periods of wavy waveguide made of permalloy with parameters $\Lambda = 100$ nm, $h = 10$ nm and $d = 10$ nm were simulated. In the *y*-direction the cell size was 5 nm. Number of cells was $16384 \times 1 \times 32$ and PBC $1, 9000, 0$ to simulate an approximately square area. An excitation with a sinc spatial and temporal dependency was used (the cut-off frequency was 40 GHz and the cut-off wave vector 150 rad/μm). The flat reference simulation had only 16 cells in the *z*-direction to keep the cell size constant. No external field was applied.

4.2.2 Experimental investigation of anisotropy

The anisotropic behavior of the wavy waveguide system was observed in a number of experiments. This system was investigated thoroughly by Igor Turčan in his doctoral research, and we show some of his experiments concerning the static problem in Fig.4.7. The static anisotropy was studied in corrugated disks to remove effects of the (overall) shape anisotropy [63]. Hysteresis loops were measured in the Kerr microscope in the easy and hard axes, which allowed the determination of uniaxial anisotropy field (1.26). The angular dependence of remanence magnetization showed clear uniaxial behavior, that is, at zero field the magnetization aligned along the ridges as is shown in Fig.4.7.

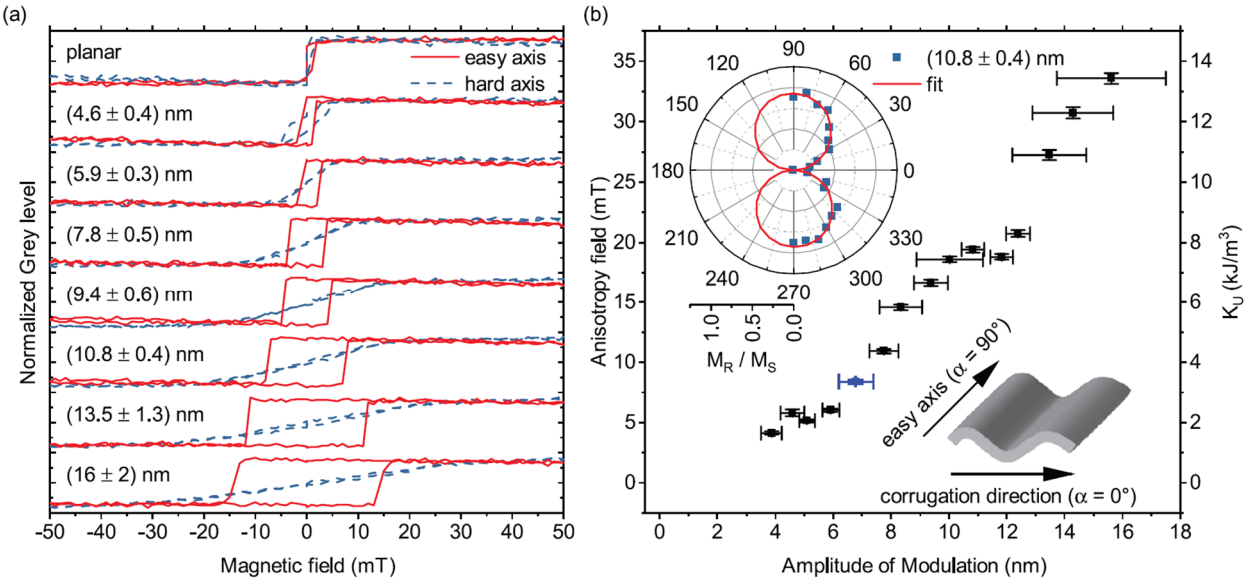

Fig.4.7: **(a)** Hysteresis loops measured by the Kerr microscope in corrugated permalloy disks with the field and detected component of magnetization being aligned along the easy and hard axes defined by the corrugation direction. Structures with different amplitudes of modulation were fabricated, determined by the atomic force microscopy, and measured in the Kerr microscope [63]. **(b)** Dependence of strength of the static geometrically induced anisotropy on the amplitude of corrugation. The anisotropy field was determined from hysteresis loops [examples of which are in (a)] by finding the field, which was necessary to saturate the magnetization in the hard axis. The inset shows the normalized magnetization remanence in a structure with modulation 10.8 nm as function of the angle from the hard direction, $\alpha = 90°$ is the direction of corrugation and easy axis. The pattern displays clear uniaxial behavior – the magnetization at zero field aligns along the ridges. All taken from [63].

The dynamic geometrically induced anisotropy was measured in wavy waveguides prepared for spin wave propagation (and turning). The laser spot in the Brillouin light scattering microscope was focused at the middle of a straight part of the waveguides, whose corrugation was transversal to the long axis of the waveguides to operate at the Damon-Eshbach mode, and an external field was applied parallel to the ridges, that is, in the easy axis of the geometrically induced anisotropy. Layout of the experiment is outlined in Fig.4.8 (a). A flat reference waveguide was also measured.

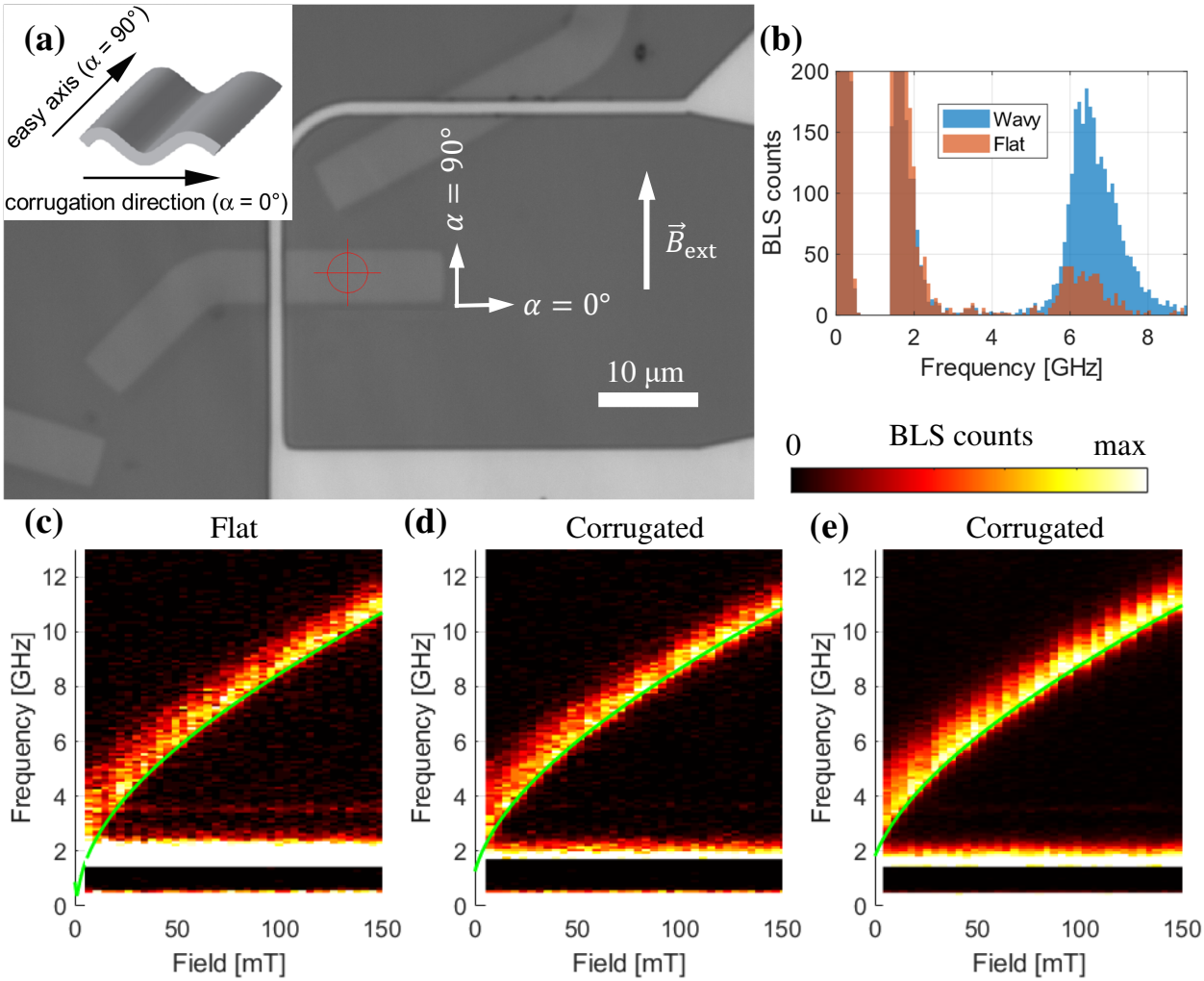

Fig.4.8: **(a)** Layout of the BLS experiment – laser (red crosshair) was focused at the straight part of waveguides with transversal ridges (and a flat reference). External field was applied parallel to the easy axis of geometrically induced anisotropy. The excitation antennas (white) were not used, and we have measured the thermal populations of magnons. The picture of wavy waveguide on the left was taken from [63]. **(b)** Thermal spectra measured in the corrugated and flat films [in (e) and (c)] at 50 mT. Due to the tilt of elliptically shaped precession [Fig.4.5 (c)] and the fact that the BLS microscope is more sensitive to the dynamic z-component of magnetization, the magnon signal is stronger in the corrugated film. (In contrast, the laser-mode peak around 2 GHz has the same intensity in both measurements.) **(c)** BLS spectra measured at different external fields in the flat reference. Green line is the fit by the model (3.1). Measurement with external field in the short axis of the waveguide results in a negative (shape) anisotropy -1.2 mT. **(d)** BLS spectra measured in a corrugated waveguide. The saturation magnetization is the same as in (c) because the material was deposited on both structures at the same time, and the apparent anisotropy is caused by the corrugation. Strength of the anisotropy was found from the first few spectra around zero external field and the green line shows the model (3.1). As in Fig.4.5, at higher fields the FMR frequency shows a shift with regards to the magnetocrystalline model. **(e)** Measurement of a structure like the one in (d) but prepared and measured in separate sessions. Proper acceleration voltage was used in the FEBID procedure and the stronger induced anisotropy suggests a higher modulation h than in (d).

The FMR frequency was found again (as in Fig.3.7) by looking for frequency where the BLS signal first reaches 70% of the maximum. We have fitted the data for the flat reference by the model (3.1) with the anisotropy constant and saturation magnetization being the fit parameters and the gyromagnetic ratio was set constant $\gamma = 2\pi \cdot 29$ rad/Ts [66]. The saturation magnetization was found to be $M_S = 609$ kA/m and the anisotropy constant $K_\mathrm{u} = -370\ \mathrm{J/m^3}$ or in the terms of anisotropy field $B_\mathrm{u} = -1.2$ mT. This constant was expected to be negative because of the (overall) shape anisotropy and the magnetization being aligned in the short axis of the waveguide, and because the permalloy should have no crystalline anisotropy. The permalloy on corrugated waveguides was deposited in the same Evaporator from the same crucible with permalloy, and the structure measured in Fig.4.8 (d) was even deposited during the same session as the flat structure in Fig.4.8 (c). Therefore, the material parameters should be the same. In the corrugated structures, we have found the strength of anisotropy by fitting only the first few data points near the zero field with only the anisotropy constant being the fit parameter (and the M_S being constant, which was found in measurement of the flat structure). This way we have found the anisotropy constants $K_\mathrm{u} = 750\ \mathrm{J/m^3}$ for the measurement in Fig.4.8 (d) and $K_\mathrm{u} = 1560\ \mathrm{J/m^3}$ for Fig.4.8 (e). Removing the effect of the (overall) shape anisotropy, the dynamic geometrically induced anisotropies should be $K_\mathrm{w} = 1100\ \mathrm{J/m^3}$ or 3.6 mT in the first structure and $K_\mathrm{w} = 1900\ \mathrm{J/m^3}$ or 6.2 mT in the second. Both of these structures were fabricated using 7000 scans and the same FEBID-command-file, but in the session for fabricating the first structure [Fig.4.8 (d)] we have inappropriately used a lower electron-acceleration voltage (20 kV instead of 30 kV). This typically results in larger electron beam spot size and more blurry structures, in our case in lower modulation h of the corrugation. This explains the weaker geometrically induced anisotropy in this structure. The second corrugated structure was fabricated correctly with the help from Igor Turčan.

First and foremost, this experiment has demonstrated presence of the dynamic geometrically induced anisotropy and has provided an estimate of its strength in our structures. Secondarily, we observe [in Fig.4.8 (d) and (e)] the same mismatch between the anisotropic FMR model (3.1) and the measured dependency of the frequency on external field as in the simulations (Fig.4.5), which shows the different nature of this anisotropy compared to the magnetocrystalline anisotropy. Lastly, we have observed a stronger signal of thermal magnons in the corrugated structure, even on approximately the same frequencies as can be seen in Fig.4.8 (b). The Rayleigh-scattered laser-mode at 2 GHz had the same intensity in both measurements signifying that the difference in the inelastically scattered light is caused by a different interaction of the light with magnons. In the BLS setup, which we have used, the light is guided through the whole aperture of our objective and consequently the equivalent of the longitudinal Kerr signal is cancelled out and we detect only signal proportional to the z-component (like polar Kerr). Then, it is obvious that the signal is higher in the corrugated structure because of the tilt of the elliptical precession, which can be seen in Fig.4.5 (c).

5 Refraction of spin waves

In the introduction, the need of routing spin waves between various components on a chip was mentioned, which would be necessary for a successful magnonics application. Refraction on an interface presents the simplest case of guiding waves and a basic building block for some of the more complex means of turning waves, examples of which are shown in the next chapter. In this chapter we demonstrate refraction of spin waves between different domains of the transformed iron-nickel thin films, which were discussed in chapter 3.

The preparation process of the magnetic domains is described in the aforementioned chapter, which also includes an overview and inspection of magnetic properties of one of the transformed areas in Fig.3.6 (a). After the transformation, excitation antennas made of Ti(5nm)/SiO_2(50nm)/Ti(5nm)/Cu(85nm)/Au(15nm) were fabricated using the electron beam lithography process (described in section 2.1). Purpose of the SiO_2 layer was to insulate the conductive antenna from the metallic sample and the Ti layers have been deposited for better adhesion. The Cu and Au layers form the actual conductive antenna with the Au layer serving also as a protection from oxidation of the Cu. High-frequency current in the conductive strip creates a dynamic magnetic field, which excites the spin waves. Width of the antennas determines the width of the excited spectrum of wave vectors with narrower stripes exciting wider spectra [64]. The first minimum of excitation efficiency occurs for wavelength equal to the width of the antenna and the efficiency is generally low afterwards. We have exploited this feature to excite spin waves only at desired locations by making the conductive structure very wide elsewhere. Transformed areas with antennas are displayed in Fig.5.1.

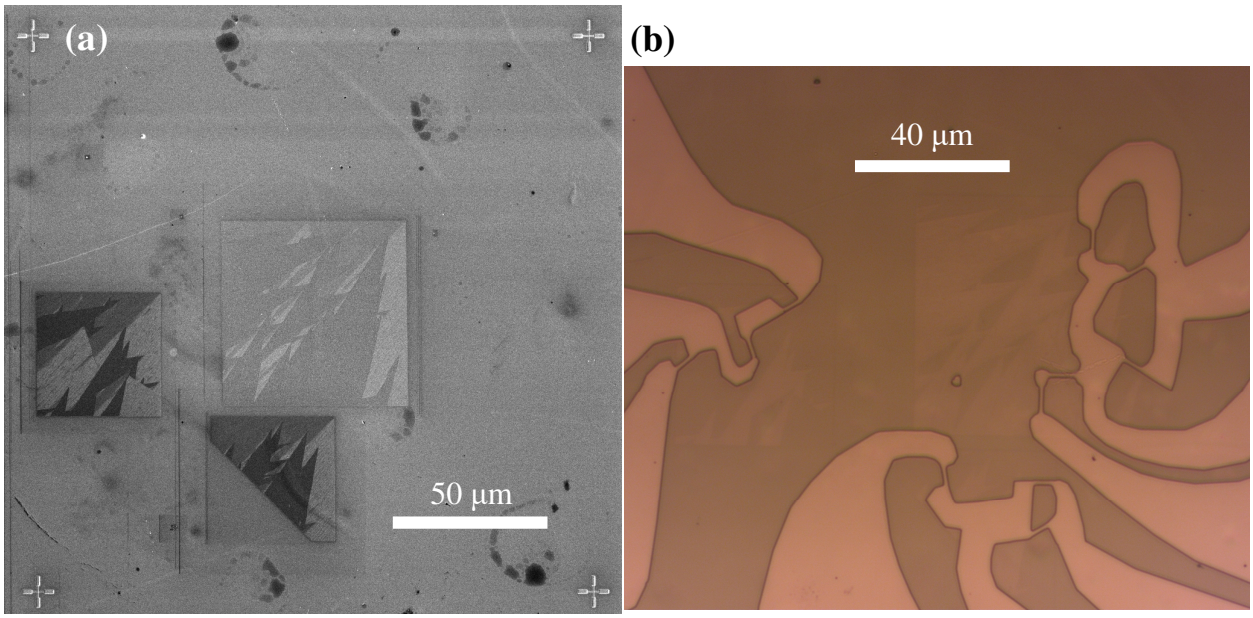

Fig.5.1: **(a)** SEM image of the tilted (4°) sample with three transformed areas. The transformed areas were designed to be made of the domains (6) (dark gray) and (5) (white) and an interface along [110] of the fcc lattice between them, as was discussed in section 3.2. An undesired (alp) domain (black) with inferior qualities was also created. The structure in the middle was created in an earlier session and exhibits lower contrast between the different domains. The four FIB-drilled marks in the corners served for proper alignment in the EBL process. **(b)** Light microscope image of the same complete structure with excitation antennas. Excitation of spin waves was intended to occur at the narrow parts of antennas.

5.1 Refraction from domain (6) to domain (5)

In this section, measurement of refraction from the domain (6) to domain (5) will be presented, where the incident spin wave mode had an angle approx. 60° from the Damon-Eshbach orientation. Location of this measurement can be found in the top-right corner of the left transformed rectangle in Fig.5.1 (a) and (b). Geometry of the experiment can be found in Fig.5.2 (a), where the design of antenna for the EBL process is shown on top of a (tilted) SEM image.

As the first step in this kind of measurements, we inspect, on which frequency the spin waves propagate the best, by changing the excitation frequency (frequency of current in the antenna) and measuring the magnon spectra at certain locations of interest – in this case the BLS laser spot was focused before and behind the interface as is sketched in Fig.5.2 (a) by the red circles. Results of these experiments are displayed in Fig.5.2 (b). Since we want to observe refracting waves, we need to work at frequency, on which the waves behind the interface have high enough intensity. By looking at the spectra behind the interface, we have decided to work at the frequency 3.75 GHz.

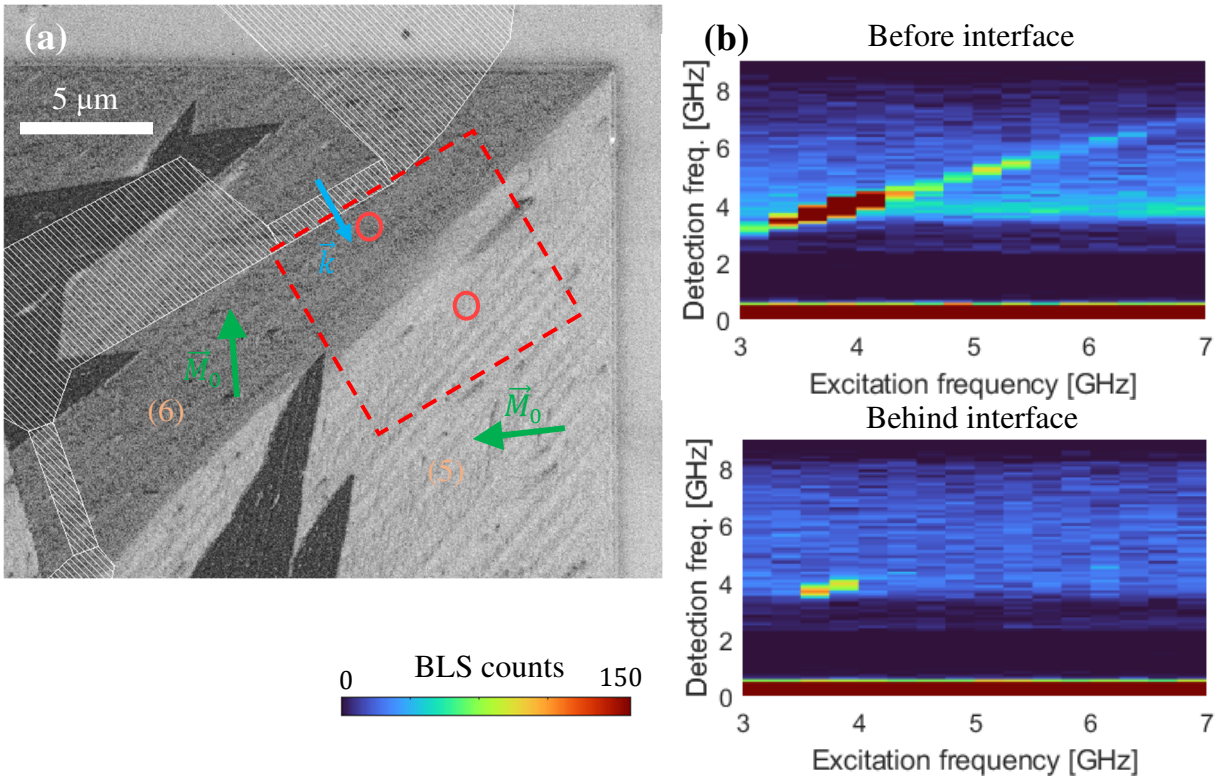

Fig.5.2: **(a)** Tilted (4°) SEM image of the area for refraction from domain (6) to (5) with the design drawing for the excitation antenna. The easy axis direction was found by the Kerr measurement (presented in Fig.3.6) and since we did not apply any static external field, the magnetization will be aligned in these directions as is sketched by the green arrows. Red circles show the locations of measurements for finding frequency, on which the waves propagate well, that is, the measurement in (b). Red rectangle shows the position of the 2D-BLS measurement of the refracting waves. **(b)** BLS measurements at the two spots outlined in (a) for different excitation frequencies. The detected signal is a sum of thermal and excited magnons. Because we are interested in propagating the wave behind the interface, we have chosen to work at the frequency 3.75 GHz.

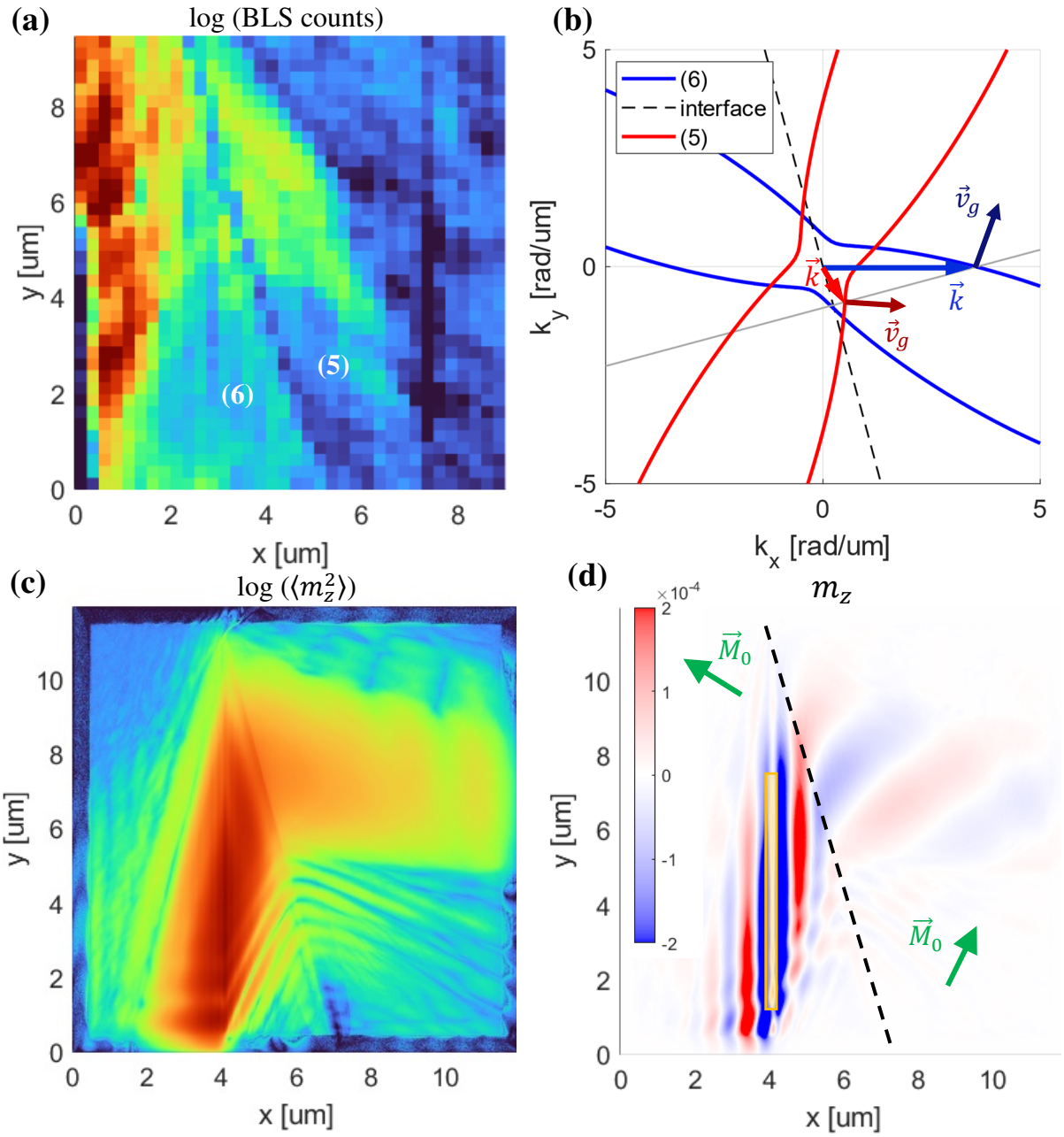

Fig.5.3: **(a)** 2D-BLS scan of the area outlined by the red rectangle in Fig.5.2 (a). The excitation frequency was 3.75 GHz, and the detection was performed in a short interval of frequencies around that. A minimum of the spin-wave intensity can be observed at the interface. **(b)** Isofrequency lines calculated using (1.68) and the magnetic properties found in section 3.2. Interface is outlined by the dashed line. Wave vector transforms during the refraction only in the component perpendicular to the interface to match the dispersion behind the interface. **(c)** Result of simulation illustrating the refraction. The magnetization response of m_z was squared and averaged through time to correspond to the BLS data. **(d)** Snapshot of the response of m_z from the same simulation. Dashed line shows the interface.

Measurement of the refraction was performed over the area designated by the red rectangle in Fig.5.2 (a), in which the BLS laser spot was scanned with a 0.25 μm step. The magnons were detected in a short interval of frequencies around the excitation frequency and the result

summed over this interval is shown in Fig.5.3 (a). Position of the excitation antenna can be recognized by the lower intensity in the bottom-left corner.

In Fig.5.3 (b) we plot the isofrequency lines of spin waves before (blue) and behind (red) the interface, which were obtained using (1.68) and the magnetic properties found in section 3.2. The antenna excites waves with phase changing purely in the *x*-direction, that is, the blue wave vector. As was described in subsection 1.3.3 – during refraction, the wave vector component parallel to the interface is preserved and the perpendicular component changes to match the dispersion behind the interface. In Fig.5.3 (b) we outline direction of the interface by the dashed line and the set of allowed refracted wave vectors by the solid gray line. It is obvious from the geometry that the wave vector transforms into the red one displayed in Fig.5.3 (b). Group velocity is given by $\partial\omega/\partial\vec{k}$ (1.71), which follows the direction of steepest incline of the dispersion relation, that is perpendicular to the isofrequency line. Therefore, it is to be expected that the initial wave packet propagates in the top-right direction and the refracted wave approximatelly to the right. In the measured data presented in Fig.5.3 (a) we observe the predicted propagation direction before the interface, but behind the interface the direction is more downward than expected. This could be caused either by the inhomogeneity visible in Fig.5.2 (a) or by another incident wave, which originates in the wider part of the antenna that is necessary to connect the dynamic currect to the desired slim strip constituting the intended excitation antenna.

We have also performed micromagnetic simulation to illustrate the refraction. The wave was excited at the position outlined by the yellow rectangle with a gaussian profile in Fig.5.3 (d) (to remove any artifacts caused by the sharp edges, which would be present if it was excited simply in a rectangular area). The simulation was run for 10 nanoseconds to get in the steady state and then the response of magnetization was saved over one period. One snapshot of this response is displayed in Fig.5.3 (d), where we see the spin wave propagate in the top right direction with the wave vector purely in the *x*-direction before the interface. Behind the interface the wave propagates approximately to the right with the phase changing in the down-right direction, which agrees well with Fig.5.3 (b). In Fig.5.3 (c) we show the response squared and averaged through time to see a quantity that is proportional to the signal detected in the BLS measurement. (We also see certain artifacts caused by reflection of waves from the sides of simulation with higher damping.) Altogether, the situation presented in the simulation shows what we would expect in a clearer structure with a more definite excitation that would have the magnetic properties measured in section 3.2.

5.2 Refraction from domain (5) to domain (6)

This section covers another measurement of refraction, this time the incident wave was excited in the domain (5) approximately as the Damon-Eshbach mode and refracted on an interface with domain (6). This measurement was located in the top-right corner of the bottom transformed rectangle shown in Fig.5.1 (a). Geometry of this experiment is displayed on a (tilted) SEM image with design of the antennas for the EBL process in Fig.5.4 (a). Measurements similar to those presented in Fig.5.2 were done and we have decided to use the frequency 4 GHz for this structure. The 2D-BLS measurement was performed over the area outlined by the red rectangle and its result is shown in Fig.5.4 (c).

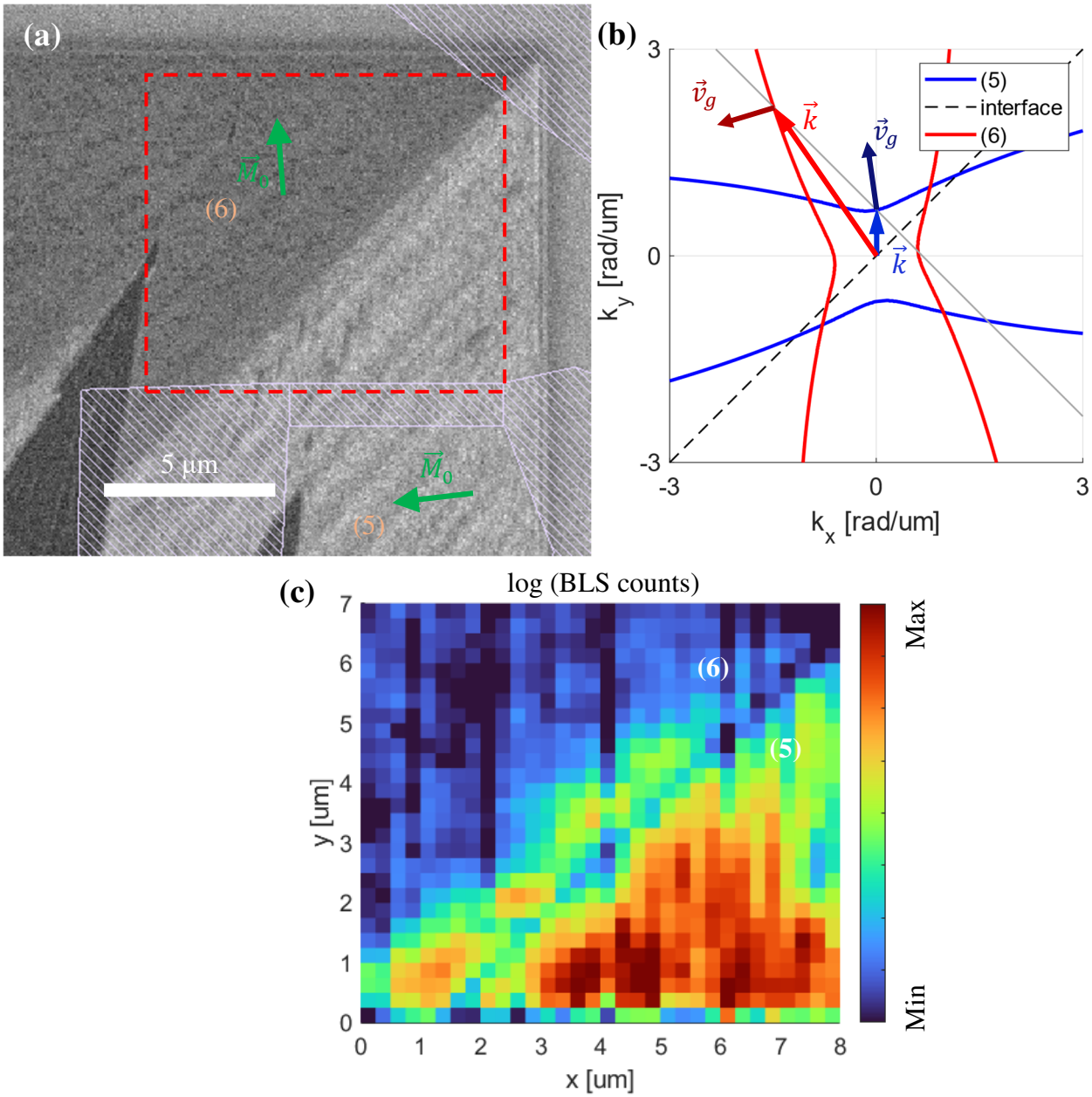

Fig.5.4: **(a)** Tilted (4°) SEM image of the area for refraction from domain (5) to (6) with the design sketch for the excitation antenna. No external field was applied, and the magnetization is oriented along the easy axes found in section 3.2. Red rectangle shows the position of the 2D-BLS measurement of the refracting waves. **(b)** Isofrequency lines calculated using (1.68) and the magnetic properties found in section 3.2. Interface is outlined by the dashed line. Refraction of an approximately Damon-Eshbach mode into a mode with its wave vector misaligned from the local magnetization by approx. 50° is expected. **(c)** 2D-BLS scan of the area outlined by the red rectangle in Fig.5.4 (a). The excitation frequency was 4 GHz, and the detection was performed in a short interval of frequencies around that. A minimum of the spin-wave intensity can be observed at the interface.

We also show the isofrequency lines computed [using (1.68) and the magnetic properties from section 3.2] for this experiment in Fig.5.4 (b). The excited mode in domain (5) is approximately of the Damon-Eshbach type and the refracted mode has its wave vector angled from the magnetization in domain (6) by approximately 50°. Consequently, the excited wave packet should travel from the antenna quite perpendicularly, and the refracted wave's group velocity should be oriented in the left-bottom direction ca. 20 or 30 degrees from the interface. Spatial evolution of the spin-wave intensity observed in the measured data [Fig.5.4 (c)] approximately agrees with these group velocity directions. However, the measured intensity is not very homogeneous. The vertical lines of lower intensity were likely caused by instability of the spectrometer in BLS (mirrors in the tandem Fabry-Perot interferometer are automatically and continuously being aligned during the measurement, but some disruptions can cause lower transmission efficiency for a while). In the domain (5), the observed intensity is result of interference of the excited and reflected waves. Additional inhomogeneities could be caused by imperfections of the transformed crystal but comparing the SEM images of this structure [Fig.5.4 (a)] and the previous structure [Fig.5.2 (a)] suggests that this should be a smaller concern here.

5.3 Refraction from domain (6) to domain (alp)

In this section, an attempt to measure refraction from domain (6) to domain (alp) is presented. The excited wave is ca. of the Damon-Eshbach mode and propagates towards the interface, along which a small region of the domain type (5) is situated, as can be seen on the SEM image with design for the antennas in Fig.5.5 (a). This measured structure is located in the top-left corner of the bottom transformed area in Fig. 5.1. As in previous measurements, we first present the outline of the experiment on the SEM image in Fig.5.5 (a).

The working frequency was again chosen to be 4 GHz. The 2D-intensity map measured by the BLS is displayed in Fig.5.5 (c). No spin waves were observed behind the interface, which should be expected given the magnetic properties of the (alp) domain measured in section 3.2. In that section, we have found that the saturation magnetization of this domain type is less than half compared to magnetization in the conventional domains [(6), (5), …] and the anisotropy is also much weaker. Consequently, the magnon frequencies will be significantly lower than in the conventional domains, or expressed in more relevant terms, the wave vectors on a given frequency will be much higher in the (alp) domain. This feature is shown in Fig.5.5 (b) for the working frequency 4 GHz. Again, the isofrequency lines were computed by equation (1.68), which was modified along (3.3) in the (alp) domain, and the magnetic properties found in section 3.2. Naturally, the big mode-mismatch will result in low transmission. And second reason, why we observe no waves in the (alp) in this measurement, is that the wave would have a wave vector at or beyond the limit of BLS detectivity, which is optimally 18 rad/μm. It should be noted that we did not measure the exchange constant, which will probably also be lower in the (alp) domain given its lower overall qualities and inhomogeneity. This would shift the frequencies at higher wave vectors even lower, or in other terms, to reach a given frequency the wave vector would have to be bigger. This would further enlarge the isofrequency line and would lead to a more certain undetectability.

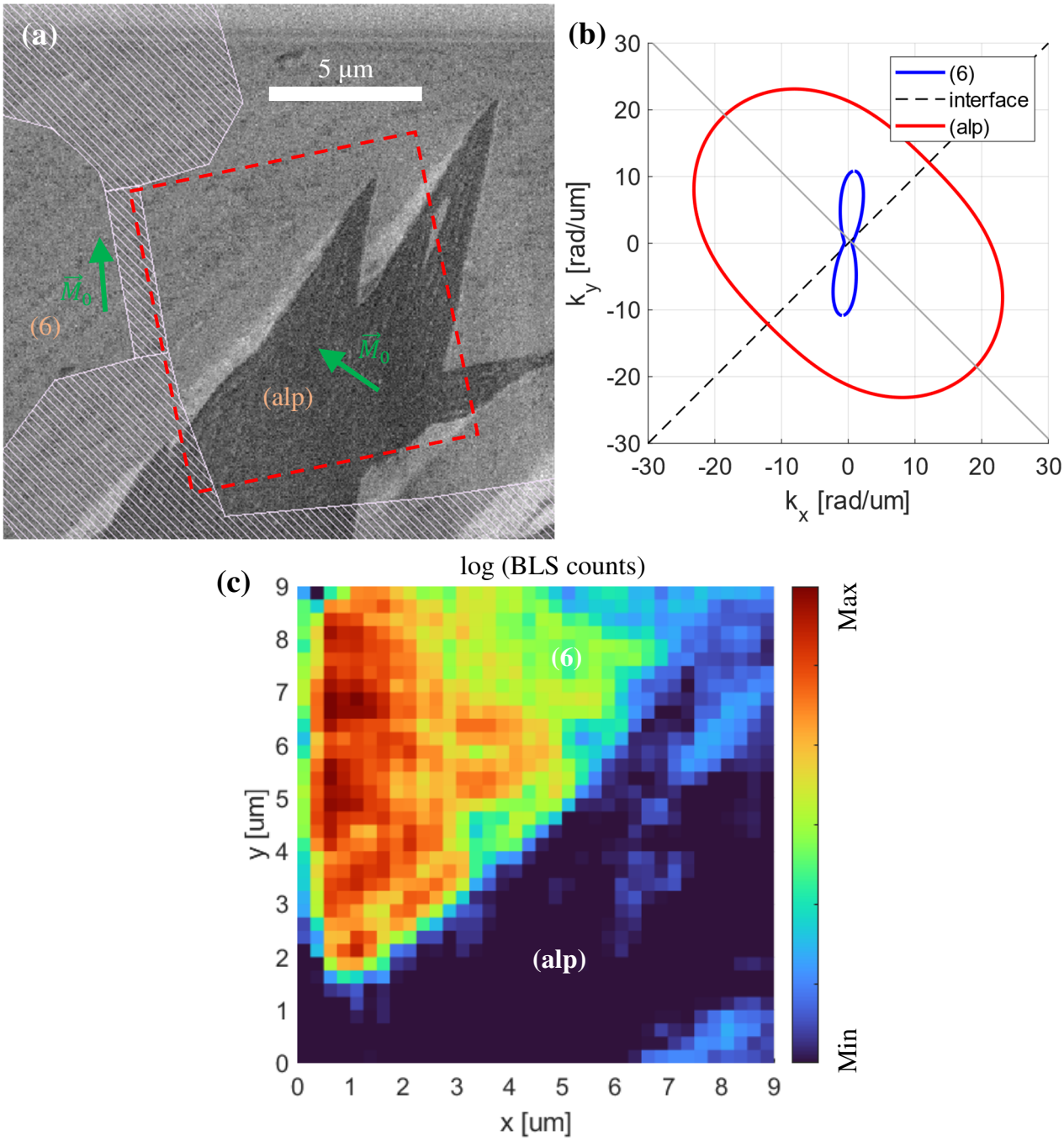

Fig.5.5: **(a)** Tilted (4°) SEM image of the area for refraction from domain (6) to (alp) with the design sketch for the excitation antenna. No external field was applied, and the magnetization is oriented along the easy axes found in section 3.2. **(b)** Isofrequency lines calculated using (1.68) [in (alp) modified along (3.3)] and the magnetic properties found in section 3.2. The exchange constant is likely lower than what we have used for the (alp) domain's isofrequency line and the wave vectors are likely even larger. Interface is outlined by the dashed line. Wave vector of the mode in the (alp) domain is very large, probably undetectable by our BLS setup. The big mode-mismatch could also lower the transmission efficiency. **(c)** 2D-BLS scan of the area outlined by the red rectangle in Fig.5.5 (a). The excitation frequency was 4 GHz, and the detection was performed in a short interval of frequencies around that. No spin waves were observed in the (alp) domain.

6 Turning of spin waves

This chapter is dedicated to our investigation of the possibilities to turn spin waves in waveguides with locally varying direction of anisotropy. First, we present micromagnetic simulations of two different designs of turned waveguides – one with transversal orientation of anisotropy and one with a more complex anisotropy landscape, which assures preservation of the spin wave mode with regards to the local dispersion relation. Then, Brillouin light scattering measurements of these two designs, which were experimentally realized in the wavy waveguide system, are shown and their advantages are discussed.

6.1 Simulations of alternative turn designs

In this section, we describe our micromagnetic simulations (introduced in section 2.4) of two different designs of turned spin-wave waveguides and compare their qualities. These designs are based on spatial variation of the direction of uniaxial anisotropy, which can be experimentally realized in our wavy waveguide system.

The first design is very similar to the turned spin-wave waveguide created by the authors of [37], which was presented back in Fig.1.8 (d) together with its advantages over a uniformly magnetized turn. They have magnetized the turned waveguide transversally by a nonuniform external magnetic field that was induced by current flowing in an underlying conducting strip. Our first design is based on their structure, but the magnetization is forced to be aligned transversally in every part of the waveguide by a changing anisotropy direction. Our second (more complicated) design is intended to work with waves that have their wave vector misoriented by approximately 60° from the Damon-Eshbach (DE) mode and the anisotropy is tilted from the transversal direction in such a way that the group velocity is parallel to the waveguide. Then, in the turn, the waveguide consists of several domains with different constant anisotropy directions and specific angles of the interfaces between the domains, which assures that the turned (refracted) wave stays in the same mode as the incoming wave. In other words, this design is intended to provide phase-coherent turning, but it also provides a superior turning of the real-space spin-wave wave packet. Versions with gradually changing anisotropy directions and with discrete domains of constant anisotropy direction offer practically the same turning qualities (as will be shown later) and we will first deal with the discrete case.

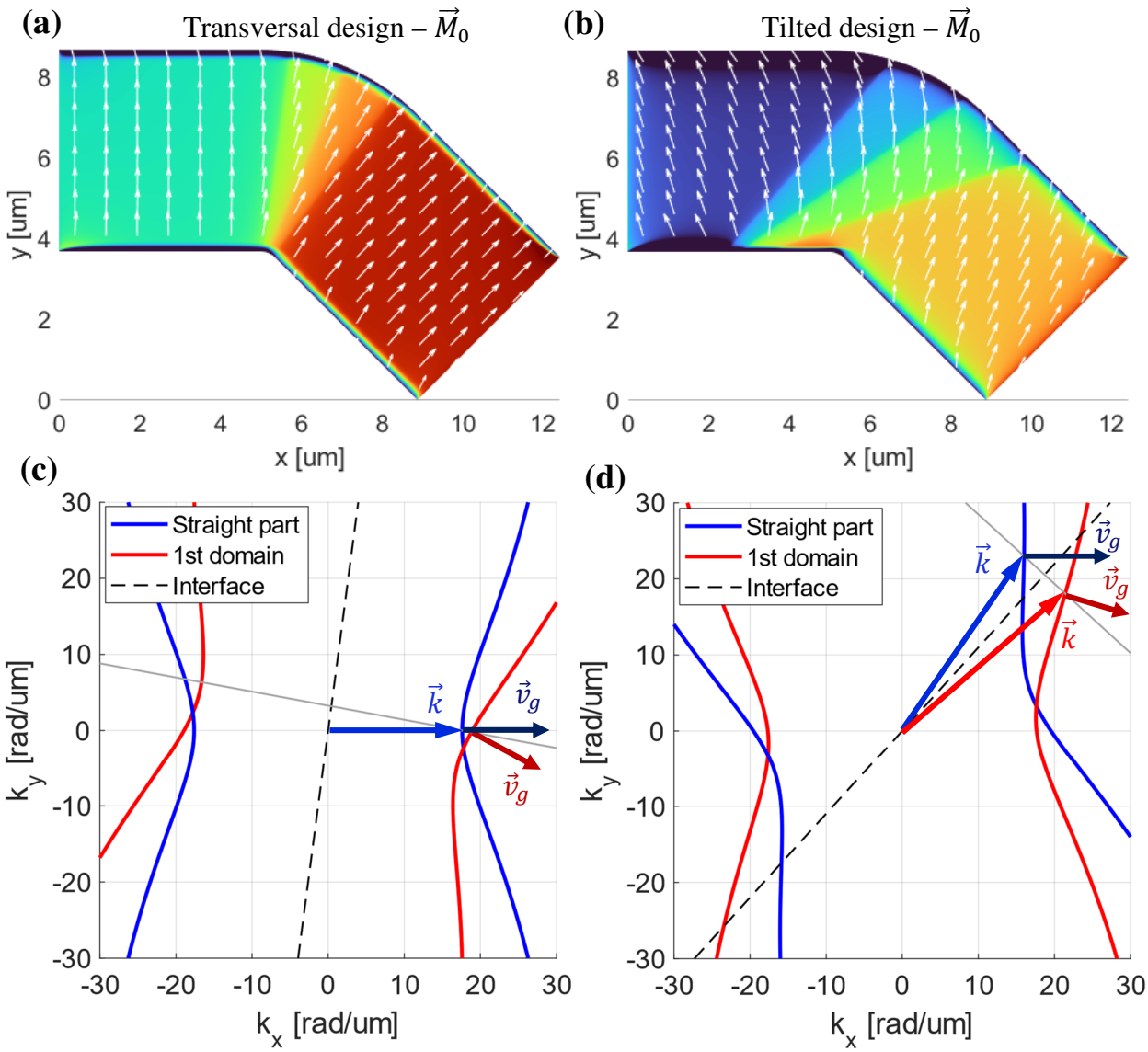

Fig.6.1: **(a)** Magnetization ground state of our first (transversal) design obtained from simulation. The magnetization is forced to be transversal to the local waveguide direction by uniaxial anisotropy of changing direction. **(b)** Magnetization ground state of our second (tilted) design obtained from simulation with the same parameters as (a) but a different spatial distribution of the anisotropy direction. **(c)** Isofrequency lines of the straight part and the first domain of the turn in (a), computed using (1.68) and parameters of the simulation. The dashed line shows direction of the interface between the two regions and the gray solid line is perpendicular to it, showing the set of allowed refracted wave vectors. This design works initially with the DE mode (in experiment excited by an antenna placed perpendicularly to the waveguide) but due to the geometry, the refracted wave is shifted on the isofrequency line in the positive k_y-direction. Given the anisotropic nature of the dispersion relation, this leads to the group velocities before and behind the interface forming an angle larger than the angle of anisotropy-direction difference, which leads to the over-turning seen in Fig.6.2 (a). **(d)** Analogy of (c) but for the tilted design presented in (b). The working point is tilted from the DE mode by approx. 60° and the waveguide is designed to refract the wave into the same mode with respect to the local dispersion.

Both (discrete versions of the) designs are outlined in Fig.6.1 (a) and (b) by their equilibrium magnetization directions obtained from simulations[1]. The angle of anisotropy changes with a 15 degrees step in both cases. In most of the waveguide's area the magnetization is parallel to the anisotropy direction, but at the edges the magnetization aligns more parallelly to the borders of the magnetic body due to the demagnetizing energy. The inner turn radius could be increased (and waveguide width decreased) to get rid of the "wild" configuration near the inner part of the turn in Fig.6.1 (b).

Basis of the wave turning is refraction at the several interfaces and the turning characteristics can be revealed by inspection of refraction on just one interface. In Fig.6.1 (c) and (d), we show isofrequency lines in the straight part of the waveguides and in the first domains of the turns along with the interface direction between these two regions. In the transversal design of turned waveguide, the initial wave is excited by an antenna perpendicular to the straight part of the waveguide, that is, in the DE mode. As is graphically explained in Fig.6.1 (c), the wave then refracts on the interfaces into modes, that are shifted along the k_y-direction in the local dispersion. This causes a loss of phase coherency and over-turning of the group velocity (which is perpendicular to the isofrequency line). The tilted design works with a mode, whose wave vector is tilted from the DE geometry by approx. 60°, which is realized in the experiments by placing the antenna under an angle to the longitudinal direction of the waveguide. In order to secure refraction into the same mode, the interface is chosen to be tilted by half of the domain angle-step from the wave vector direction. This achieves preservation of the phase coherence and the group velocity direction leading to better turning qualities as can be seen in Fig.6.2. It is obvious from Fig.6.1 (c) that this design-approach cannot be used on waveguides operating with the DE mode, because the interfaces would be practically parallel to the propagation direction.

We have simulated spin wave propagation in the two turned waveguides presented in Fig.6.1. The waves were excited with a gaussian profile so that we are able to trace the wave inside the waveguide (and to remove some undesired distracting effects at the waveguide's borders). The simulations were run for 6 ns to get in the steady state and then the magnetization was saved. The z-component of magnetization m_z displayed in Fig.6.2 (a) and (b) shows the spin waves. We observe behavior predicted in the previous paragraph – the wave in the waveguide of transversal design over-turns and the mode transforms from the DE mode to some different mode. This is clearly confirmed in Fig.6.2 (c), which shows the two-dimensional (discrete) Fourier transforms of m_z in the regions before and behind the turn. The turning properties of the tilted design are much better as can be seen in Fig.6.2 (b) – the group velocities are aligned along the waveguide everywhere and the mode before and behind the turn stays the same, as is confirmed by the 2D-Fourier transformations [Fig.6.2 (d)].

[1] We have simulated 12.4 μm by 8.7 μm area containing the 9 nm thick and 5 μm wide waveguide with magnetic parameters $M_S = 1.41$ MA/m, $\gamma = 2\pi \cdot 29.3 \cdot 10^9$ rad/Ts, $A_{\mathrm{ex}} = 11$ pJ/m, $\alpha = 0.0005$ (to focus our attention on the turning qualities) and $K_{\mathrm{u}} = 22$ kJ/m^3. (These simulations were performed before the experimental part of this thesis and we have chosen these parameters according to [57].) The outer radius of the turn was 5.5 μm. The number of cells was $4096 \times 4096 \times 1$ and no PBCs were used. The spin wave was excited in the straight part of the waveguide with a gaussian profile at the frequency 15 GHz (having a higher frequency and therefore also the wave vector makes the simulation more readable). The magnetization was first saved in the equilibrium configuration for Fig.6.1 (a) and (b) and then for the spin wave in the steady state (after 6 ns). 1 μm long damping regions were placed in the beginning and end of the waveguide.

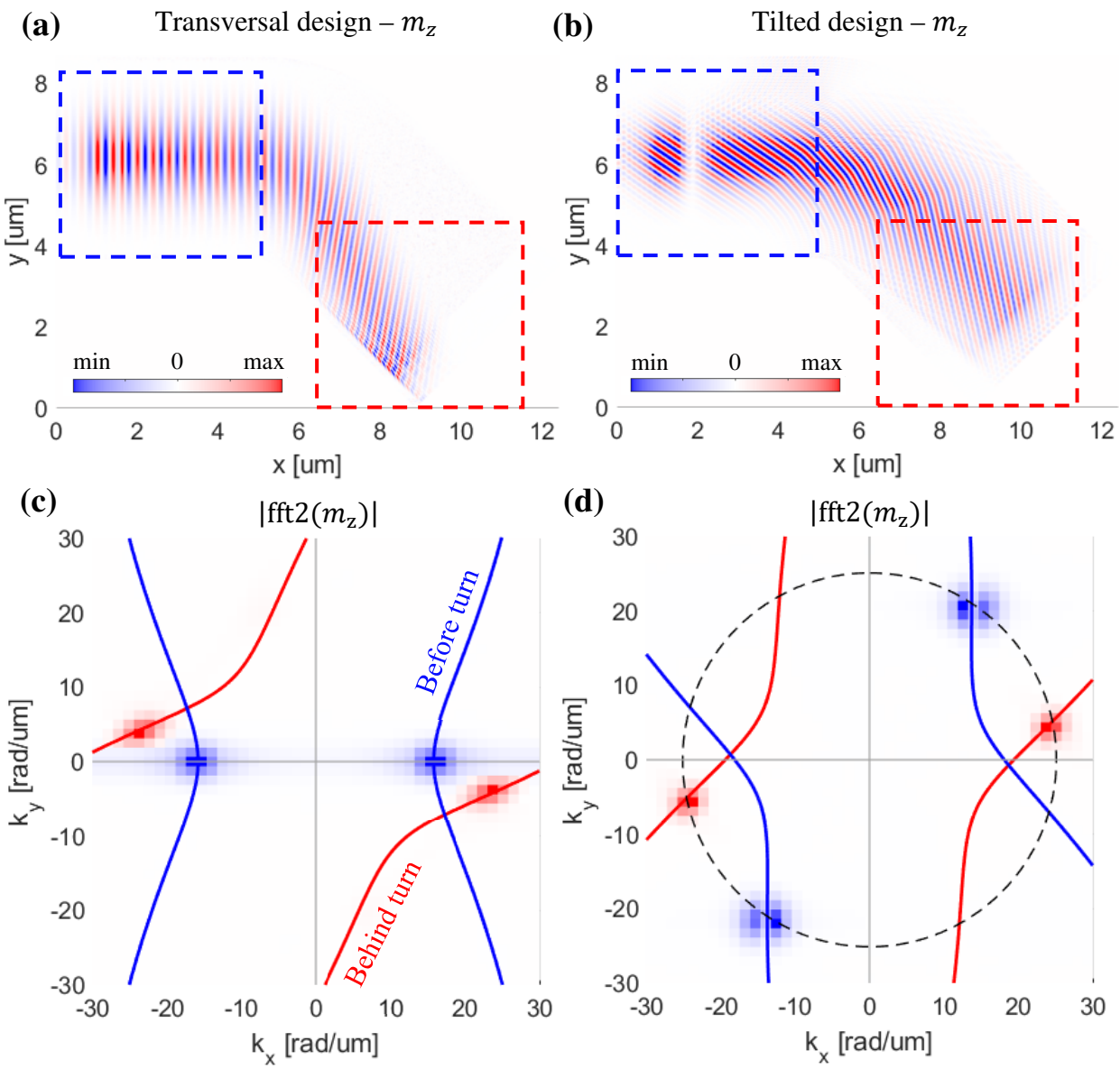

Fig.6.2: **(a)** Simulation of spin waves in the waveguide of transversal design in Fig.6.1 (a). m_z component of magnetization shows the spin wave in the steady state (after running the simulation for 6 ns). The wave was excited in the top-left straight region with a gaussian profile on the frequency 15 GHz. Over-turning of the wave in the turn can be observed, which was graphically explained in Fig.6.1 (c). **(b)** Spin wave in the waveguide of tilted design, no over-turning is observed. **(c)** Normalized magnitude of the two-dimensional (discrete) Fourier transformations of the magnetization response in the rectangular regions from (a). Blue color belongs to the region before the turn and red to the region behind the turn. The isofrequency lines were computed using (1.68) and parameters of the simulation. The DE mode transforms into a different mode during propagation through the turn. **(d)** Analogy of (c) but for the tilted design presented in (b). The spin wave stays in the same mode. The dashed circle provides a guide for demonstration of the mode-preservation.

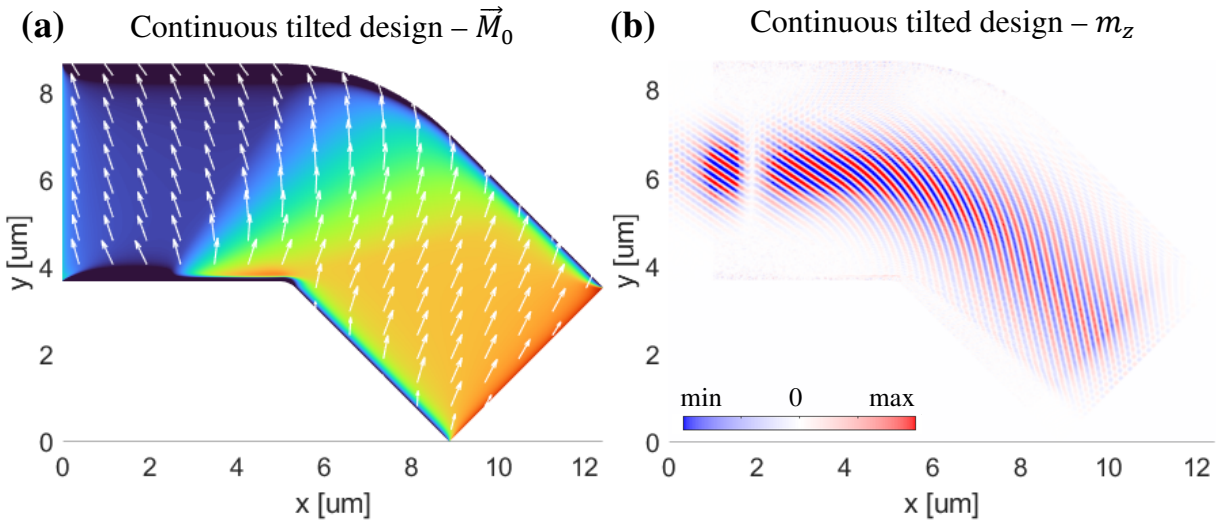

Fig.6.3: **(a)** Magnetization ground state of the tilted design in its continuous version (obtained from simulation). **(b)** Spin wave in the waveguide from (a). There exists only a small difference in the spin wave propagation compared to the discrete version – in the turn the wave transforms gradually instead of refracting on individual interfaces as in Fig.6.2 (b). The important qualities are the same. The same is true for the discrete and continuous versions of the transversal design (not shown).

We have also performed simulations of spin wave propagation in continuous versions of these designs. An example of this is displayed in Fig.6.3 for the tilted design. Comparing the m_z response in the steady state between the discrete [Fig.6.2 (b)] and continuous [Fig.6.3 (b)] versions reveals only negligible differences. Lastly, we have run a simulation with an excitation on a wider range of frequencies and we have observed (not shown) similar propagation path for an interval $9 - 19$ GHz, which should not be surprising given the dispersion in Fig.1.4 (b).

6.2 Wavy waveguide turns of transversal design

This section covers our measurements of spin waves propagating through turned wavy waveguides of the transversal design. The waveguides and excitation antennas were fabricated using the focused electron beam induced deposition, electron beam lithography and the evaporator, as was described in section 4.1. Typical outline of these measurements is presented in Fig.6.4 together with an atomic force microscopy image of the corrugation in the turn.

We have consecutively fabricated three generations of turned wavy waveguides. In the first generation, waveguides of width 4 μm and 2.5 μm were created on corrugated areas of width 6 μm and 4 μm. In the narrower waveguides, the geometrically induced anisotropy was not strong enough to overcome the (overall) shape anisotropy (which was seen by short decay lengths in the 2D-BLS maps) and we have not used them any further. In the second and third generations, which have used the same FEBID-controlling file, we have placed the excitation antennas farther away from the turns and we have introduced the proper "tilted design" [shown later in Fig.6.8 (a)]. We have used low (20 kV) acceleration voltage during the FEBID process when fabricating the second generation, consequently height of the corrugation was low, and the geometrically induced anisotropy was weak. (Comparison of the anisotropy of the 2nd and 3rd generations was made in Fig.4.8.) The third generation was prepared using the proper parameters with the help from Igor Turčan, who has performed most of the fabrication steps.

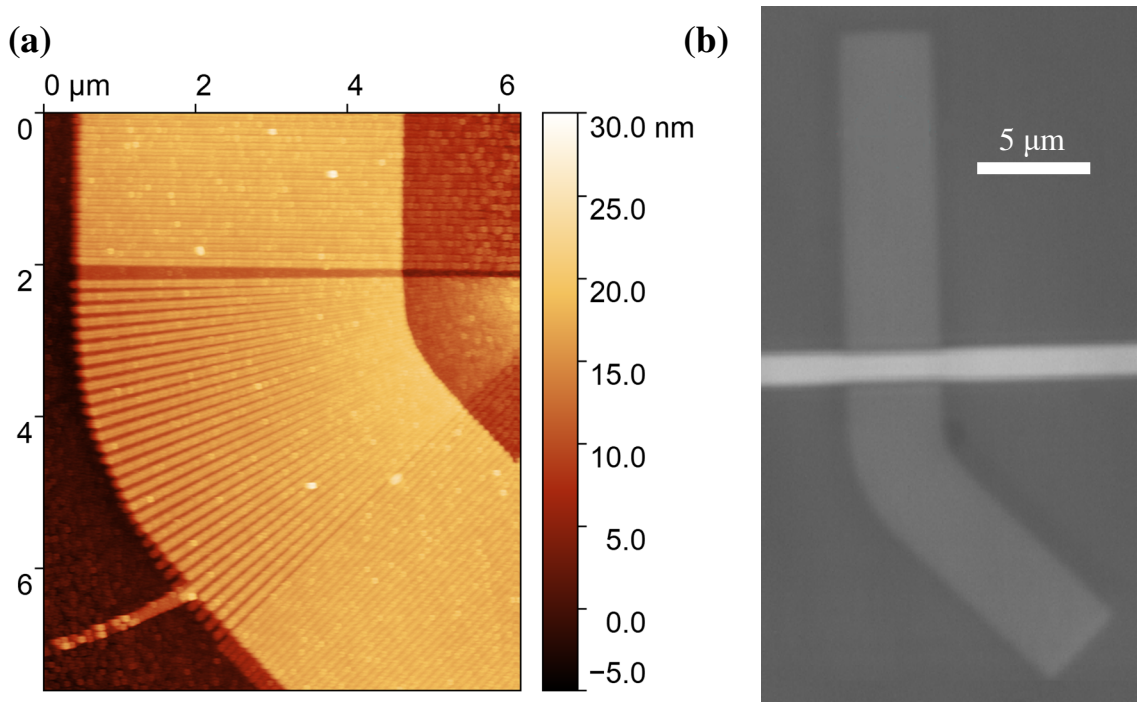

Fig.6.4: **(a)** Atomic force microscopy image of a turned waveguide of the transversal design (belonging to the first generation, created by 7000 FEBID scans). Three types of areas are visible – substrate (lowest), FEBID-grown corrugation (medium height) and corrugation with a permalloy layer on top of it (the waveguide itself, highest). Sometimes during the FEBID procedure, the beam gets misaligned when driving to new locations and imperfections like the one near 2 µm (vertical) get created. Measured by Igor Turčan. **(b)** Light microscope image of the turned waveguide prepared for a BLS measurement. The antenna (white strip) is perpendicular to the transversally magnetized waveguide to excite the DE mode.

In BLS measurements of the turned waveguides, we typically begin by inspection of the thermal magnon spectra before, in and behind the turn to see whether the magnon frequencies match. A high frequency mismatch would indicate big differences in the dispersion relations and consequently the incoming spin wave would have to convert to a very different mode, which would lead to stronger reflection rather than passing through the turn. However, this is not the case with most of our waveguides of the transversal design. Usually, we measure the magnon spectra only at the three specific locations, but here we present [in Fig.6.5 (c) and (d)] only a more comprehensive measurement, in which the spectra were measured along lines of changing radius (c) and changing angle (d) in the turn.

Typically, as the next step, we look for frequencies at which the spin waves pass through the turn with the highest intensity. This is done by focusing the BLS laser spot at a location behind the turn and changing the excitation frequency, as is shown in Fig.6.5 (b).

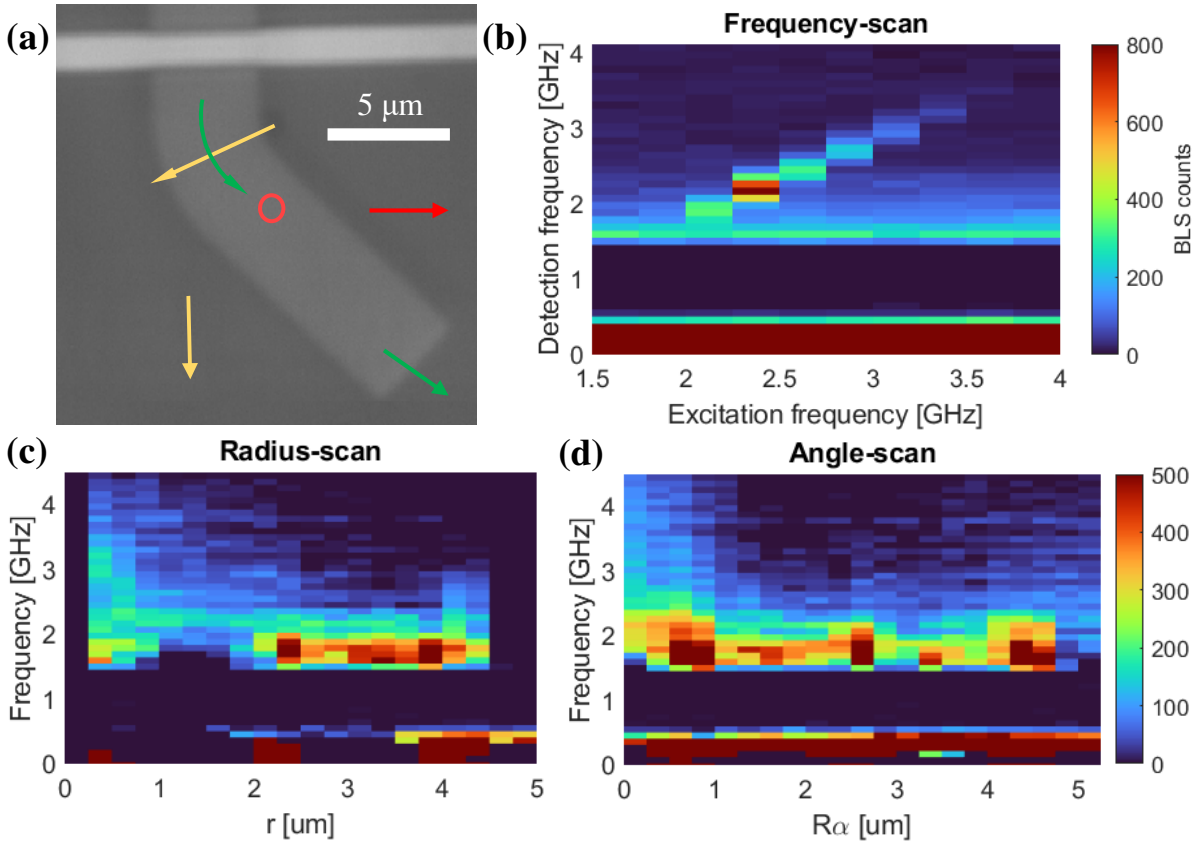

Fig.6.5: **(a)** Light microscope image of the turned waveguide with outlined positions of the three measurements. **(b)** BLS measurement with the laser focused at the red circle in (a). The excitation frequency was swept to find a good propagation frequency, in this case 2.25 GHz was chosen for the 2D intensity map shown in Fig.6.6 (c). **(c)** Thermal magnon spectra measured by BLS at different radii in the turn [along the yellow line in (a)] of the same structure as in (b). The first position was still outside the magnetic waveguide, and we have used it to subtract the laser mode in (c) and (d) (which was visible in many previous figures), which would otherwise obfuscate the data. The frequency is only slightly higher at lower radii, but at the edge it drops again, likely due to the character of edge-modes [57] and due to fusion of the corrugations [which can be seen in Fig.6.4 (a)]. **(d)** Thermal magnon spectra measured at different angles inside the turn [along the green line in (a)]. The frequencies stay approximately the same (especially when compared to measurements of the tilted designs presented later). The small frequency decrease in the turn with respect to the straight parts does not prevent spin wave propagation but likely causes some reflection.

We have performed measurements similar to those shown in Fig.6.5 in several turned waveguides of the transversal design, the frequencies in different location approximately matched, and we have chosen the appropriate excitation frequencies. Two dimensional BLS scans of several of those structures are presented in Fig.6.6. However, anisotropy in waveguides of the second generation was weak (as was discussed earlier), consequently the magnetization could not be kept transversal in every part of the waveguide and the spin waves reflected on some domain wall in the turn, which separated domains of significantly different dispersions (we do not display the corresponding data, it looked similar to the unsuccessful waveguides shown in the next section).

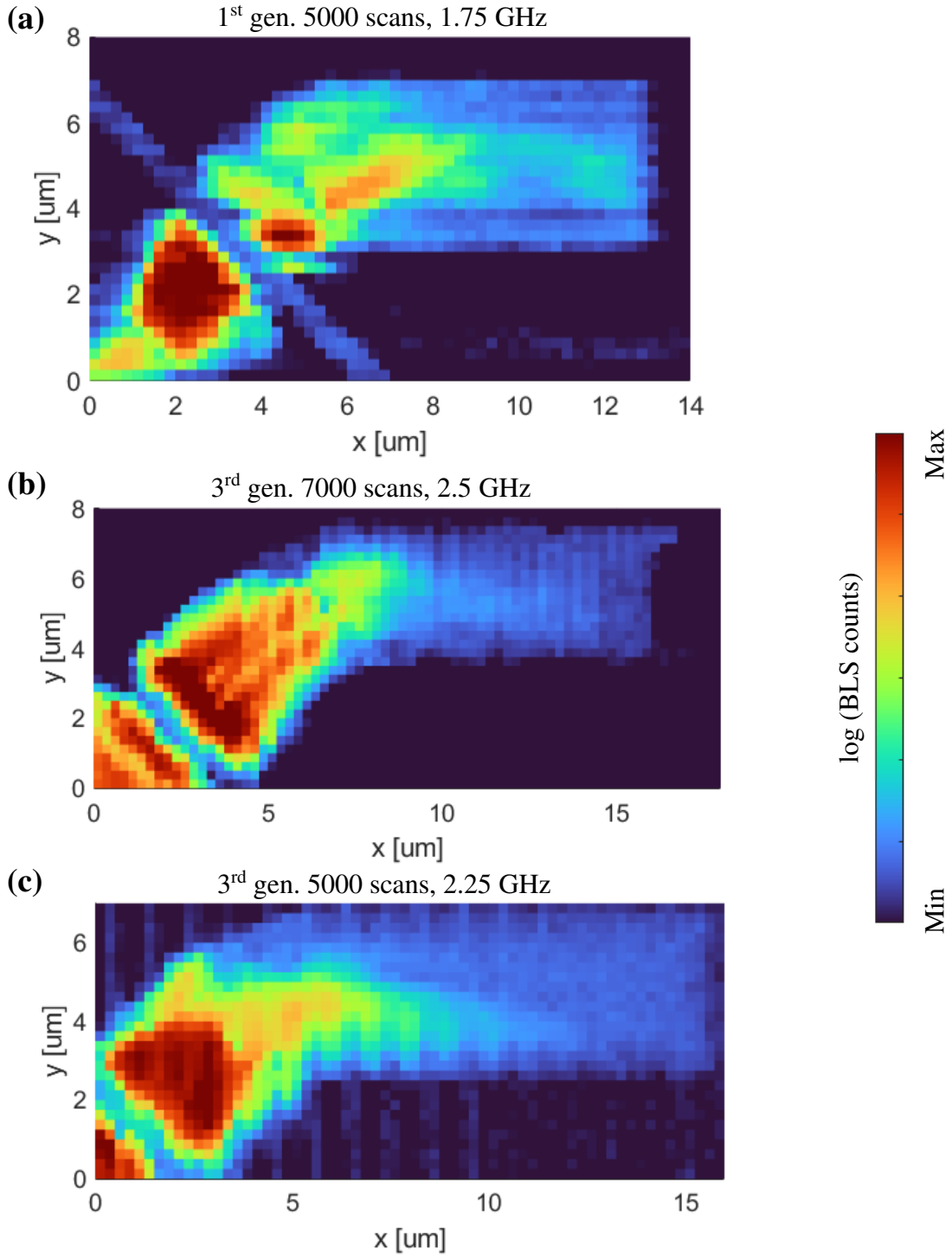

Fig.6.6: **(a)** Two dimensional BLS measurement of spin wave intensity in a waveguide of the transversal design, which was created using 5000 FEBID-scans in the first generation. The antenna excited spin waves at the frequency 1.75 GHz. **(b)** Spin wave intensity at 2.5 GHz in a waveguide of the third generation created by 7000 scans. **(c)** Spin wave intensity at 2.25 GHz in a waveguide of the third generation created by 5000 scans. The slight vertical lines in the measured data were likely caused by instability of the BLS setup.

We can see in Fig.6.6 that the waves typically partially reflect at the beginning of the turns. In some of the waveguides [(a) and (b)] this is accompanied by a short reduction of the spin wave intensity, which we have also observed during refraction between domains with different anisotropy directions in chapter 5 and a similar pattern was reported for spin wave propagation through a domain wall [67]. The cleanest propagation was shown in Fig.6.6 (c), where we even see the over-turning of the wave, which was predicted by the simulations in section 6.1.

Furthermore, we have also measured the straight sides of the waveguides to have a reference for the turns. In Fig.6.7 we present the cleanest measurement from Fig.6.6 along with measurement of its straight part, which was performed while using the same experimental parameters (such as the excitation frequency and the BLS detection frequency interval). We have integrated the measured signal along the transversal direction of the waveguide to obtain a streamlined comparison of the two measurements, as is shown in Fig.6.7 (c). It is apparent that the biggest loss of wave intensity propagating in the turned waveguide occurs just before the beginning of the turn. This could be suggested even from looking at the 2D intensity maps in Fig.6.6 (b) and (c). The small downward frequency shift of the magnon spectra in the turn [shown in Fig.6.5 (d)] should be reminded here. Moreover, the intensity decays faster behind the turn than in the straight waveguide because of the over-turning.

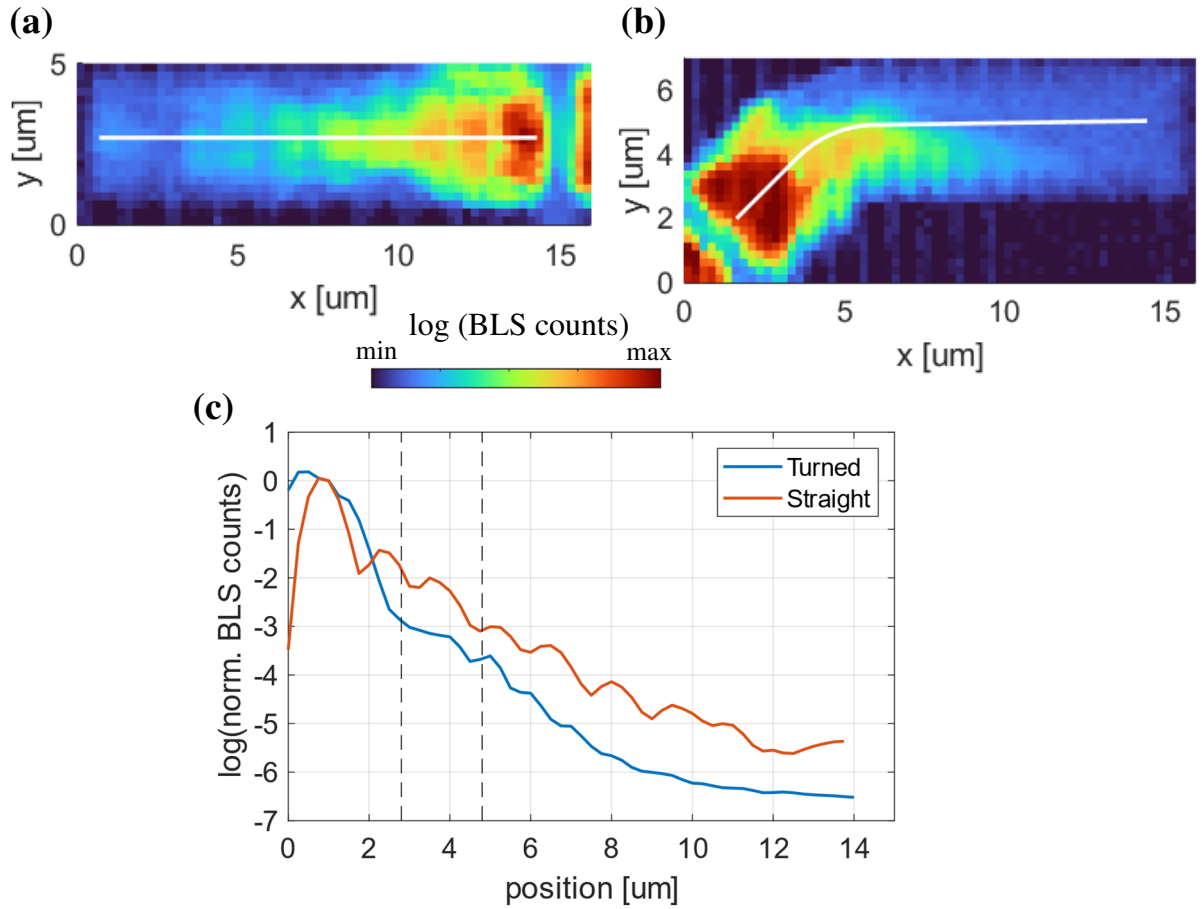

Fig.6.7: **(a)** 2D BLS measurement of the straight part of the same waveguide as (b). The excitation frequency was 2.25 GHz. **(b)** The same BLS measurement as in Fig.6.6 (c). Same parameters were used for this turned and the straight waveguide's measurements. **(c)** Spin wave intensity, which was integrated along the transversal direction of the waveguide. The intensity was normalized approximately 1 μm from the antenna. The dashed lines outline the turn's region.

6.3 Wavy waveguide turns of tilted design

In this section we present our measurements of spin wave propagation in turned waveguides of the tilted design. These structures were prepared together with the ones of transversal designs in the same FEBID and EBL sessions. Geometry of these corrugated turned waveguides and their experimental setup are shown in Fig.6.8. We have decided to work with the mode tilted in the other direction with regards to the turn than in the simulations to obtain more space for the excitation antenna, the working mechanism remains the same.

We began by investigating the thermal spectra at different parts of the waveguide for reasons outlined in the previous section. The thermal magnon spectra measured a few micrometers before and behind the turn exhibit large frequency differences as can be seen in Fig.6.9 (b). This should be directly unrelated to the to the magnetization order inside the turn given the location of these measurements, and we suspect it to be a result of inhomogeneity of the corrugation height – the electron beam in the FEBID procedure might have been astigmatic and ridges created in different directions would be differently blurred. This alone predicts worse turning qualities. Moreover, performing the measurements of thermal magnons along two distinct lines inside the turn suggested presence of a complicated magnetic order. The measurements at different radii in the turn are shown in Fig.6.9 (c) and at different angles in the turn in Fig.6.9 (d). The complicated spatial evolution of the magnon spectra is likely caused by different qualities of the individual domains [which are visible in Fig.6.8 (a)], by formation of domain walls and by possible discontinuities in the corrugation. We would expect spin waves to propagate through these areas very poorly, which we also observed in later experiments.

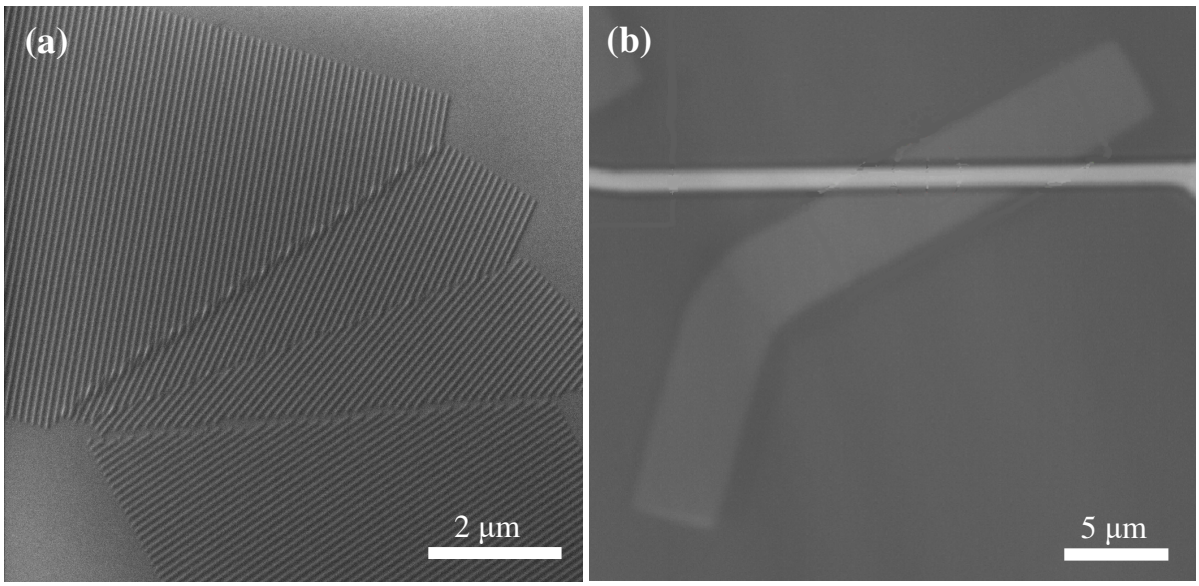

Fig.6.8: **(a)** SEM image of corrugation of the substrate for a turned waveguide of the tilted design. This image shows the state of the sample just after the FEBID. The magnetic material was later deposited in the normal smooth shape. Contrast is achieved due to the secondary-electron detector being in a certain direction from the measured area. **(b)** Light microscope image of the turned waveguide prepared for a BLS measurement. The antenna (white strip) and the waveguide form an angle equal to the sum of the angle of the chosen mode with respect to the DE mode and of the angle of group velocity this mode would have with respect to the DE mode's group velocity (that is equal to the designed tilt of magnetization from the transversal direction).

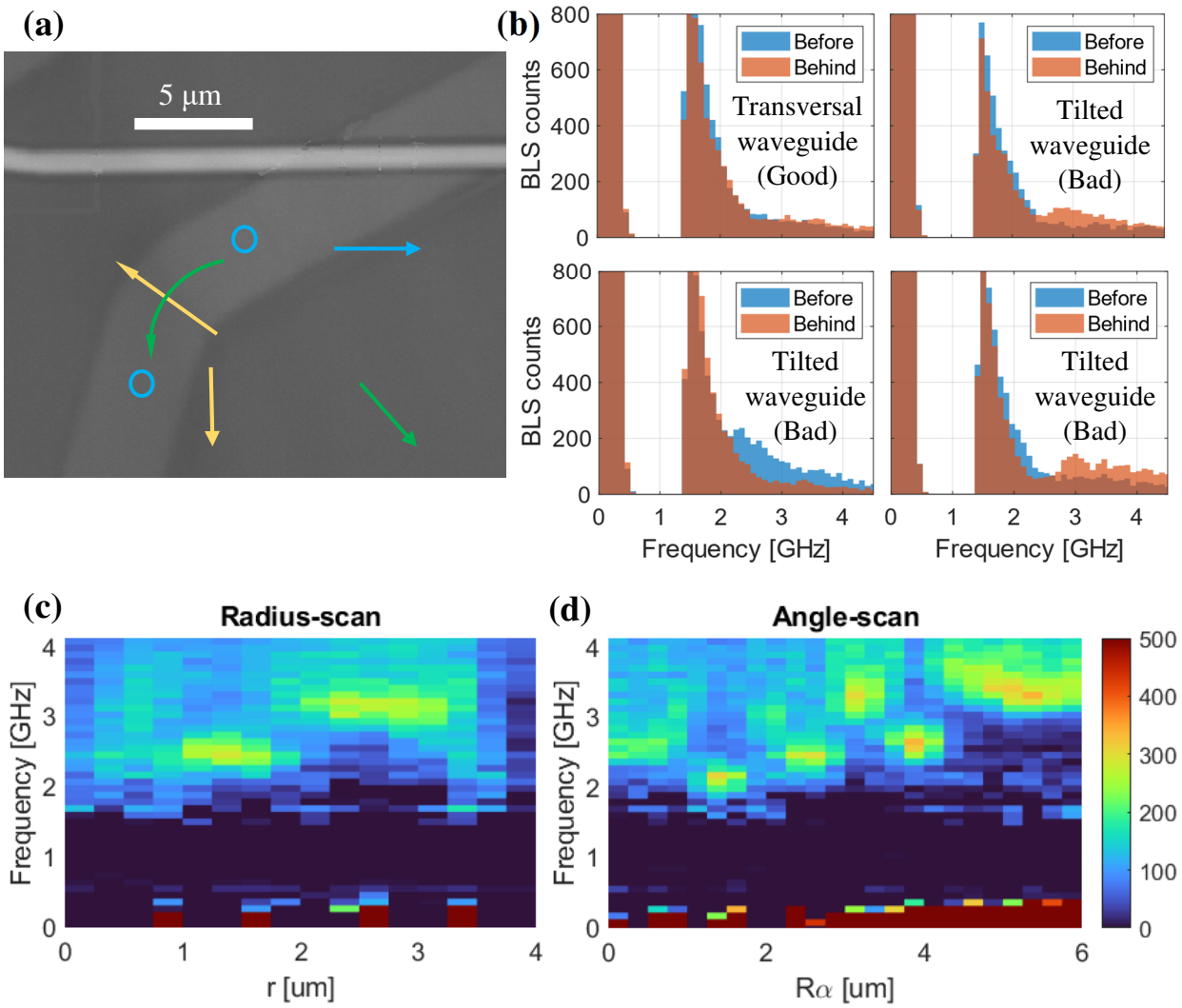

Fig.6.9: **(a)** Light microscope image of the turned waveguide of tilted design with outlined positions of the three measurements. **(b)** Four BLS measurements of thermal magnons with the laser focused before and behind the turn as is outlined by the blue circles in (a). The first measurement is from a waveguide of transversal design with good propagation characteristics [Fig.6.6 (c)], which is shown for comparison. The other three belong to different waveguides of tilted design, which show a large frequency mismatch. The laser mode obfuscates the data, but the main feature can be seen. **(c)** Thermal magnon spectra measured by BLS at different radii in the turn [along the yellow line in (a)]. The last position was definitely outside the magnetic waveguide, and we have used it to subtract the laser mode in (c) and (d), which would otherwise obfuscate the data. Large discrepancies are present. **(d)** Thermal magnon spectra measured at different angles inside the turn [along the green line in (a)]. The wild magnon frequency landscape suggests a complicated magnetization order in the turn. We would expect spin waves to propagate through these areas with low transmission efficiency.

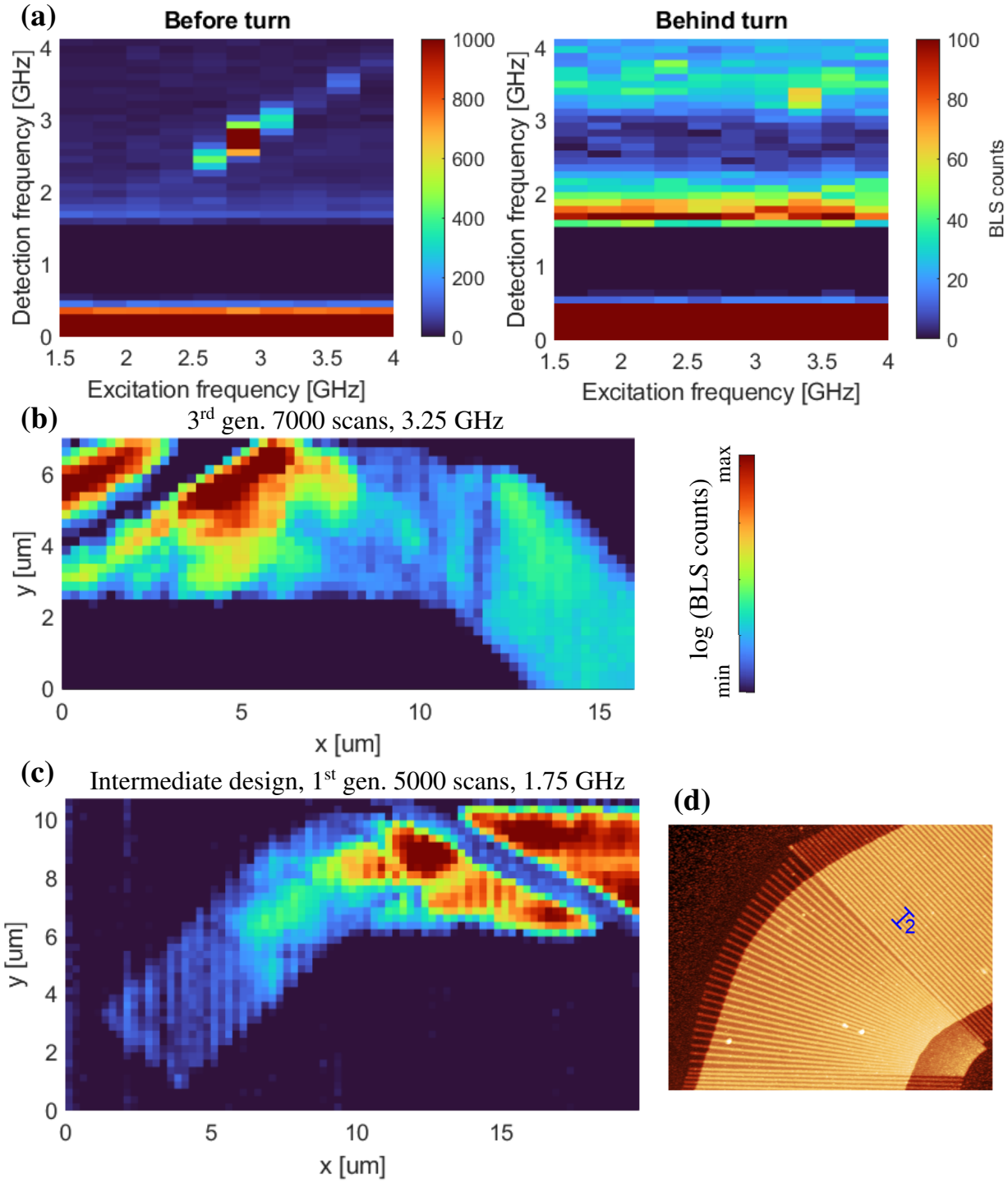

Fig.6.10: **(a)** Measurements performed with changing excitation frequency while the laser was focused at spots before and just behind the turn of a waveguide of tilted design. Some signal above the level of thermal magnons is detected at 3.25 GHz even behind the turn. **(b)** Spin wave intensity at 3.25 GHz in a waveguide of the third generation created by 7000 scans, which was also studied in Fig.6.9 (c), (d) and here in (a). **(c)** Two dimensional BLS measurement of spin wave intensity at 1.75 GHz in a waveguide of the intermediate design, which was created using 5000 scans in the first generation. **(d)** Atomic force microscopy measurement of the intermediate design, which operates with the tilted mode but changes direction of its corrugation in the turn gradually. (d) was measured by Igor Turčan.

Even though we expected poor qualities of the turned waveguides of the tilted design, we have performed the measurements for finding good propagation frequency. The BLS laser spot was focused consecutively before and just behind the turn, and we have changed the excitation frequency. Results of these measurements are displayed in Fig.6.10 (a). The frequency mismatch between the two regions is apparent again, but we managed to detect some signal above the thermal level even behind the turn at the frequency 3.25 GHz. 2D BLS scan of the spin wave intensity on this frequency was then performed [Fig.6.10 (b)]. The spin wave intensity attenuates very quickly and looks like a result of interference between different waves, which were, perhaps, reflected from sides of the waveguide. Some excited waves can still be observed at the beginning of the turn and attenuate from there. Overall, the spin waves do not propagate nicely in this turned waveguide. Several similar structures were measured as well, but the results were not different. The only exception was the turned waveguide of the intermediate design, in which the working mode is tilted the same way as in the proper tilted design, but the in the turn the direction of the corrugation changes gradually as is displayed in Fig.6.10 (d). Its 2D BLS intensity map is presented in Fig.6.10 (c).

A general problem of the tilted mode as the waveguide's working point is that the demagnetizing field (overall shape anisotropy) sways the magnetization more in the long axis of the waveguide. This results in rotation of the dispersion relation (whose anisotropy is determined with respect to the equilibrium magnetization direction) and excitation of a spin wave mode with group velocity not parallel to the waveguide. Two examples of this are shown in Fig.6.11. In the first generation, we did not account for this effect and the result was propagation in a more perpendicular direction from the antenna than was intended [case in Fig.6.11 (a)]. This finding slightly devaluates the measurement in Fig.6.10 (c), because we effectively excited the waves propagating already partially in the direction of waveguide behind the turn. In the second and third generations we have compensated for this by designing the tilt of corrugation from the transversal direction to be smaller than needed and the demagnetizing field [68] would sway the magnetization back into the intended direction. However, strength of the geometrically induced anisotropy was difficult to estimate with sufficient precision in advance and the result was the opposite – magnetization was aligned too transversally [Fig.6.11 (b)]. This issue cannot affect waveguides of the transversal design.

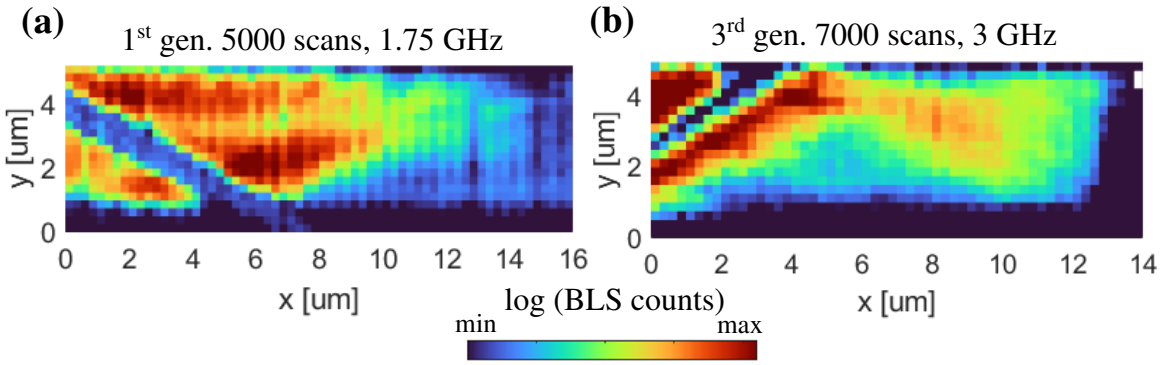

Fig.6.11: **(a)** Two dimensional BLS scan of a spin wave excited on the frequency 1.75 GHz in a straight part of a 1st generation waveguide operating with the tilted mode. Demagnetizing field sways the magnetization more into the long axis of the waveguide, dispersion relation gets rotated together with that and the excited mode does not propagate along the waveguide. **(b)** Spin wave in a 3rd generation waveguide, whose design over-compensated for this effect. This effect was less extreme in a waveguide prepared by 5000 FEBID-scans (not shown).

Conclusion

The goal of this thesis was to study turning of spin waves in two experimental systems with locally modifiable magnetic anisotropy, namely the metastable iron-nickel thin films and wavy waveguides, by means of micromagnetic simulations and Brillouin light scattering experiments.

In the first chapter we have introduced several magnetic phenomena in the framework of micromagnetic theory, which are necessary for a proper understanding of the studied topic. Firstly, we have discussed the different magnetic energies governing the behavior of magnetic systems and their contribution to the effective magnetic field. Then, the Landau-Lifschitz-Gilbert equation describing the spatial and temporal evolution of these systems was introduced. The most important part of this chapter was about spin waves. We have examined their dispersion relation, which is characteristic for its anisotropy – it strongly depends on the angle between the direction of propagation and the equilibrium direction of magnetization. At the end of this chapter, we have shortly reviewed the research about refraction and turning of spin waves.

The second chapter covers techniques used in the course of this thesis. We began by describing our process of fabricating structures using the electron beam lithography. We have used this technique to prepare antennas for excitation of spin waves in all of our samples and to deposit the magnetic layer of the wavy waveguides. Then, we have written about the Brillouin light scattering microscopy, which served as our main analytical tool. It was used to study the magnetic properties of our structures and to measure the spin waves propagating in our samples. The magneto-optical Kerr microscopy was also employed to inspect some of our samples and is therefore shortly mentioned in this chapter. And finally, we have described the simulations, more specifically we have outlined the workings of the finite difference method of the micromagnetic solver MuMax. This program was extensively used to provide insight into the studied problematics and to help us identify good designs for our experiments.

The third chapter was dedicated to the metastable iron-nickel thin films. First, we have talked about how this system works, to summarize, the material can be grown epitaxially on an fcc copper substrate as its continuation, but this phase constitutes only a metastable state, which is paramagnetic. Using the focused ion beam we can locally transform this film into its stable ferromagnetic bcc phase. Moreover, we have shown that the focused ion beam scanning strategy determines the direction of uniaxial anisotropy. This chapter also covers measurements of magnetic properties of some transformed structures, that is, we have estimated the saturation magnetization, decay length and anisotropy direction and strength from Kerr microscopy and Brillouin light scattering measurements.

In the fourth chapter we have discussed the corrugated magnetic films called wavy waveguides. In the beginning the fabrication process is outlined. In the first step of fabricating the wavy waveguides corrugation on the substrate is created by focused electron beam induced deposition, and in the second step the electron beam lithography process is used to build the magnetic waveguide on top of the corrugation. In the next section the geometrically induced anisotropy is studied by simulations and demonstrated in experiments. Origin of this geometrically induced anisotropy is explained for the static and dynamic case, and it is revealed that the anisotropy has a somewhat different character than the conventional crystalline anisotropy, but this difference is not too important for our application.

The fifth chapter deals with refraction of spin waves between different domains of the transformed iron-nickel film. Using the knowledge about the dependence of anisotropy direction on the focused ion beam scanning strategy, we have prepared neighboring domains suitable for refracting waves. Excitation antennas were fabricated to excite spin waves at specific locations, and we have measured the refracting waves by Brillouin light scattering microscopy. The measured waves qualitatively agree with what we would expect from theory given the magnetic properties measured in chapter three.

The last (sixth) chapter contains our investigation about propagating spin waves through turned waveguides with locally varying uniaxial anisotropy direction. It begins with micromagnetic simulations exploring two alternative waveguide designs – in the first one the anisotropy aligns the magnetization in every part of the waveguide transversally, and in the second design the waveguide works in a tilted regime and the anisotropy in the turn evolves in such a way to secure refraction into the same spin wave-mode. The latter design seemed to offer superior spin wave-turning qualities in the simulations. However, we have not been able to experimentally realize it in the wavy waveguide system – the magnetization order was seemingly complicated, and the spin wave waves did not propagate in the waveguide as was intended, which was revealed by the Brillouin light scattering microscopy. We had more success with experimental realization of the transversal design. Spin waves in wavy waveguides of this design propagated through the turn and only partially reflected at its beginning. This result together with the passive nature of our structure presents an improvement over a very similar turned waveguide, which had to be ordered by an external field originating from an underlying conductor [37].

References

[1] M. M. Waldrop, “The chips are down for Moore’s law,” *Nat. News*, vol. 530, no. 7589, p. 144, Feb. 2016, doi: 10.1038/530144a.

[2] A. V. Chumak, “Magnon Spintronics,” in *Spintronics Handbook: Spin Transport and Magnetism, Second Edition*, CRC Press, 2019, pp. 247–302.

[3] T. Fischer *et al.*, “Experimental prototype of a spin-wave majority gate,” *Appl. Phys. Lett.*, vol. 110, no. 15, p. 152401, Apr. 2017, doi: 10.1063/1.4979840.

[4] A. V. Chumak, A. A. Serga, and B. Hillebrands, “Magnon transistor for all-magnon data processing,” *Nat. Commun. 2014 51*, vol. 5, no. 1, pp. 1–8, Aug. 2014, doi: 10.1038/ncomms5700.

[5] C. Abert, “Micromagnetics and spintronics: models and numerical methods,” *Eur. Phys. J. B*, vol. 92, no. 6, p. 120, Jun. 2019, doi: 10.1140/epjb/e2019-90599-6.

[6] H. Kronmüller, “General Micromagnetic Theory,” in *Handbook of Magnetism and Advanced Magnetic Materials*, John Wiley & Sons, Ltd, 2007.

[7] J. M. D. Coey, *Magnetism and Magnetic Materials*. Cambridge University Press, 2009.

[8] K. Y. Guslienko and A. N. Slavin, “Magnetostatic Greens functions for the description of spin waves in finite rectangular magnetic dots and stripes,” *J. Magn. Magn. Mater.*, vol. 323, no. 18–19, pp. 2418–2424, Oct. 2011, doi: 10.1016/j.jmmm.2011.05.020.

[9] B. A. Kalinikos and A. N. Slavin, “Theory of dipole-exchange spin wave spectrum for ferromagnetic films with mixed exchange boundary conditions,” *J. Phys. C Solid State Phys.*, vol. 19, no. 35, pp. 7013–7033, Dec. 1986, doi: 10.1088/0022-3719/19/35/014.

[10] W. Heisenberg, “Zur Theorie des Ferromagnetismus,” *Zeitschrift für Phys.*, vol. 49, no. 9–10, pp. 619–636, Sep. 1928, doi: 10.1007/BF01328601.

[11] B. D. Cullity and C. D. Graham, *Introduction to Magnetic Materials*. John Wiley & Sons, Inc., 2008.

[12] B. Hillebrands and K. Ounadjela, *Spin Dynamics in Confined Magnetic Structures I*. Springer Berlin Heidelberg, 2002.

[13] I. Turčan, “Study of Magnonic Crystals in a Frequency Domain,” Brno University of Technology, 2017.

[14] R. W. Damon and J. R. Eshbach, “Magnetostatic modes of a ferromagnet slab,” *J. Phys. Chem. Solids*, vol. 19, no. 3–4, pp. 308–320, May 1961, doi: 10.1016/0022-3697(61)90041-5.

[15] L. R. Walker, “Magnetostatic modes in ferromagnetic resonance,” *Phys. Rev.*, vol. 105, no. 2, pp. 390–399, Jan. 1957, doi: 10.1103/PhysRev.105.390.

[16] M. J. Hurben and C. E. Patton, “Theory of magnetostatic waves for in-plane magnetized isotropic films,” *J. Magn. Magn. Mater.*, vol. 139, no. 3, pp. 263–291, Jan. 1995, doi: 10.1016/0304-8853(95)90006-3.

[17] D. D. Stancil and A. Prabhakar, *Spin waves: Theory and applications*. Springer US, 2009.

[18] B. A. Kalinikos, M. P. Kostylev, N. V. Kozhus, and A. N. Slavin, “The dipole-exchange spin wave spectrum for anisotropic ferromagnetic films with mixed exchange boundary conditions,” *J. Phys. Condens. Matter*, vol. 2, no. 49, pp. 9861–9877, Dec. 1990, doi: 10.1088/0953-8984/2/49/012.

[19] C. S. Davies, A. V. Sadovnikov, S. V. Grishin, Y. P. Sharaevskii, S. A. Nikitov, and V. V. Kruglyak, "Generation of propagating spin waves from regions of increased dynamic demagnetising field near magnetic antidots," *Appl. Phys. Lett.*, vol. 107, no. 16, p. 162401, Oct. 2015, doi: 10.1063/1.4933263.

[20] J. Stigloher, "Reflection and Refraction of Spin Waves," Universität Regensburg, 2018.

[21] A. V Vashkovskii and E. H. Lokk, "Negative refractive index for a surface magnetostatic wave propagating through the boundary between a ferrite and ferrite-insulator-metal media," *Physics-Uspekhi*, vol. 47, no. 6, pp. 601–605, Jun. 2004, doi: 10.1070/pu2004v047n06abeh001793.

[22] W. Yu, J. Lan, R. Wu, and J. Xiao, "Magnetic Snell's law and spin-wave fiber with Dzyaloshinskii-Moriya interaction," *Phys. Rev. B*, vol. 94, no. 14, p. 140410, Oct. 2016, doi: 10.1103/PhysRevB.94.140410.

[23] T. Hioki, R. Tsuboi, T. H. Johansen, Y. Hashimoto, and E. Saitoh, "Snell's law for spin waves at a 90° magnetic domain wall," *Appl. Phys. Lett.*, vol. 116, no. 11, p. 112402, Mar. 2020, doi: 10.1063/1.5141864.

[24] J. Stigloher *et al.*, "Snell's Law for Spin Waves," *Phys. Rev. Lett.*, vol. 117, no. 3, p. 037204, Jul. 2016, doi: 10.1103/PhysRevLett.117.037204.

[25] J. N. Toedt, M. Mundkowski, D. Heitmann, S. Mendach, and W. Hansen, "Design and construction of a spin-wave lens," *Sci. Rep.*, vol. 6, no. 1, pp. 1–6, Sep. 2016, doi: 10.1038/srep33169.

[26] M. Vogel, P. Pirro, B. Hillebrands, and G. Von Freymann, "Optical elements for anisotropic spin-wave propagation," *Appl. Phys. Lett.*, vol. 116, no. 26, p. 262404, Jun. 2020, doi: 10.1063/5.0018519.

[27] M. Vogel, R. Aßmann, P. Pirro, A. V. Chumak, B. Hillebrands, and G. von Freymann, "Control of Spin-Wave Propagation using Magnetisation Gradients," *Sci. Rep.*, vol. 8, no. 1, p. 11099, Dec. 2018, doi: 10.1038/s41598-018-29191-2.

[28] O. Dzyapko, I. V. Borisenko, V. E. Demidov, W. Pernice, and S. O. Demokritov, "Reconfigurable heat-induced spin wave lenses," *Appl. Phys. Lett.*, vol. 109, no. 23, p. 232407, Dec. 2016, doi: 10.1063/1.4971829.

[29] J. Gloss *et al.*, "The growth of metastable fcc Fe 78 Ni 22 thin films on H-Si(1 0 0) substrates suitable for focused ion beam direct magnetic patterning," *Appl. Surf. Sci.*, vol. 469, pp. 747–752, Mar. 2019, doi: 10.1016/j.apsusc.2018.10.263.

[30] S. A. Bunyaev *et al.*, "Engineered magnetization and exchange stiffness in direct-write Co-Fe nanoelements," *Appl. Phys. Lett.*, vol. 118, no. 2, p. 22408, Jan. 2021, doi: 10.1063/5.0036361.

[31] A. Maziewski *et al.*, "Tailoring of magnetism in Pt/Co/Pt ultrathin films by ion irradiation," *Phys. Rev. B - Condens. Matter Mater. Phys.*, vol. 85, no. 5, p. 054427, Feb. 2012, doi: 10.1103/PhysRevB.85.054427.

[32] B. Obry *et al.*, "A micro-structured ion-implanted magnonic crystal," *Appl. Phys. Lett.*, vol. 102, no. 20, p. 202403, May 2013, doi: 10.1063/1.4807721.

[33] S. Mieszczak, O. Busel, P. Gruszecki, A. N. Kuchko, J. W. Kłos, and M. Krawczyk, "Anomalous Refraction of Spin Waves as a Way to Guide Signals in Curved Magnonic Multimode Waveguides," *Phys. Rev. Appl.*, vol. 13, no. 5, p. 054038, May 2020, doi: 10.1103/PhysRevApplied.13.054038.

[34] B. Rana and Y. C. Otani, "Towards magnonic devices based on voltage-controlled magnetic anisotropy," *Communications Physics*, vol. 2, no. 1. Nature Research, pp. 1–

12, Dec. 01, 2019, doi: 10.1038/s42005-019-0189-6.

[35] X. Xing, Y. Yu, S. Li, and X. Huang, “Howdo spin waves pass through a bend ï¿½,” *Sci. Rep.*, vol. 3, no. 1, pp. 1–6, Oct. 2013, doi: 10.1038/srep02958.

[36] A. V. Sadovnikov *et al.*, “Spin wave propagation in a uniformly biased curved magnonic waveguide,” *Phys. Rev. B*, vol. 96, no. 6, p. 060401, Aug. 2017, doi: 10.1103/PhysRevB.96.060401.

[37] K. Vogt *et al.*, “Spin waves turning a corner,” *Appl. Phys. Lett.*, vol. 101, no. 4, p. 42410, Jul. 2012, doi: 10.1063/1.4738887.

[38] C. S. Davies *et al.*, “Towards graded-index magnonics: Steering spin waves in magnonic networks,” *Phys. Rev. B - Condens. Matter Mater. Phys.*, vol. 92, no. 2, p. 020408, Jul. 2015, doi: 10.1103/PhysRevB.92.020408.

[39] Y. Chen, “Nanofabrication by electron beam lithography and its applications: A review,” *Microelectronic Engineering*, vol. 135. Elsevier, pp. 57–72, Mar. 05, 2015, doi: 10.1016/j.mee.2015.02.042.

[40] T. Sebastian, K. Schultheiss, B. Obry, B. Hillebrands, and H. Schultheiss, “Micro-focused Brillouin light scattering: imaging spin waves at the nanoscale,” *Front. Phys.*, vol. 3, p. 35, Jun. 2015, doi: 10.3389/fphy.2015.00035.

[41] O. Wojewoda, “Phase-resolved brillouin light scattering: development and applications,” Brno University of Technology, 2020.

[42] L. Flajšman, “Magneto-optical study of the dynamic properties of magnetic nanostructures and nanostructured metamaterials,” Brno University of Technology, 2019.

[43] J. A. Arregi, P. Riego, and A. Berger, “What is the longitudinal magneto-optical Kerr effect?,” *J. Phys. D. Appl. Phys.*, vol. 50, no. 3, pp. 3–4, Jan. 2017, doi: 10.1088/1361-6463/aa4ea6.

[44] S. Yamamoto and I. Matsuda, “Measurement of the resonant magneto-optical Kerr effect using a free electron laser,” *Applied Sciences (Switzerland)*, vol. 7, no. 7. MDPI AG, p. 662, Jun. 27, 2017, doi: 10.3390/app7070662.

[45] C. Abert, F. Bruckner, C. Vogler, R. Windl, R. Thanhoffer, and D. Suess, “A full-fledged micromagnetic code in fewer than 70 lines of NumPy,” *J. Magn. Magn. Mater.*, vol. 387, pp. 13–18, Aug. 2015, doi: 10.1016/j.jmmm.2015.03.081.

[46] J. Leliaert and J. Mulkers, “Tomorrow’s micromagnetic simulations,” *J. Appl. Phys.*, vol. 125, no. 18, p. 180901, May 2019, doi: 10.1063/1.5093730.

[47] A. Vansteenkiste, J. Leliaert, M. Dvornik, M. Helsen, F. Garcia-Sanchez, and B. Van Waeyenberge, “The design and verification of MuMax3,” *AIP Adv.*, vol. 4, no. 10, p. 107133, Oct. 2014, doi: 10.1063/1.4899186.

[48] C. L. Ordóñez-Romero *et al.*, “Mapping of spin wave propagation in a one-dimensional magnonic crystal,” *J. Appl. Phys.*, vol. 120, no. 4, p. 43901, Jul. 2016, doi: 10.1063/1.4958903.

[49] W. Rupp *et al.*, “Ion-beam induced fcc-bcc transition in ultrathin Fe films for ferromagnetic patterning,” *Appl. Phys. Lett.*, vol. 93, no. 6, p. 63102, Aug. 2008, doi: 10.1063/1.2969795.

[50] A. Biedermann, R. Tscheliessnig, M. Schmid, and P. Varga, “Local atomic structure of ultra-thin Fe films grown on Cu(100),” *Appl. Phys. A Mater. Sci. Process.*, vol. 78, no. 6, pp. 807–816, Mar. 2004, doi: 10.1007/s00339-003-2435-7.

[51] S. Shah Zaman *et al.*, “Ion-beam-induced magnetic transformation of CO-stabilized fcc

Fe films on Cu(100)," *Phys. Rev. B - Condens. Matter Mater. Phys.*, vol. 82, no. 23, p. 235401, Dec. 2010, doi: 10.1103/PhysRevB.82.235401.

[52] J. Gloss *et al.*, "Ion-beam-induced magnetic and structural phase transformation of Ni-stabilized face-centered-cubic Fe films on Cu(100)," *Appl. Phys. Lett.*, vol. 103, no. 26, p. 262405, Dec. 2013, doi: 10.1063/1.4856775.

[53] J. Holobrádek, "Metastable iron thin films for magnetic metamaterials," Brno University of Technology, 2020.

[54] M. Urbánek *et al.*, "Research Update: Focused ion beam direct writing of magnetic patterns with controlled structural and magnetic properties," *APL Mater.*, vol. 6, no. 6, p. 60701, Jun. 2018, doi: 10.1063/1.5029367.

[55] K. Ashida, T. Kajino, Y. Kutsuma, N. Ohtani, and T. Kaneko, "Crystallographic orientation dependence of SEM contrast revealed by SiC polytypes," *J. Vac. Sci. Technol. B, Nanotechnol. Microelectron. Mater. Process. Meas. Phenom.*, vol. 33, no. 4, p. 04E104, Jul. 2015, doi: 10.1116/1.4927136.

[56] X. Liu, Y. Sasaki, and J. K. Furdyna, "Ferromagnetic resonance in Ga1−xMnxAs: Effects of magnetic anisotropy," *Phys. Rev. B - Condens. Matter Mater. Phys.*, vol. 67, no. 20, p. 205204, May 2003, doi: 10.1103/PhysRevB.67.205204.

[57] L. Flajšman *et al.*, "Zero-field propagation of spin waves in waveguides prepared by focused ion beam direct writing," *Phys. Rev. B*, vol. 101, no. 1, p. 014436, Jan. 2020, doi: 10.1103/PhysRevB.101.014436.

[58] M. O. Liedke *et al.*, "Crossover in the surface anisotropy contributions of ferromagnetic films on rippled Si surfaces," *Phys. Rev. B - Condens. Matter Mater. Phys.*, vol. 87, no. 2, p. 024424, Jan. 2013, doi: 10.1103/PhysRevB.87.024424.

[59] K. Chen, R. Frömter, S. Rössler, N. Mikuszeit, and H. P. Oepen, "Uniaxial magnetic anisotropy of cobalt films deposited on sputtered MgO(001) substrates," *Phys. Rev. B - Condens. Matter Mater. Phys.*, vol. 86, no. 6, p. 064432, Aug. 2012, doi: 10.1103/PhysRevB.86.064432.

[60] K. Zhang, M. Uhrmacher, H. Hofsäss, and J. Krauser, "Magnetic texturing of ferromagnetic thin films by sputtering induced ripple formation," *J. Appl. Phys.*, vol. 103, no. 8, p. 83507, Apr. 2008, doi: 10.1063/1.2905324.

[61] M. Körner *et al.*, "Two-magnon scattering in permalloy thin films due to rippled substrates," *Phys. Rev. B - Condens. Matter Mater. Phys.*, vol. 88, no. 5, p. 054405, Aug. 2013, doi: 10.1103/PhysRevB.88.054405.

[62] I. Turčan, "Magnetism in curved geometries," Brno University of Technology.

[63] I. Turčan, L. Flajšman, O. Wojewoda, V. Roučka, O. Man, and M. Urbánek, "Spin wave propagation in corrugated waveguides," *Appl. Phys. Lett.*, vol. 118, no. 9, p. 92405, Mar. 2021, doi: 10.1063/5.0041138.

[64] V. E. Demidov, M. P. Kostylev, K. Rott, P. Krzysteczko, G. Reiss, and S. O. Demokritov, "Excitation of microwaveguide modes by a stripe antenna," *Appl. Phys. Lett.*, vol. 95, no. 11, p. 112509, Sep. 2009, doi: 10.1063/1.3231875.

[65] S. Ki and J. Dho, "Strong uniaxial magnetic anisotropy in triangular wave-like ferromagnetic NiFe thin films," *Appl. Phys. Lett.*, vol. 106, no. 21, p. 212404, May 2015, doi: 10.1063/1.4921784.

[66] M. Vaňatka, "Static and dynamic properties of nanostructured magnetic materials," Brno University of Technology, 2021.

[67] O. Wojewoda *et al.*, "Propagation of spin waves through a Néel domain wall," *Appl.*

Phys. Lett, vol. 117, no. 2, p. 22405, Jul. 2020, doi: 10.1063/5.0013692.

[68] A. Aharoni, "Demagnetizing factors for rectangular ferromagnetic prisms," *J. Appl. Phys.*, vol. 83, no. 6, pp. 3432–3434, Jun. 1998, doi: 10.1063/1.367113.

List of used abbreviations

CMOS	Complementary Metal-Oxide-Semiconductor
LLG	Landau-Lifschitz-Gilbert (equation)
DE	Damon-Eshbach (spin wave mode)
BV	Backward volume (spin wave mode)
FIB	Focused ion beam
FEBID	Focused electron beam induced deposition
EBL	Electron beam lithography
PMMA	Poly-(methyl methacrylate)
BLS	Brillouin light scattering (microscope)
FPi	Fabry-Perot interferometer
FSR	Free spectral range
PBC	Periodic boundary condition
FT	Fourier transform
SEM	Scanning electron microscope
FMR	Ferromagnetic resonance
GIS	Gas injection system